The Dynamics of the Unitary Fermi Gas

Yuan Lung Luo

A dissertation
submitted in partial fulfillment of the
requirements for the degree of

Doctor of Philosophy

University of Washington

2013

Reading Committee:

Aurel Bulgac, Chair

Subhadeep Gupta

Stephen R. Sharpe

Program Authorized to Offer Degree:
Physics

University of Washington

Abstract

The Dynamics of the Unitary Fermi Gas

Yuan Lung Luo

Chair of the Supervisory Committee:
Professor Aurel Bulgac
Department of Physics

This dissertation is concerned with the dynamics of dilute Fermi gases in the unitary regime with short-range interaction and infinite scattering length. This work represents the first ab-initio simulation of quantized vortex generation and domain walls generation. In addition, the interaction of quantized vortices and domain walls are investigated.

TABLE OF CONTENTS

LIST OF FIGURES

ACKNOWLEDGMENTS

I thank my Adviser Prof. Aurel Bulgac and collaborators Kenny Roche for all the guidance and support throughout my graduate studies. I thank my friends, especially my housemate Frankie, for all the fun we do that help me survive through the downtime during my research. Also I want to thank my buddies in Husky Cycling team for the thrills and companions during weekend bike rides throughout the Western Washington area. Finally I want to thank my parents and my brother for supporting me, both financially and spiritually for my studies here in the U.S..

Chapter 1

INTRODUCTION

In our world, dynamics happen everywhere. In sophisticated machines, hundreds of parts and motors together follow the equations derived from the Hamiltonian in classical mechanics and complete complex tasks. In the air and the ocean, interactions of solid objects with fluid or gas create many interesting linear or nonlinear hydrodynamics like simple flows, vortices, turbulence, burst of shock waves during explosion, and solitary waves drifting through the long Panama Canal. Finally, in our daily lives dynamics appear as the flow of information, for example the traffic flow at rush hours, the social media information surge on the Internet during and after the Super Bowl , and fluctuations in the stock market in response to events happening around the globe. These examples of dynamics are fascinating. At the same time they are important to understand in order to improve our lives and advance our technology.

In physics, dynamics are even more intriguing when they appear together with quantum phenomena. In particular, with the dynamics of fluid flow appear together with quantum properties, a fascinating phenomenon called "superfluidity", appears, and it gives many properties that are strange in the eyes of classical fluid dynamics. Examples of this are zero-resistance flow, quantized vortices and lattices, and domain walls. Even more complicated is the study of the dynamics of a superfluid in a strongly-interacting system. The interplay of different interactions, including kinetic potential, correlation potential, and pairing potential, together makes the physical description of such a dynamical system complicated and challenging. At the same time it is rewarding because of the more interesting properties emerged from such system.

In this thesis we investigate several phenomena of superfluid dynamics in a special strongly interacting system called the "Unitary Fermi Gases" (UFG), with definition provided later in this chapter. The dynamical properties we investigate include quantized

vortex dynamics, nonlinear hydrodynamic collisions, and domain wall dynamics.

To help readers build up the theoretical tools to understand our research, in this chapter we first outline the elements of many-body physics and other theoretical methods. First we begin with non-interacting quantum fermionic systems, and then to interacting systems with extension to superfluidity. We then discuss quantum Monte Carlo methods and density functional methods. Second, we introduce unitary fermi gas systems and their experimental realizations with ultra-cold atoms and our particular models to describe their dynamics. Finally, we briefly describe the properties of quantized vortices and the domain walls (dark solitons) which were observed in our research.

1.1 Free Fermions

When we put identical particles together at zero temperature, even if there is no interaction between the particles, their statistical properties characterize them into two types: bosons and fermions. For bosons the particles can occupy the same quantum state, while the fermions cannot. The latter phenomenon is referred to as *the Pauli principle*.

Bosons carry integer spins, examples being photons, phonons, and helium 4, while fermions carry half integer spin, examples being protons, electrons, neutrons, and Lithium 6.

Because the Pauli principle prevents protons, neutrons, and electrons from occupying the same quantum state, many different kinds of atoms are formed, and together these atoms create the lively universe and different life forms on the Earth.

In a non-interacting fermion system in zero temperature subject to no external confining potential, the momentum space is the eigenspace, and the fermions occupy each momentum $\vec{k}$ up to the degeneracy factor g (ex: spins) for each momentum state. In the ground state, to minimize total energy, the fermions occupy a sphere centered at the origin. The surface of the sphere is called the fermi surface, with fermi momentum k_F and energy $\epsilon_F = \frac{k_F^2}{2m}$. The fermi momentum is related to the density ρ as:

$$k_F = (\frac{6\pi^2}{g}\rho)^{1/3} \tag{1.1}$$

And the total energy E is related to fermi energy as:

$$E = \frac{3}{5}\epsilon_F N \tag{1.2}$$

where N is the total particle number.

For a spatially inhomogenous system such as the cold atoms in a trap with equal number of particles in each spin state and spin-independent potentials, the momentum space is no longer the eigenspace of the system. However, when the external potential $U(\vec{r})$ is "smooth" enough (the variation of the potential is large compared to the inter-particle distance), one can use the "Thomas Fermi approximation" to treat the particles at each position $\vec{r}$ as if they are in the non-interacting system with fermi energy as $\epsilon_F(\vec{r}) = \mu - U(\vec{r})$, where μ is the chemical potential that satisfies:

$$N = g\frac{1}{(2\pi)^3}\int d\vec{r}\sqrt{2(\mu - U(\vec{r}))} \tag{1.3}$$

We will see later that the Fermi vector k_F, Fermi energy ϵ_F, and the chemical potential μ can be applied also to quasi-particles. These are the fundamental scales of the strongly-interacting unitary fermi gas.

Finally, in non-interacting fermi systems one can have two basic elementary excitations. For particle/hole excitation one can take a fermion within the fermi sphere, excite it, and move it to an energy level outside of the fermi sphere. This creates a "particle" on top of the fermi sea and leaves a "hole" in the fermi sea. The hole is an empty state that has properties very similar to the particle, with opposite wave-vector, excitation energy, mass and charge, and with the same velocity, [42].

For almost free fermion system with very weak interaction, we can collectively excite the system by compressing/extending the particle gas as a whole and creating excitations such as sound waves. With classical hydrodynamics [27] one can show that the speed of sound is:

$$c_s = k_F/\sqrt{3} \tag{1.4}$$

1.2 Interacting Fermion System

We now look at the interacting fermion system at zero temperature. With interaction, the fermions become "correlated" to each other, and thus in general each fermion would not behave the same as a free fermion. However, as we will see later, by introducing the concept of "quasi-particles", one could describe an interacting system with fermions similar to free fermions, thereby reducing the complexity of the problem. We will begin by describing the Hartree-Fock treatment of fermions and introduce the notion of correlation and quasi-particles. Then we will examine one of the fascinating phenomena that arises from mutual fermion interaction, the superfluidity, and the BCS theory that describes it with weak interaction. Finally, we will combine Hartree-Fock and BCS and introduce the Hartree-Fock-Bogoliubov theory to describe a superfluid system when both pairing and part of the correlation energy are considered.

1.2.1 The Hartree Fock Theory

In terms of second quantization [27], the Hamiltonian of a fermionic system with only two-body interaction can be written as:

$$\begin{aligned} H &= \sum_{l_1,l_2} t_{l_1,l_2} a^\dagger_{l_1} a_{l_2} + \frac{1}{4} \sum_{l_1,i_2,i_3,i_4} \bar{v}_{l_1 l_2,l_3 l_4} a^\dagger_{l_1} a^\dagger_{l_2} a_{l_3} a_{l_4} \\ \bar{v}_{l_1 l_2,l_3 l_4} &= v_{l_1 l_2,l_3 l_4} - v_{l_1 l_2,l_4 l_3} \end{aligned} \tag{1.5}$$

where $a^\dagger_{l_1}$,a_{l_2} are the fermionic creation/destruction operators in a particular basis, and t, v are the matrix/tensor elements of the kinetic and interaction energies. Within a trap, there will also be an external potential term $U_{ext l_1,l_2} a^\dagger_{l_1} a_{l_2}$.

In general the exact ground state of Eqn.(1.5) is hard to find, so instead one uses the equivalence of Schrodinger equation to the *variational principle*: the ground state $|g\rangle$ is the wave-function that minimizes the total energy $E_H = \langle g|H|g\rangle$. One then guesses the form of the ground state with a trial wave function with variable parameters, and determines the parameters by minimizing E_H. In Hartree Fock theory one assumes that the trial wave-function is a *Slater determinant*

$$|HF\rangle = \Pi_{i=1}^{N} c_i^\dagger |-\rangle \tag{1.6}$$

of N *quasi-particles* with creation operator $c_i^\dagger$, and $|-\rangle$ is the vacuum state. The number N is the same as the number of particles in the system. The quasi-particles are linear combinations of the creation operators $a_{l_1}^\dagger$:

$$c_i^\dagger = \sum_k b_{ik} a_k^\dagger \tag{1.7}$$

and they satisfy the unitary transformation:

$$\sum_k b_{ik}^* b_{kj} = \delta_{ij} \tag{1.8}$$

By minimizing the Hartree Fock energy $E_{HF} \equiv \langle HF|H|HF\rangle$ with respect to the linear parameters, we find that the single-particle wave-functions ϕ_i corresponding to $c_i^\dagger$ diagonalize the Hartree Fock Hamiltonian H_{HF}:

$$H^{HF} = \sum_{kk'} h_{kk'} a_k^\dagger a_{k'} = \sum_{kk'} (t_{kk'} + \sum_{j=1}^{N} \bar{v}_{kjk'j}) a_k^\dagger a_{k'} = \sum_k \epsilon_k a_k^\dagger a_k \tag{1.9}$$

Using the eigen-functions as the new basis, we can express the energy E^{HF} as

$$E^{HF} = \sum_{i=1}^{N} t_{ii} + \frac{1}{2} \sum_{i,j=1}^{N} \bar{v}_{ij,ij} \tag{1.10}$$

Here we see several features of an interacting system. First, in Eqn.(1.10) the interaction potential introduces another term besides the kinetic energy term (and the external energy term, if an external potential is present). This term is called the "direct" and "exchange" energies in the Hartree Fock theory. Physically the direct energy represents the part of the interaction energy from overlapping the densities of all pairs of quasi-particles, and the exchange energy represents the density repulsion resulting from the Pauli principle. For a translation-invariant interaction potential $v(\vec{x_1}, \vec{x_2}) = v(\vec{x_1} - \vec{x_2})$, the direct and exchange energies have the form:

$$
\begin{aligned}
E_{\text{direct}} &= \frac{1}{2}\sum_{j,k}\int_{\vec{x_1}} d^3x_1 \int_{\vec{x_2}} d^3x_2 v(\vec{x_1}-\vec{x_2})|\phi_j(\vec{x_1})|^2|\phi_k(\vec{x_2})|^2 \\
E_{\text{exchange}} &= -\frac{1}{2}\sum_{j,k}\int_{\vec{x_1}} d^3x_1 \int_{\vec{x_2}} d^3x_2 v(\vec{x_1}-\vec{x_2})\phi_j^*(\vec{x_1})\phi_k(\vec{x_1})\phi_k^*(\vec{x_2})\phi_j(\vec{x_2}) \quad (1.11)
\end{aligned}
$$

In a more general sense, the direct and exchange energies represent part of the *correlation energy* from the correlated motions of fermions due to the mutual interaction potential in Eqn.(1.5). In strongly interacting systems, the correlation energy can have the same order of magnitude as the kinetic energy, and thus dramatically alter the properties of the system. Later we will also see that when incorporating superfluidity into our trial wave-functions, another term called "pairing potential" will emerge to take into consideration of the short range correlations of fermion pairs in the fermi sea.

Another feature we can see from Eqn.(1.10) is that, with approximation, we can use a set of independent single-particle wave-function to describe a many-body system. However these single-particle wave-functions are not totally like the free fermions described in the previous section. For example, the eigen-energies of these quasi-particle wave-functions with momentum k have the form:

$$\epsilon_k = \frac{\alpha}{2}k^2 + U + U_{\text{ext}} \quad (1.12)$$

The parameter α is 1 for non-interacting particles, while for quasi-particles it is not necessarily 1. The inverse of α is called the "effective mass" that represents the extra (or less) effort a quasi-particle spends to move through the interacting fermi sea. The term U, called the exchange potential, also comes from the mutual interaction. Finally, when we compare Eqn.(1.10) and the sum of the eigen-energy we see that they are not equal. This explains that the quasi-particles really interact with each other through the term α and U, and thus although they are orthogonal to each other they are really not "free" fermions.

1.2.2 Superfluidity

The Hartree Fock Theory takes into consideration of some of the fermion correlations. However it could not explain another fascinating interacting system: the superfluid system.

Superfluid systems appear in some materials, for example mercury metal, in low temperature. These materials display a phenomenon that the flow, for example the mass flow of superfluid helium or the current flow in metals, has absolute zero resistance. We will defer the discussion of other superfluid phenomena to later chapters and focus here on the microscopic theory.

Microscopically superfluidity is caused by the short-range interaction between fermions that form a "bound pair"[22] with fermion with one state $k, \uparrow$ and another in the conjugate state $\bar{k} \equiv -k, \downarrow$. Due to the small but finite bound energy these "Cooper pairs" could withstand the inelastic scattering caused by small external perturbations (defects in lattice crystals or dragging forces from liquid containers) and flow without resistance. To capture such correlating effect in our trial wave-function, for an almost free fermion system with short range interaction, Bardeen, Cooper, and Schrieffer [8] proposed the so called "BCS" wave-function:

$$|BCS\rangle = \Pi_{k>0}(u_k + v_k a_k^\dagger a_{\bar{k}}^\dagger)|-\rangle \tag{1.13}$$

where $|-\rangle$ represents the vacuum state, $\bar{k}$ is the "time-conjugate" state of the $\bar{k}$ state, with momentum $\vec{\bar{k}} = -\vec{k}$ and opposite spin. The coefficients u_k and v_k are complex and have the restriction that the norm is unity, $|u_k|^2 + |v_k|^2 = 1$. One could then determine the coefficients by the variational principle, with one extra requirement that the expected particle number need to be a desired number N. This is because the BCS wavefunction does not conserve particles. We therefore get the following set of equations:

$$\begin{aligned}
2\sum_{k>0} v_k^2 &= N \\
v_k^2 &= \frac{1}{2}\{1 - \frac{\epsilon_k}{\sqrt{\epsilon_k^2 + \Delta_k^2}}\} \\
u_k^2 &= \frac{1}{2}\{1 + \frac{\epsilon_k}{\sqrt{\epsilon_k^2 + \Delta_k^2}}\} \\
\epsilon_k &= t_{kk} + \sum_{k'>0, k'<0} v_{kk'kk'} v_{k'}^2 - \lambda \\
\Delta_k &= -\sum_{k'>0} v_{k\bar{k}k'\bar{k}'} u_{k'} v_{k'}
\end{aligned} \tag{1.14}$$

We see that if the parameter Δ_k in Eqn. (1.14) reduces to zero we recover the equations for a normal system. As a result, non-zero Δ_k is characteristic for a superfluid system. Since Δ_k is also the energy gap in the excitation spectrum we call it the gap parameter. We now see how we can represent the BCS equation in a form of a quasi-particle wave-function like Eqn. (1.6). This could be achieved by the "Bogoliubov transformation":

$$c_k^\dagger = u_k a_k^\dagger - v_k a_{\bar{k}} \tag{1.15}$$

$$c_{\bar{k}}^\dagger = u_k a_{\bar{k}}^\dagger + v_k a_k \tag{1.16}$$

$$|BCS\rangle \propto \prod_{k>0,k<0} c_k|-\rangle \tag{1.17}$$

$$\tag{1.18}$$

and the significance of the gap parameter appears in the quasi-particle energy E_k

$$E_k = \sqrt{\epsilon_k^2 + \Delta_k^2} \tag{1.19}$$

which we then see that the energy has a minimal value, or "gap" of strength $|\Delta|$. Such gap is the reason why superfluid systems have no-resistance flow, as to generate excitation one needs to have internal energy of at least Δ. With energy smaller than that the system in the moving frame will remain stationary. Landau [2] considered the internal energy of a moving fluid with velocity v and found that there is a critical velocity v_c above which superfluidity does not occur:

$$v_c = (E_k/k)_{min} \tag{1.20}$$

The exact value of v_c depends on the shape of the quasi-particle excitation spectrum. For typical BCS-derived theories describing almost-free electrons with small attractive interaction, we have $v_c = \frac{\Delta}{k_F}$ [57].

The magnitude of the gap also measures the fraction of superfluid inside the system. By comparing it with the phenomenological Ginsburg-Landau equation [27] that connects Δ to superfluid flow, the requirement of the single-valuedness of Δ requires that, if there is any flow inside the superfluid system it has to be quantized, with the unit flow being

$$\oint v \cdot ds = \frac{hn}{m} \tag{1.21}$$

where n is a positive integer. Such quantization of circulation, and thus quantization of angular momentums, is the basis of quantized vortices we study in this thesis. We will describe the properties of quantized vortices later in this chapter.

1.2.3 Hartree Fock Boboliubov Theory

We see in Hartree Fock Theory and BCS theory that a unitary transformation on the creation and destruction operators can give us ground states of quasi-particles, which describe a normal interacting system and a superfluid system. Naturally if we can combine the transformative properties of both theories, we should be able to have a trial wave-function suitable to describe *both* the correlation effects captured in the Hartree Fock and in the BCS theory. This is done by having the most general unitary transformation onto the operators in Eqn.(1.5):

$$\beta_k^\dagger = \sum_l U_{lk} a_l^\dagger + V_{lk} a_l \tag{1.22}$$

where U and V here are matrices, and by unitarity they satisfy

$$U^\dagger U + V^\dagger V = 1 \tag{1.23}$$

$$U U^\dagger + V^* V^T = 1 \tag{1.24}$$

$$U^T V + V^T U = 1 \tag{1.25}$$

$$U V^\dagger + V^* U^T = 0 \tag{1.26}$$

Minimizing the trial quasi-particle ground state wave-function, one obtains the so-called *Hartree-Fock-Bogoliubov (HFB)* equation:

$$\begin{pmatrix} h & \Delta \\ -\Delta^* & -h^* \end{pmatrix} \begin{pmatrix} U_k \\ V_k \end{pmatrix} = \begin{pmatrix} U_k \\ V_k \end{pmatrix} \cdot E_k \tag{1.27}$$

where both h and Δ are now matrices, and h contains the direct and exchange potentials in the Hartree Fock equation Eqn.(1.10). The matrices h and Δ are functions of the density matrix ρ and the pairing tensor κ, and they are functions of matrices U_k and V_k:

$$\rho = V^* V^T$$
$$\kappa = -UV^\dagger \tag{1.28}$$

Furthermore, as for the BCS equation the chemical potential is determined by satisfying the particle number constraint:

$$2 * tr(\rho) = N \tag{1.29}$$

which requires the HFB equation to be solved iteratively.

To determine the matrices h and Δ, normally one needs to work through the second quantization rule and Hamiltonian [29]. However, as described in the later section in this chapter one can use the density functional theory and quantum Monte Carlo methods to get an energy functional of the unitary fermi gas, and derive an equation similar to the HFB equation. Such approach is tested and shown to accurately describe the dynamics of unitary fermi gases.

1.3 Theoretical tools to describe unitary fermi gases

1.3.1 Density Functional Theory

The Density Functional Theory (DFT) is a theory proven by P. Hohenberg and W. Kohn in 1964 [35]. They shows that the density of the physical system is in one-to-one correspondence with the system's Hamiltonian. Ever since its discovery in 1964, the density functional theory, due to the ease with which it treats very large particle systems, has became a workhorse in condensed matter physics and computational chemistry. In this dissertation we will use an extension of DFT to treat superfluid unitary fermi gas system.

Mathematically, the DFT theory proves that for each normal physical system, its ground state can be described as a functional of density n

$$E(n) = F(n) + \int v_{ext}(\vec{r}) n(\vec{r}) d\vec{r} \tag{1.30}$$

where v_{ext} is the external potential. $F(n)$ is a functional unique to this physical system and independent of v_{ext}. The system's ground state density is determined by minimizing Eqn.(1.30) subject to the particle number constraint:

$$N = \int n(\vec{r}) d\vec{r} \tag{1.31}$$

The functional $F(n)$ contains a term from the kinetic energy of the particle, $T(n)$, and a term from the interaction potential between the particles , $E_v(n)$. The form of $T(n)$ is well known in terms of the wave-function:

$$T(n) = \frac{1}{2} \int \nabla \phi^{\dagger}(n) \nabla \phi(n) d\vec{r} \tag{1.32}$$

while $E_v(n)$ is usually complicated and non-local. However, for many systems such as the high-density electron gas, $E_v(n)$ can be approximated as a term that depends only on the local density $n(\vec{r})$

$$E_v^{LDA}(n) = \int g(n(\vec{r})) d\vec{r} \tag{1.33}$$

This is called the "local density approximation (LDA)" [43]. It greatly simplifies the calculation and has been found in many systems to be a good approximation. For other systems, sometimes higher gradient terms are needed, and they are called the "generalized gradient approximation (GGA)":

$$E_v^{GGA}(n) = \int g(n(\vec{r}), \nabla n(\vec{r}), ...) d\vec{r} \tag{1.34}$$

Although one can directly solve the coupled equation derived from varying the functional in Eqn.(1.30), it is harder to do so. Furthermore, we would like to know if the density problem can be translated into the more familiar eigen-function problem. In [43] Kohn and Sham proposed that, with the density $n(r)$ taken to be the sum of some *single-particle* wave-functions $\phi_i(\vec{r})$,

$$n(\vec{r}) = \sum_{i}^{N} |\phi_i(\vec{r})|^2 \tag{1.35}$$

the minimization of the functional can be transferred to solving the eigen-problem of single-particle Kohn-Sham Hamiltonian:

$$\begin{aligned} H_{\mathrm{KS}}\phi_i &= \epsilon_i\phi_i \\ H_{\mathrm{KS}} &= -\frac{1}{2}\nabla^2 + \frac{\delta E_v}{\delta n} \end{aligned} \tag{1.36}$$

While the original DFT applies only to the ground state of the system, Runge and Gross [62] in 1984 extended the DFT theory to time-dependent systems and opened the gateway of using DFT for dynamical problems. The time-dependent equation is similar to the time-dependent Schrodinger equation:

$$i\frac{\partial}{\partial t}\phi_i = H_{\mathrm{KS}}(t)\phi_i \tag{1.37}$$

$$H_{\mathrm{KS}}(t) = -\frac{1}{2}\nabla^2 + \frac{\delta E_v(t)}{\delta n} \tag{1.38}$$

where the time-dependent term in $H_{KS}(t)$ enters from the time dependent external potential.

Another major advance critical to our DFT formulation of the superfluid unitary fermi gas appeared in 1988, where Oliveira, Gross and Kohn [54] extended DFT from treating the normal electronic systems to the superfluid systems. In their formulation, the system's functional not only depends on the real, particle density $n(\vec{r}) \equiv \langle\phi^\dagger(\vec{r})\phi(\vec{r})\rangle$, where $\phi^\dagger(\vec{r})$ is the creation operator at position $\vec{r}$, but also on the complex, pairing (anomalous) density $\nu(\vec{r}) \equiv \langle\phi^\dagger(\vec{r})\phi^\dagger(\vec{r})\rangle$ and its conjugate

$$E_{SF} = F_{SF}(n, \nu, \nu^\dagger) + \int v_{ext}(\vec{r})n(\vec{r})d\vec{r} \tag{1.39}$$

We will see in next section how we construct a superfluid energy functional for the superfluid unitary fermi gas, and how we derive from it an "HFB-like" equation similar to Eqn. (1.27) and its time-dependent version of the form Eqn. (1.38).

1.3.2 Quantum Monte Carlo

The Monte Carlo (MC) method is a method to use randomly generated numbers to perform numerical calculations, in particular the summation of different terms. A simple example is the calculation of π value. As shown in Fig.(1.1), the number π can be represented as the area ratio between a one-quarter circle with radius 1 and a square with length 1 times 4. Thus, to get the value π, one first creates a unit square and inscribe a quarter-circle inside. One then distributes points that have their x, y values are generated from a uniformly distributed random number generator from $(0-1)$. Finally one examines the ratio of points lying within the quarter-circle to the total points and gets an estimation of $\pi/4$. The error, according to statistical theory, will decrease as the square root of the total points n (Central Limit Theorem).

Generalizing this simple idea, assume there is an expression E that sums over an ensemble of configurations $(r_1, r_2, ..., r_N)$ with a certain amount of positive weight $w(r_1, r_2, ...r_N)$ that adds up to 1 over the entire ensemble, and a function $f(r_1, r_2, ..., r_N)$:

$$\begin{aligned} E &= \sum_{r_1}\sum_{r_2}...\sum_{r_N} w(r_1, r_2, ..., r_N) f(r_1, r_2, ..., r_N) \\ 1 &= \sum_{r_1}\sum_{r_2}...\sum_{r_N} w(r_1, r_2, ..., r_N) \end{aligned} \tag{1.40}$$

Such expression can be calculated by generating configurations $(r_1, r_2, ..., r_N)$ with probability $w(r_1, r_2, ..., r_N)$, adding up the value $f(r_1, r_2, ..., r_N)$, and then averaging the result over the entire number of configurations.

The quantum Monte Carlo (QMC) method is to apply Monte Carlo to calculate quantum physical quantities such as the expectation value of Hermitian operators. Examples of this are the system's total energy $E = \langle\phi|H|\phi\rangle$ and the particle number $N = \langle\phi|\rho|\phi\rangle$. In quantum mechanics with fermions, however, one has to deal with the fact that the weight $w(r_1, r_2, ...r_N)$ might not be a positive number due to sign change when swapping two fermions. This "sign problem" results into averaging many positive and negative number and creates large noise-to-signal ratios. To solve this sign problem for a fermion system one thus needs to introduce some approximations into the equations.

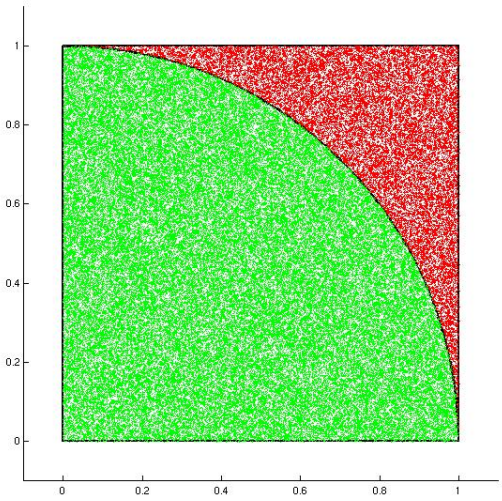

Figure 1.1: Monte Carlo calculation of the value π. A simulation of $100,000$ points are randomly distributed in the unit square. Those lying in the quarter-circle are labeled green, and others red. The π value is estimated by the number of green points divided by $100,000$, then multiply by 4. The result from this simulation was 3.14176 which is correct up to the 3rd digit to the actual π value.

The most intuitive QMC method is the variational Monte Carlo, where the expectation value of some operators O has the form:

$$O = \int |\Phi(R,C)|^2 O(R) dR / \int |\Phi(R,C)|^2 dR \tag{1.41}$$

$\Phi(R,C)$ is the wave-function value at the coordinate R, which has $3N$ variables for three dimension and N particles. The specific set of parameters C are what we want to optimize to satisfy a certain condition from the variational principle, for example to minimize the energy. $O(R)$ is the local value of the operator at that coordinate. To sample through different distributions, one typically uses the so-called "Metropolis Algorithm" [52] to generate new coordinate R_{m+1} based on previous coordinate R_m and satisfies the distribution $|\Phi(R)|^2 / \int |\Phi(R)|^2 dR$. Finally, The evaluation is performed over the landscape of parameters C to find the "best" wave-function according to the variational principle. This can be done either by simply evaluating all sets of parameters or implementing min/max methods such as the conjugate gradient method [87].

In our study, the parameters of our density functional are determined with another QMC method, the Green's Function Monte Carlo (GFMC)[20]. The underlying theory of GFMC is that for a non-degenerate system, any initial wave-function ϕ_I reduces to the ground-state wave-function when it is applied with the imaginary time operator:

$$\phi(\tau \to \infty) = lim_{\tau \to \infty} e^{-(H - E_T)} \phi_I \to e^{-(E_0 - E_T)} \phi_0 \tag{1.42}$$

with a reference energy E_T slightly smaller than the ground state energy. This theorem is easy to prove by representing the wave-function with the eigen-state of the Hamiltonian. By discretizing the imaginary time operator and representing the operator in coordinate space R, one derives the formation for the wave-function at later time $\tau + \Delta\tau$ as the wave-function at time τ propagated by the imaginary Green's function:

$$\phi(R, \tau + \Delta\tau) = \int dR' G(R, R') \phi(R', \tau) \tag{1.43}$$

With small time step, the interacting Green's function $G(R, R')$ can be approximated as the product of potential exponentials and the free fermion Green's function:

$$G(R, R') \approx e^{-[V(R)-E_T]\Delta\tau/2} G_0(R, R') e^{-[V(R)-E_T]\Delta\tau/2}$$
$$G_0(R, R') = [\frac{m}{2\pi\hbar^2\Delta\tau}]^{3/2} e^{-m(R-R')^2/2\hbar^2\Delta\tau} \tag{1.44}$$

By dividing the total imaginary time τ into N small steps $\Delta\tau$, one derives the approximate ground state ϕ_{gs} by:

$$\phi_{gs} e^{-(E_{gs}-E_T)\tau} = \int_{R_1}\int_{R_2}...\int_{R_N} G(R_N, R_{N-1})G(R_{N-1}, R_{N-2})... \\ G(R_1, R_0)\phi_I(R_0)dR_0dR_1...dR_N \tag{1.45}$$

The GFMC approach will still suffer from the negative weight problem. To fix this problem, a further approximation is applied to fix the nodes of the wavefunctions in each step to be the same as the initial wave-function. This gives an upper bound of the ground state energy calculated with the wave-function derived from the GFMC method.

1.4 The Unitary Fermi Gas

1.4.1 The Cold Atoms

Cold atoms are atoms (Li, K, Rb, etc) trapped in an optical or magnetic trap (or using both) [40] and cooled to very low temperature. The nano-Kelvin temperature is so low that the atoms together display quantum coherence phenomena not seen in normal temperature gases. They do not exist in nature, as the ground state of atoms at such temperature is a solid rather than a gas. However, because of experimentalists' capabilities to tune the atoms' interaction, flip their spins, disturb them with lasers, and image them directly, the cold atom systems are ideal tools to mimic and study the interacting quantum systems in nature. Examples of this are superfluid systems from liquid Helium 3 and 4, superconducting materials, nuclei and neutron stars, and high energy systems like the color superconductivity in quark plasma [13]. Furthermore, its ease to tune the system's interaction parameters

its clean, simple composition (one atom species with short range interaction) and point interactions enables us to verify some theoretical models. Examples of this are the 1-d Tonks-Girardeau gas [41], the BCS models, or just the non-interacting Fermi gas. In short, the cold atom system is one of the most powerful experimental tools available at present to study non-relativistic interacting quantum systems.

Depending on the total spin of the atom (electronic spin and the nuclear spin) cold atoms can either be bosons, fermions, or mixture of them. The bosonic BEC condensate was first realized in 1995 [4]. The fermionic degenerate gas, due to the Pauli blocking that makes the cooling processes more difficult, was not realized until 1999 [24]. The next breakthrough on manipulating the gases was the realization of using Feshbach resonance [26] to tune the interaction between the atoms.

For fermionic atoms in particular, the ability to tune the interaction between the fermions via Feshbach resonance enabled experimentalists to explore from the weak attractive BCS regime to the strongly interacting unitary regime, and eventually to the molecular BEC regime. The change of the fermi gas properties throughout these regimes is called the "BCS-BEC crossover". Throughout the crossover, various different physical properties have been studied. Examples of this are the equation of states [6], excitation spectrum, collective excitations [57], expansion and rotation [66]. As the trapped superfluid gas became larger and more stable, the dynamical behavior of the superfluid state are investigated. Examples of this are the creation of quantized vortices through laser stirring the cloud [90], or the formation of shock waves by collision of two [37] fermi clouds.

Recently, other different topics are also under exploration. Examples of this are the polarized gas (unequal number of spin-up and spin-down) [65], usage of optical lattice in the trap [3], and some intriguing features of different fermi gas mixtures [74].

1.4.2 The Unitary Fermi Gas

For a dilute fermi gas in the cold atom experiment, the inter-particle distance is typically in the order of μm [40]. this distance is much larger than the interaction potential range

r_0, which has a typical order of angstroms. In terms of fermi vector one has the inequality:

$$k_F \cdot r_0 \ll 1 \tag{1.46}$$

In such case the interaction can be regarded as the contact interaction and is characterized only by the scattering length a. Furthermore, one can tune the interaction, which is equivalent to tuning the scattering length corresponding to the contact interaction, by Feshbach resonance. When one tunes the interaction so that the scattering length is very large compared to the inter-particle distance:

$$k_F \cdot a \gg 1 \tag{1.47}$$

the only parameter of the interaction potential, a, can be regarded as infinite. As a result, the system becomes insensitive to the details of the interaction, and we call this particular fermionic system as the "unitary fermi gas".

An important property of the unitary fermi gas is the so called "universality" [34]. Since the interaction is point-like while the only parameter of the interaction, the scattering length, goes to infinity, the only physical variable (besides some constants) entering the system is the density, or equivalently the fermi energy. More specifically, this means that in a homogeneous space one has

$$E/N = \frac{3}{5}\xi_S \epsilon_F \tag{1.48}$$

$$\mu = \xi_S \epsilon_F \tag{1.49}$$

$$\Delta = \eta \epsilon_F \tag{1.50}$$

Δ is the pairing gap used to describe superfluidity, and μ the chemical potential. Universality implies that ξ_S and η are constant. Such universality is especially convenient for applying density functional theory to a fully paired unitary system. The reason is that the coefficients in each functional term will have densities as the only variables, which are therefore easier to determine through the fitting process. Universality also implies that theories of unitary fermi gases are applicable to systems with dramatically different scales of Fermi

energy (ex: neutron stars to dilute fermi gases) as long as they satisfy the unitary fermi gas properties.

From a physical viewpoint, the superfluid unitary fermi gas has the strongest fermionic superfluid properties in nature. As a result, the value η is of order unity. This means that the critical temperature of superfluidity is also of the order of the fermi energy. As a result, it is easier to realize superfluidity at the unitary regime compared to the BCS regime, which has the critical temperature exponentially smaller than the fermi energy. Moreover, the size of the Cooper pair, which is determined by the coherence length of order $\frac{\hbar k_F}{m\Delta}$, is also at the order of the inter-particle distance. This means that for a unitary system the superfluid as well as its normal component are both strongly interacting.

1.4.3 Density functional description of the fully-paired unitary fermi gas

As discussed in previous section, in the DFT formalism we first need to determine the density functional form of the unitary gas. We adapted the strategy in [54] to use both particle density $n(\vec{r})$ and anomalous density $\nu(\vec{r})$. We also used local density approximation instead of a non-local potential energy functional. To the lowest order, the energy functional has a kinetic term T and a correlation energy term E_c that existed even in the normal state, and is thus dependent on the particle density. Lastly, it also has an anomalous term E_p from superfluidity, and it depends on the magnitude squared of the anomalous density because the energy was a scalar.

Using dimensional analysis with combination of $n(\vec{r})$, $\nu(\vec{r})$, and the fully-paired system assumption, we get the energy functional of the unitary fermi gas as

$$E_{UFG} = \int d\vec{r} \left[\alpha \frac{\tau(\vec{r})}{2} + \beta \frac{3(3\pi^2)^{2/3} n^{5/3}(\vec{r})}{10} + \gamma \frac{|\nu(\vec{r})|^2}{n^{1/3}(\vec{r})} + V_{ext}(\vec{r}) n(\vec{r}) \right] \tag{1.51}$$

where α, β, and γ are dimensionless parameters to be fixed. As in [54] one has

$$n(\vec{r}) = 2\sum_k |v_k(\vec{r})|^2 \tag{1.52}$$

$$\tau(\vec{r}) = -2\nabla^2 n(\vec{r}) \equiv 2\sum_k |\nabla v_k(\vec{r})|^2 \tag{1.53}$$

$$\nu(\vec{r}) = \sum_k v_k^*(\vec{r})u_k(\vec{r}) \tag{1.54}$$

where the $u_k(\vec{r})$ and $v_k(\vec{r})$ come from the Bogoliubov transformation of the quasi-particle operator [60]. The index k sums over all the positive energy states (the negative energy states, in a fully paired system, were counted by the factor 2), and the energy states are determined iteratively by solving the Kohn-Sham eigen-equation.

For contact interaction in superfluid system, however, it was well known that individually the kinetic term τ and anomalous term E_p diverge but together they produced a finite value. As a result, numerically one could only calculate the terms in Eqn.(1.54) up to a certain energy cutoff E_c. Moreover, to maintain correct value of Eqn.(1.51) one has to renormalize the functional [17]. Doing so one derives the new expression for the energy functional as:

$$\begin{aligned}
E_{UFG} &= \int d\vec{r}\left[\alpha\frac{\tau_c(\vec{r})}{2} + \beta\frac{3(3\pi^2)^{2/3}n_c^{5/3}(\vec{r})}{10} + g_{eff}|\nu_c(\vec{r})|^2 + V_{ext}(\vec{r})n_c(\vec{r})\right] \\
g_{eff}^{-1} &= \frac{n_c^{1/3}}{\gamma} + \Lambda_c(\vec{r}) \\
\Lambda_c &= -\frac{k_c(\vec{r})}{2\pi^2\alpha}\left[1 - \frac{k_0(\vec{r})}{2k_c(\vec{r})}\log\frac{k_c(\vec{r})+k_0(\vec{r})}{k_c(\vec{r})-k_0(\vec{r})}\right] \\
E_c &= \sqrt{\left(\frac{\alpha k_c^2(\vec{r})}{2} + U(\vec{r}) - \mu\right)^2 + \Delta^2} \\
0 &= \frac{\alpha k_0^2(\vec{r})}{2} + U(\vec{r}) - \mu \\
n_c(\vec{r}) &= 2\sum_{E_k<E_c} |v_k(\vec{r})|^2 \\
\tau_c(\vec{r}) &= 2\sum_{E_k<E_c} |\nabla v_k(\vec{r})|^2 \\
\nu_c(\vec{r}) &= \sum_{E_k<E_c} v_k^*(\vec{r})u_k(\vec{r})
\end{aligned} \tag{1.55}$$

To get the Kohn-Sham equation similar to Eqn.(1.36) one has to vary the energy func-

tional Eqn.(1.55) with respect to u_k and v_k. However u_k and v_k are related by Eqn.(1.26), so one can only vary one of them. Doing so we derive the Kohn-Sham equation that has a form very similar to the Bogoliubov-deGennes equation [29]:

$$\begin{pmatrix} h(\vec{r}) & \Delta(\vec{r}) \\ \Delta^*(\vec{r}) & -h^*(\vec{r}) \end{pmatrix} \begin{pmatrix} u_k(\vec{r}) \\ v_k(\vec{r}) \end{pmatrix} = \epsilon_k \begin{pmatrix} u_k(\vec{r}) \\ v_k(\vec{r}) \end{pmatrix}$$
$$h(\vec{r}) = -\alpha\frac{\nabla^2}{2} + U(\vec{r}) \tag{1.56}$$

with $U(\vec{r})$ and the "pairing field" $\Delta(\vec{r})$ as

$$\begin{aligned} U(\vec{r}) &= \beta\frac{(3\pi^2 n_c(\vec{r}))^{2/3}}{2} - \frac{|\Delta(\vec{r})|^2}{3\gamma n^{2/3}(\vec{r})} + V_{ext}(\vec{r}) \\ \Delta &\equiv -g_{eff}(\vec{r})\nu(\vec{r}) \end{aligned} \tag{1.57}$$

and the time-dependent equation has the same form as in 1.38.

The last step we need to complete the DFT description is to determine the parameters α, β, and γ. Since the unitary fermi gas is a strongly interacting system, there is no exact method to analytically calculate the parameters. Instead we use the result calculated from the quantum Monte Carlo results [20] for the homogeneous unitary fermi gas. By fitting η, ξ_S defined in Eqn.(1.50) and the single quasi-particle spectrum

$$\epsilon_k = \alpha\frac{k^2}{2} + U - \mu = \alpha\frac{k^2}{2} + U + \left(\beta - \frac{(3\pi^2)^{2/3}\eta^2}{6\gamma} - \xi_S\right)\epsilon_F \tag{1.58}$$

to the Monte Carlo result, we determined the best fit as:

$$\alpha = 1.14 \tag{1.59}$$
$$\beta = -0.553 \tag{1.60}$$
$$\gamma^{-1} = -0.0906 \tag{1.61}$$

Further checks to see if the approximation we made (lowest term, LDA) to the density functional is appropriate for describing finite systems are done in [12] and in [15]. The

calculations show very accurate results compare with the Monte-Carlo results. From here on we will call our DFT formation for the unitary fermi gas the “Superfluid Local Density Approximation” (SLDA).

1.4.4 Vortices and Solitons

When we have a system with large number of fermions and in spatially uniform ground state (or smoothly varying in space), we naturally think that the low excited state should also be “almost uniform”: that is, we anticipate that the excitation has a wave-like, small-amplitude distortion throughout the space. And indeed there are such kinds of excitations like the excited quasi-particles in a fermi liquid, the sound (phonon) mode, and the spin-density wave in a ferromagnetic system. However, in nature there exists also low excited states that are spatially localized even though the ground state is uniform. Such excitations exist both in classical mechanics and in quantum mechanics. One example in classical mechanics is the ”solitary waves” first discovered by John Scott Russell in the Union Canal in 1834. If we are able to describe the system with some “orders” such as the spin direction in ferromagnets, angular momentum, or the pairing field in superfluid system, these localized states often have a discrete or abrupt change of order in their structures. Such abrupt change of order makes them almost stable and have relatively long lifetime against thermal or quantum fluctuation. Since these excitations are like “defects” within the uniform ground state, and they can be classified by topological theory [51], we call these excitations “topological defects” or “topological excitations.

Below we will introduce two types of topological excitations observed in our studies gases: the quantized vortices and solitons.

Quantized Vortices

Vortex is a structure that sustains circulation of flows around a center. In nature we see vortices in a pond stirred by water flow Fig.(1.2) , in air as tornado, or in the turbulence state of the smoke from a cigarette. In superfluid unitary fermi gas there are also vortices, but they are very different from classical vortices. Classical vortices can sustain any amount

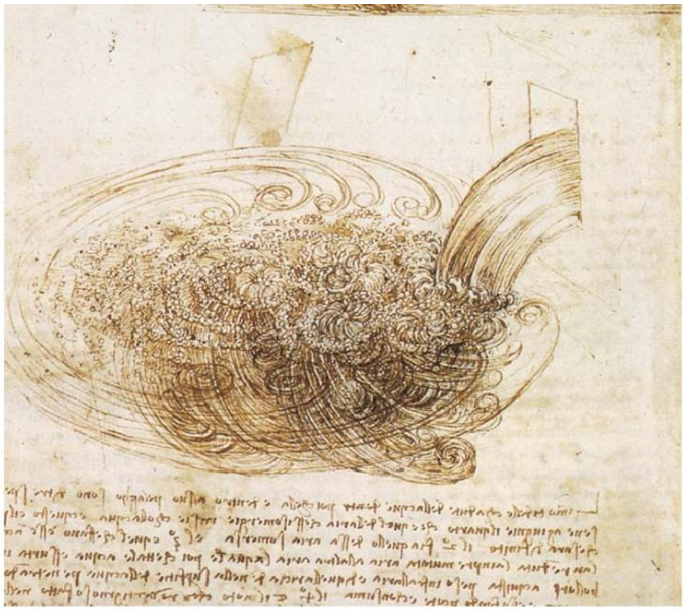

Figure 1.2: Water flow study by Leonardo Da Vinci [86]

of circulation around one vortex, and they are slowly dissipated by resistance in the flow. For quantum vortices in superfluid unitary fermi gas, on the other hand, the circulation is quantized, and the vortex will not decay unless it interacts with other excitations or objects. Mathematically one represents the the "order" of superfluid by the complex pairing field as $\Delta(\vec{r}) = \Delta_0(\vec{r}) \exp(i\theta(\vec{r}))$. It has the superfluid velocity as $v_s(\vec{r}) = (\hbar/m)\nabla\theta$. Because the pairing field needs to be single-valued everywhere in the system, the circulation κ becomes quantized:

$$\kappa \equiv \oint v_s(\vec{r}) \cdot dl = \frac{h}{m} n \tag{1.62}$$

where n is an integer. The energy of the vortex is roughly contributed by two parts: the part from the core and the part outside of the core . For a straight vortex of length l its energy is

$$E_v = E_{core} + E' \approx E_0 + \int_{r_a}^{r_b} \rho_s v_s^2 r dr = E_0 + c_0 n^2 \log \frac{r_b}{r_a} \tag{1.63}$$

where r_a is roughly the size of the core, and r_b is the size of the whole system. We see that the energy depends on n^2. As a result, as long as the generated vortices are not too closely packed with each other, it is energetically favorable to have more vortices of unit quantization than fewer vortices with quantization larger than one.

The detailed structure of a single vortex depends on the details of the interaction. For the unitary fermi gas, Bulgac and Yu [18] worked out the pairing field and the density profile of a vortex (see Fig.1.3 and Fig.1.4). They found that there is a density depletion inside the core, and this implies that one might be able to directly visualize the vortices inside the trapped fermions by observing the light contrast from density difference inside and outside of a vortex. On the other hand, the density, unlike the the density of a BEC vortex, does not go to zero in the center. This implies that in a superfluid fermionic system vortices have normal components inside the cloud.

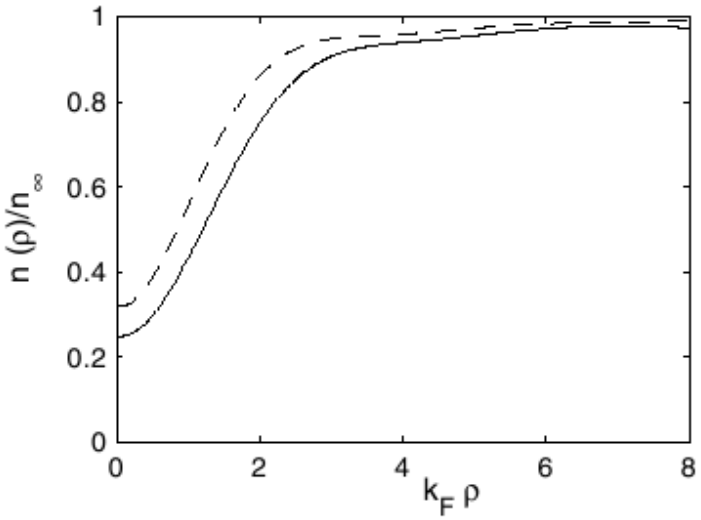

Figure 1.3: The normalized density profile of a vortex. From [18]

We now consider a system with many vortices. For vortices far away from other vortices' core there is a Magnus force acting on each vortex:

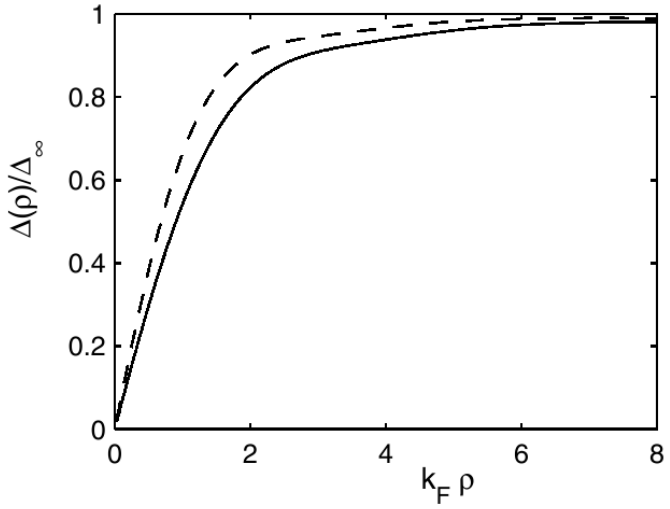

Figure 1.4: The normalized pairing profile of a vortex. From [18]

[70]

$$F = \rho\vec{\kappa} \times (\vec{v_V} - \vec{v_s}) \tag{1.64}$$

Eqn.(1.64) tells us that that for two parallel, straight vortices initially hold close to each other, they repel each other to a certain distance and then rotate with respect to the center of the two vortices. When there are so many packed vortices the forces between them are repulsive, and the vortices are packed as if they are many rigid cylinders. Analog to the closest packing theory for metals [42] they form the closest packed lattice, the triangular lattice.

When vortices are curved and dense they have the chance to collide with each other. When they collide they can twist and even reconnect with each other. Because the collision process involves the core contacting with another core, the dynamics depend on the detail structure of the vortices in this system. The separation and connections of the vortices can be complicated. However, when there are so many vortices tangled and interacting with each other, the system enters a state called "quantum turbulence". The energy spectrum of such state is believed to show some characteristic power-law behaviors: from low to

high momentum regimes the spectrum shows the classical Kolmogorov $-5/3$ spectrum, a transition regime, then a quantum regime described by power coefficient different from that of the classical value (see Fig. 1.5) [76].

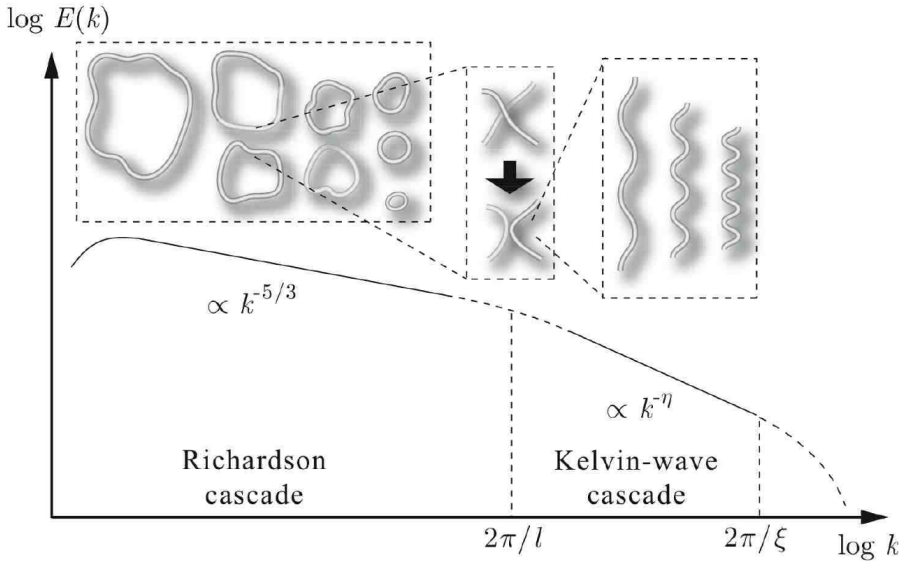

Figure 1.5: The energy spectrum of a quantum turbulence state. l is the inter-vortex spacing and ξ is the coherence length corresponding to the vortex size. For k below l the spectrum follows classical Kolmogorov spectrum with a power of $-5/3$. Above l the spectrum characterizes the "Kelvin wave cascade", which the energy is transferred from long Kelvin waves to short ones on a vortex. Above ξ, the energy is dissipated by phonons. From [76]

Solitons

Besides quantized vortices, solitons are another group of localized excitations that exist in quantum fluids.A single soliton's structure is like a "localized bump/valley" with density variation concentrated/depleted near a plane that moves in one direction. Furthermore, the solitons have unique structures that prevent them from gradually dispersing and vanishing in the medium. As a result, they can propagate in the medium for a long time without dispersion and dissipation. This property distinguish solitons from other nonlinear wave phenomena like shock waves. Despite its exotic name, solitons are quite common in nature,

existing in many physical systems in oceans, atmosphere, plasma, and even light.

In a cold atom system, based on the density variation the soliton can be classified into two groups. The first group is the bright soliton, where there is a concentration of density in the middle of the soliton. The second group is the dark/grey soliton, where there is a depletion, with dark soliton being stationary, and grey soliton moving. Both types of soltions have been observed in the BEC condensate [89] [67], and the dark/grey soiltons recently observed in fermion gases [69]. The dark/grey soliton has been theoretically investigated in [5] [64] in a unitary fermi gas system, and the bright solitons were investigated in [48] for the bose-einstein condensate. Since only the dark/grey solitons are associated with a discrete phase change across their structures similar as the quantized vortices, below we only describe the properties of dark/grey solitons, and we will defer the bright soliton discussion to a later chapter.

As mentioned above, like vortices the stationary dark solitons in a unitary fermi gas have a discontinuity of phase change $\delta\Delta = \pi$ in the complex pairing field. However, unlike vortices that have a discrete quantized number associated with them, solitons have no such number. As a result, when a dark soliton moves and become grey, the phase change can evolve gradually from π to zero when its speed reaches a critical value and the soliton dissipates [1]. In three dimensional trap, a dark/grey soliton, being a two dimensional object, can decay into other topological defects such as a pair of vortex and anti-vortex via the "snake instability" effect [89]. Thus compare to the quantized vortices, the solitons are more unstable and harder to be observed in the experiment.

The density profile of the dark soliton is showed in Fig.(1.6) [5]. It has a dip in the middle and some small oscillation at the boundary. Since the equation used to calculate the density structure ignored the normal component correlation energy, the structure in Fig.(1.6) should be regarded only as a qualitatively representation of the actually density profile.

As solitons are localized object propagating through the medium, we expect they move like classical particles. Thus within a one-dimensional harmonic trap a soliton can undergo harmonic oscillations with a definite period [64]. Unlike the classical bright solitons that collide elastically with just a shift in the space, the dark/grey solitons in a superfluid unitary

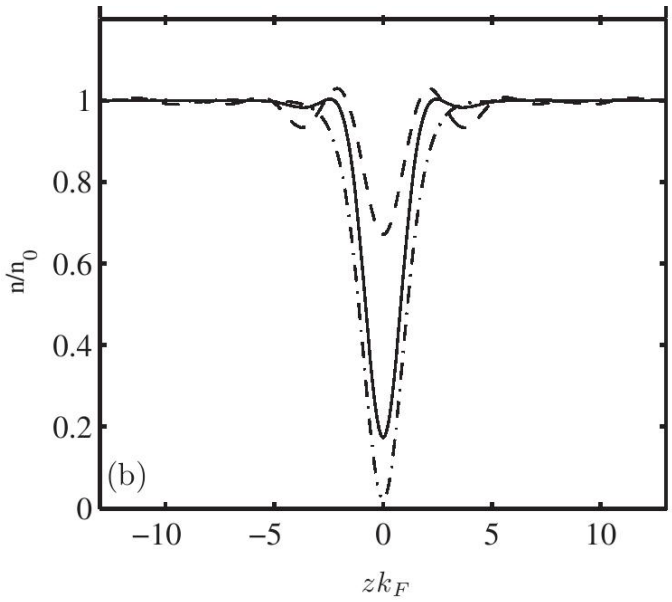

Figure 1.6: The density profile of a dark soliton [5]. The solid line is the density profile in the unitary fermi gas, while the dashed and dot-dashed lines were solutions in the BCS and BEC regimes.

gas system collide inelastically with themselves, with a localized "bump" potential, and with other bright soliton trains. When dark/grey solitons decay they generate trains of bright solitons into the unitary fermi gas. Throughout this dissertation we will call the dark/grey solitons as "domain walls" for its domain like structure in density and pairing plots. We will call the bright solitons as "soliton trains" because they always appear and propagate as groups in our simulations.

Chapter 2

SUPERFLUID DYNAMICS OF THE UNITARY FERMI GAS IN TWO DIMENSION

In this chapter we show the generation of the quantized vortex lattice, which were observed experimentally in superfluid fermion gases [90]. The dynamics during vortex generation, the critical velocity, the effect of the trap geometry, and the excited energy are discussed. These results were published in [16].

2.1 Introduction

The observation of quantized vortex lattice in [90] is a definitive proof that the unitary fermi gas below a certain critical temperature was superfluid. Like rotating spoons in a coffee cup, the experiment showed two blue-detuned (repulsive) lasers into the trapped cloud as stirring rods, stirred the cloud for some time, and then turned off. Several hundred milliseconds later they found vortices forming triangular lattice in the cloud (Fig.2.1).

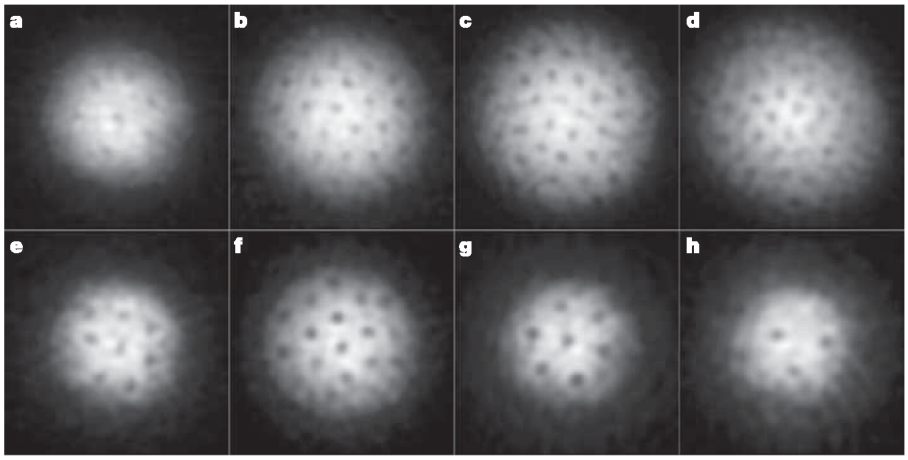

Figure 2.1: The vortex lattice images of various magnetic fields in a fermi gas system. The (e) image is at unitarity [90].

Theoretically one often uses Landau's two-fluid model [73] [46], the Gross-Pitaevskii (GP) equation [30] [55], or the classics Bogoliubov-deGennes (BdG) equation [29], to describe the dynamics of a superfluid. As we describe below, none of these theories can accurately describe the unitary fermi gas system. We will introduced our SLDA formation and see that it not only is able to generate quantized vortices without imposing artificial quantized condition, but also describe the whole transition from superfluid to normal system. Our SLDA formulation can also give insights to how the vortices are formed during the stirring process, which based on current experimental techniques, could not be observed without destroying the entire cloud.

2.2 Review on Classical Superfluid Dynamical Theories

In Chapter one we introduce some theories that describe static solutions of a superfluid system, such as the BCS equations in Eqn.(1.14) and the HFB theory in Eqn.(1.27). Here we will review some theories used to describe superfluid dynamics.

2.2.1 Landau's two fluid model

Landau's two fluid model [45] is a semi-classical model originally used to describe the dynamics of superfluid helium 4. They theory assumes that the superfluid system is composed of two liquid: the normal liquid ρ_n and the superfluid liquid ρ_s. Each fluid can move at different velocity. We thus have the total density and flux be:

$$\begin{aligned} \rho &= \rho_n + \rho_s \\ \vec{j} &= \rho_n \vec{v_n} + \rho_j \vec{v_j} \end{aligned} \tag{2.1}$$

In fluid dynamics the density and the flux satisfied the equation of continuity representing the conservation of mass. The fluid also satisfies the conservation of momentum and energy. With no dissipation and irrotational flow in zero temperature we get:

$$\begin{aligned}
&\frac{\partial \rho}{\partial t} + \nabla \cdot \vec{j} = 0 \\
&\frac{j_i}{\partial t} + \frac{\partial \Pi_{ik}}{\partial x_k} = 0 \\
&\frac{\partial v_s}{\partial t} + \nabla(\frac{1}{2}v_s^2 + \mu) = 0 \\
&\frac{\partial E}{\partial t} + \nabla \cdot \vec{Q} = 0
\end{aligned} \tag{2.2}$$

where i represents the axes for the three dimensions, Π is the momentum flux density tensor, Q was the energy flux density, and μ is the local chemical potential. Further calculations give:

$$\begin{aligned}
\vec{Q} &= (\mu + \frac{1}{2}v_s^2)\vec{j} + \rho_n \vec{v_n}(v_n^2 - v_n \cdot v_s) \\
\Pi_{ik} &= \rho_n v_{ni} v_{nk} + \rho_s v_{si} v_{sk} + p\delta_{ik} \\
p &= -E_0 + \mu\rho + \rho_n(\vec{v_n} - \vec{v_s})^2
\end{aligned} \tag{2.3}$$

where E_0 is the internal energy of the fluid. Once E_0 and μ are determined as functions of ρ_n, ρ_s, and $v_s - v_n$ the above hydrodynamics equations could be solved. If dissipation was considered, the equations in Eqn.(2.2) except the mass conservation needed to be modified by the viscous terms and three viscous coefficient ξ_1, ξ_2, and x_3. In a unitary fermi gas system the first two viscous coefficients are shown to be zero [71].

A fundamental problem of using Landau's two fluid model is that it does not have intrinsic quantization condition, or $\hbar$, in the formation. Therefore to simulate quantized vortices manual circulation restriction needs to be applied. As a result, such formation can not simulate spontaneous occurrence of various topological defects by exciting the system with external potentials. Another problem about Landau's two fluid model is that it does not consider quantum excitation of the system. As a result there is no superfluid critical velocity, and the system will not experience superfluid/normal state transition. Nevertheless, the two fluid model, with simplification of assuming ρ_n to be zero, is a simple yet powerful tool to study various nonlinear hydrodynamics behaviors in the unitary gases. Examples of this are the shock wave [37] and soliton trains [44].

2.2.2 Gross-Pitavinskii equation

The Gross-Pitavinskii (GP) equation [30] [56] describes the macroscopic wave-function of a weakly interacting Bose system:

$$i\hbar\frac{\partial\Phi(\vec{r},t)}{\partial t}=\left(-\frac{\hbar}{2m}\nabla^2+g|\Phi(\vec{r},t)|^2-\mu\right)\Phi(\vec{r},t) \tag{2.4}$$

The nonlinear term $g = 4\pi\hbar^2 a/m$ is proportional to the scattering length a of the system. $\Phi = \sqrt{\rho}\exp(i\theta)$ is the macroscopic wave-function such that its absolute value squared, $\rho = |\Phi|^2$, is the superfluid density, and θ is the phase describing superfluid velocity, $v_s = \hbar/m\nabla\theta$. The GP equation is useful to describe the dynamics in a dilute Bose gas [23]. Examples of this are quantized vortex dynamics [75], soliton generation [89], and the qualitative dynamical behaviors of liquid helium He^4. For a single quantized vortex state with the density at infinite normalized to 1, we get:

$$\Phi(\vec{x}) = f(r)\exp(i\theta) \tag{2.5}$$

With a natural scale $\xi = \left(\frac{\hbar^2}{2mg}\right)^{1/2}$ and the dimensionless parameter $\zeta = r/\xi$, $f(\zeta)$ satisfies

$$\frac{d^2f}{d\zeta^2}+\frac{1}{\zeta}\frac{df}{d\zeta}-\frac{1}{\zeta^2}f+f-f^3=0 \tag{2.6}$$

Fig.(2.2) shows the numerical solution of Eqn.(2.6) with boundary condition $\Phi(0) = 0$ and $\Phi(\infty) = 1$. Compared the pairing with the SLDA solution Fig.(1.4) we observe that they had the same linear function when ζ is small. However, the density profiles were completely different, as for the GP equation the density went to zero at the origin, while for the unitary fermi gas did not. As a result, GP can only qualitatively describe vortex dynamics in a unitary fermi gas system. Furthermore, it might not be qualitatively accurate when describing the reconnection of quantized vortices, as in the unitary fermi gas system it involves interaction of the normal fluid cores between different vortices. Nevertheless, due to its numerical simplicity (only single wave-function is involved in the equation, so the

variable numbers is only L^3), the GP equation and its modified versions are widely used to study quantum turbulence behaviors in quantum liquids [76] [32] .

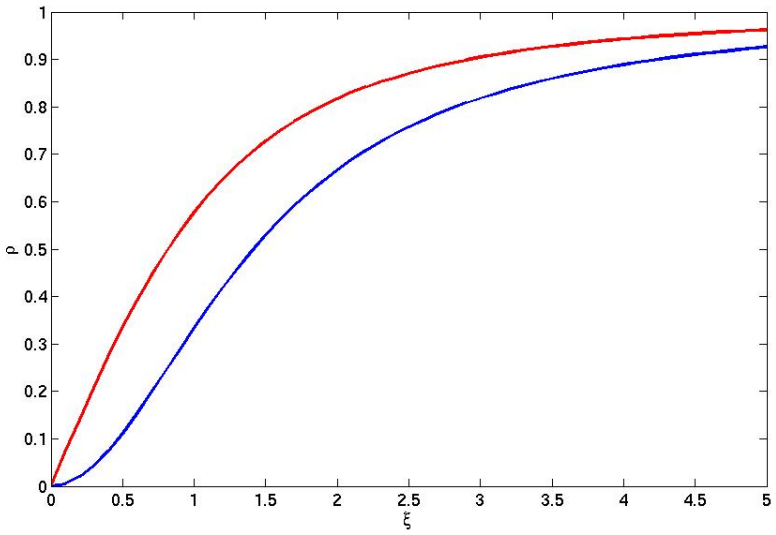

Figure 2.2: Approximated solution square of Eqn.(2.6). The red curve and blue curve show the pairing and the density radial profiles, respectively.

2.2.3 Time-dependent Hartree-Fock-Bogoliubov Equation

The mean-field Bogoliubov deGennes equation in Eqn.(1.27) can be generalized to a time dependent equation [38]:

$$\begin{pmatrix} h & \Delta \\ \Delta^* & -h^* \end{pmatrix} \begin{pmatrix} U_k \\ V_k \end{pmatrix} = i\hbar \frac{\partial}{\partial t} \begin{pmatrix} U_k \\ V_k \end{pmatrix} \tag{2.7}$$

where the matrix h includes only the kinetic and external (trap) potential terms:

$$h = -\frac{\hbar^2 \nabla^2}{2m} + U_{ext} - \mu \tag{2.8}$$

and the pairing potential Δ is calculated in a way similar to the BCS equation. Instead of having a physical cutoff of phonon energy as in the superconducting system [27], in the

unitary fermi gas system one typically specifies a cutoff energy E_c and associate the pairing coefficient g in $\Delta = g\sum_k u_k v_k$ to the scattering length a [66]. The result is:

$$\frac{1}{k_F a} = \frac{8\pi E_f}{g k_f^3} + \sqrt{\frac{4E_c}{\pi^2 E_f}} \tag{2.9}$$

$E_f = \frac{k_f^2}{2m}$ is the local fermi energy of an ideal fermi gas, and $k_f = (3\pi^2 n)^{1/3}$ with local density n. Such TDHFB formation can qualitatively simulate the various dynamics and topological excitation in a fermi gas system. Furthermore, by changing the value of the scattering length a, it can solve the dynamics across the BCS-BEC crossover [58]. However, the TDHFB does not include the correlation potential in h , and thus it is only quantitatively accurate for system with small scattering length. Numerically, TDHFB is also as complex as our SLDA formulation.

2.3 Simulation setup

2.3.1 unit and system size

We choose the lattice constant in the coordinate space and $\hbar/m$ be 1, with the position as well as the momentum described by a uniformly spaced grid. Since numerically the maximal resolvable wavelength is π, we choose a momentum cutoff to be $k_{cf} = \pi$ and it corresponds to an energy cutoff $E_c = \pi^2/2$. Let the number of grid points on each side be N_i, $i = \{x, y\}$, the momentum grid values then range from $-\pi$, $-\pi + 2\pi/N_i$ ..., 0 ,... to $\pi - 2\pi/N_i$. The value of $\{N_x, N_y\}$ is $\{32, 32\}$ and $\{48, 48\}$. The number of particles are chosen so that under Thomas Fermi approximation, the fermi vector k_F at the maximal density is about 1. Finally, to use Fast Fourier Transfer technique in our numerical calculation, the boundary condition is set to be periodic. We then minimize the effect of periodicity by imposing large potential barriers around the boundary of the space grid.

2.3.2 External potentials

To simulate a trapped UFG and to minimize periodic boundary effect, the particles are trapped in an external potential U_{ext}

$$
\begin{aligned}
r &= \min\left[\sqrt{\left(\frac{x}{N_x/2}\right)^2 + \left(\frac{y}{N_y/2}^2\right)}, 1\right] \\
U_{ext}(x,y) &= U_0 * \sin\left(\pi r/2\right)^{n_1} \\
U_0 &= 0.8 * E_c
\end{aligned} \tag{2.10}
$$

where (x, y) was measured from the midpoint, and $n_1 = 8$ for $N_x = N_y = 32$ and $n_1 = 20$ for $N_x = N_y = 48$. Such confining potential ensures the system is consistently periodic and smooth at the boundary. The reason for this is that we observe the discrepancy in periodicity and smoothness greatly decrease the numerical accuracy of our simulation. The value of U_0 at the scale of energy cutoff ensures that the wave-function over the trap boundary is exponentially small, so that again periodic effect is minimized.

For the time-dependent stirring potential U_{stir} we use a Gaussian profile potential that rotates around the trap's center:

$$
\begin{aligned}
e_F &= k_F^2/2 \\
r^2 &= \left[\left(x - R_s\cos\left(\omega t\right)\right)^2 + \left(y - R_s\sin\left(\omega t\right)\right)^2\right]/\sigma_r^2 \\
\sigma_r &= 2 \\
U_{\text{stir}}(x,y,t) &= e_F * F_{\text{time}}(t) * e^{-r^2}
\end{aligned} \tag{2.11}
$$

The values σ_r and e_F ensure that the stirring potential was not too strong and too sharp. The reason is that potentials that are too strong tend to excite the system too much and loss superfluidity, while potentials that are too sharp tend to decrease the numerical accuracy. $F_{\text{time}}(t)$ is a time-dependent on/off factor described below. In our simulation we use both one or two stirring potentials to stir the system.

2.3.3 Time scales in the system

The time step dt in the system is determined by the 5^{th} order Adam-Bashforth method used in the program to perform high time-stepping for first order differential equation over

time. Assuming that the maximal error coefficient in the method is E_c, we impose a limit that the 5th power of the product has to be smaller than a tolerance value c_t:

$$(E_c * dt)^5 \approx c_t \tag{2.12}$$

With $c_t \approx 10^{-7}$ we get $dt = 0.008067$. In general for double-precision calculations we need $c_t \approx 10^{-10}$, but we found that 10^{-7} is small enough to get good convergence in energy after the stirring process of the system.

For the time-evolving potential, to ensure that the system varies adiabatically, the on/off function $F_{\text{time}}(t)$ has the form:

$$F_{time}(t) = \left[\left(\frac{1 + \tanh\left(\frac{t - T_{\text{on}}}{\sigma_{t1}}\right)}{2} \right) \left(\frac{1 + \tanh\left(\frac{T_{\text{off}} - t}{\sigma_{t2}}\right)}{2} \right) \right]_t^n \tag{2.13}$$

where $n_t = 3$ and σ_{t1} and σ_{t2} are large compared to the time step. A typical function profile of Eqn.(2.13) is showed in Fig.(2.3). Typical values of σ_{t1} and σ_{t2} are $30/e_F$. The T_{on} value is also large compare to the time step with a typically value of $30/e_F$. These value ensure that initially F_{time} starts from a small enough value and the potential turned on adiabatically. T_{off} is determined by the number of rotations n_{stir} in the system and the stirring angular velocity ω_s:

$$T_{\text{off}} = T_{\text{on}} + n_{\text{stir}} * \frac{2\pi}{\omega_s} \tag{2.14}$$

Typical value of n_{stir} is 5. ω_s varies wildly.

The total time T_t to tun the simulation is about $T_t \approx T_{\text{off}} * 1.7$, which is almost twice of the time combined for the setup and stirring. This extra time enables the stirred system to stabilize and generate rotating vortex lattices.

2.4 Simulation method

The simulation process consists of two steps. First the ground state is determined by an iterative method (Broyden's method. See Appendix C). The program starts from a

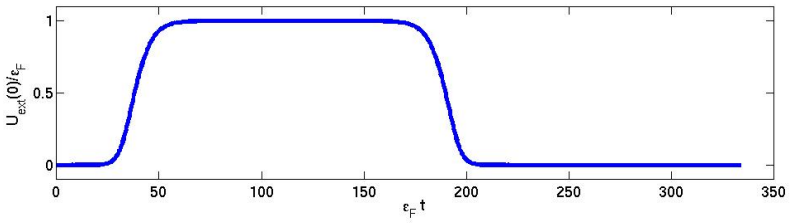

Figure 2.3: A typical function profile of F_{time}. The x-axes (time) is normalized by the Fermi Energy.

system of non-interacting fermi gas with either uniform distribution or distribution based on the Thomas-Fermi approximation, which we know the exact forms. Then HFB-like matrix, Eqn.(1.56), is constructed using Discrete Variable Representation (DVR. See Appendix C) and solved. After getting the eigen-functions and eigenvalues physical observables (density,pairing field, particle number and energy) are calculated from the resulting single-particle eigen-functions. Then using Broyden's method, the new and several old densities and pairing fields are mixed to suppress numerical oscillations and accelerate convergence. In order to reach the desirable number of particles, after each iteration the chemical potential is adjusted linearly by the deviation of calculated and targeted particle number. Finally, to exist from the iterative process, after each iteration (except the first) an error is calculated by subtracting the new and the previous chemical potential. If the error is smaller than a threshold (typically set to 10^{-12}) the program would exist from the iterative loop. It then writes out all the physical observables and the wave-functions of the converged system into several files to be used for time-stepping calculations. A typical converging behavior of our solver program was showed in Fig.(2.4). The error threshold is met typically after about 130 steps. Within the first few steps, an artificial external pairing field is required to break the normal-superfluid symmetry and enable the system to become superfluid. The flow chart of the ground state solver is shown in Fig.(2.5).

For the time stepping program, initially the wavefunctions and the potentials are read from the input files, and then the program uses a highly-accurate fifth-order Adam-Bashforth method to step through time (see Appendix C). Unlike the solver program, in each step the

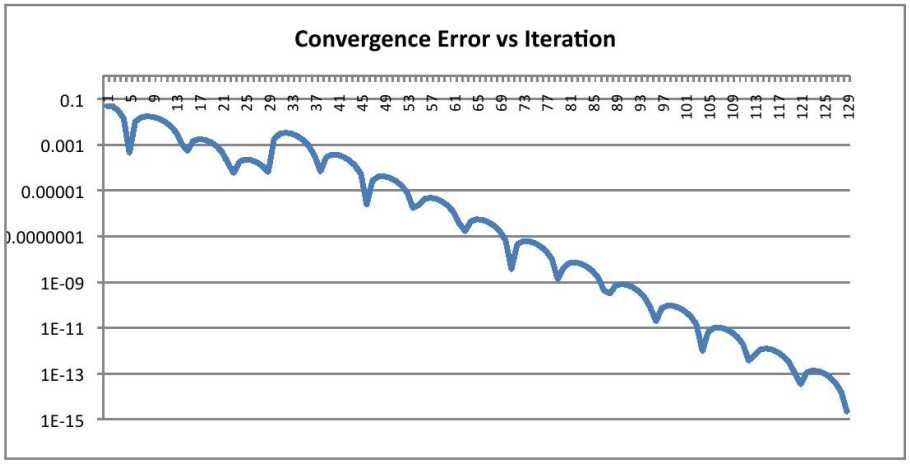

Figure 2.4: A typical error converging behavior of the SLDA solver (ground state calculation) program.

operators such as the deviation are directly applied to each wave-function using Fast Fourier Transformation. As a result there is no need to construct the entire HFB-like matrix in each time step. For every few tens or hundreds of steps the physical observables are computed and written into files. The time stepping process then either runs to finish time or to a designated run time. In the latter case it performs a checkpoint and dumps all the current running data into the disk for restart in later time. The flow chart of the time stepping process is shown in Fig.(2.6).

2.5 Results

2.5.1 Energy Profile

A typical energy profile versus time throughout the process of a stirring simulation is shown in Fig.(2.7). Initially the energy remains constant, and then it increases when the stirring potential enters the system. It then fluctuates and increases slowly during the stir process, and decreases a little once the stirring potential is pulled out of the system. Finally the energy remains constant (within fluctuation of about $10^{-}3$ in the raw data) while the system stabilizes into vortex lattice. The stabilization of the energy is an indicator of whether the stirring process is smooth enough to allow for an adiabatic transformation of the system.

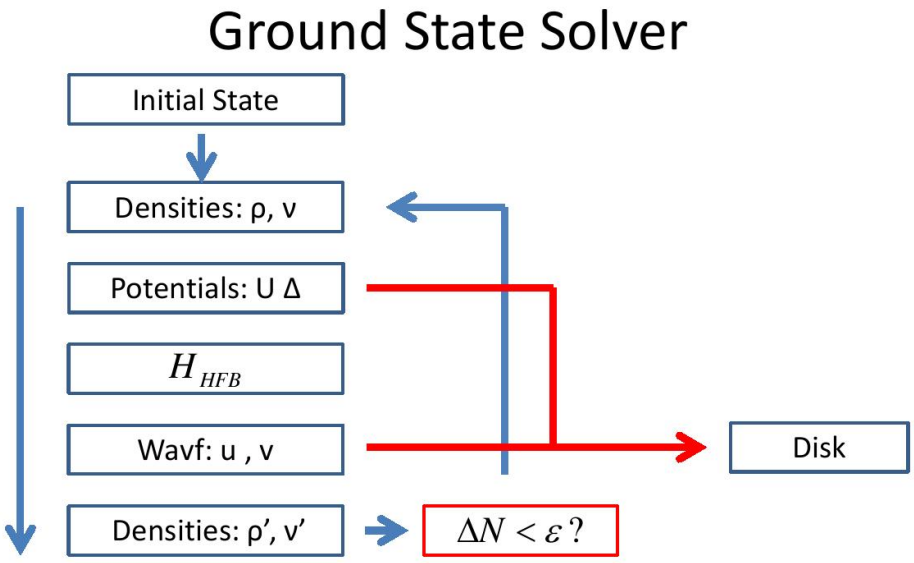

Figure 2.5: Flow chart of the ground state solving process.

It also indicates that the system does not generate too many highly-excited single particle states with wave vector higher than the maximal number π. If either of these conditions are violated the energy will diverge exponentially at the end of the simulation.

2.5.2 Generation and Destruction of Quantized Vortices

Fig.(2.8) shows the pairing potential magnitudes of different vortex generating stages in a 48 by 48 lattice, with rotating speed of $0.45k_f$ and the rotating orbit radius $r = 10$. Initially the superfluid system is mostly uniform in the trapping potential. Then a repulsive, cylindrical shape stirring potential, indicated as the round dark blue region about 2 o-clock location in the upper left subplot, is introduced into the trap and stirs the unitary gas clockwise. As the rotating potential rotates the superfluid unitary gas is strongly compressed, and is accumulated in front of the stirring potential. This creates a large red region in the upper left and upper right subplots. At the back of the stirring potential the unitary gas is depleted by the stirring potential. This creates a low density, dark blue region in the subplots. This dark blue region is connected to the boundary of the trap, and it enables vortices to enter the system from the boundary. Initially the vortices appear as a large lump of low pairing

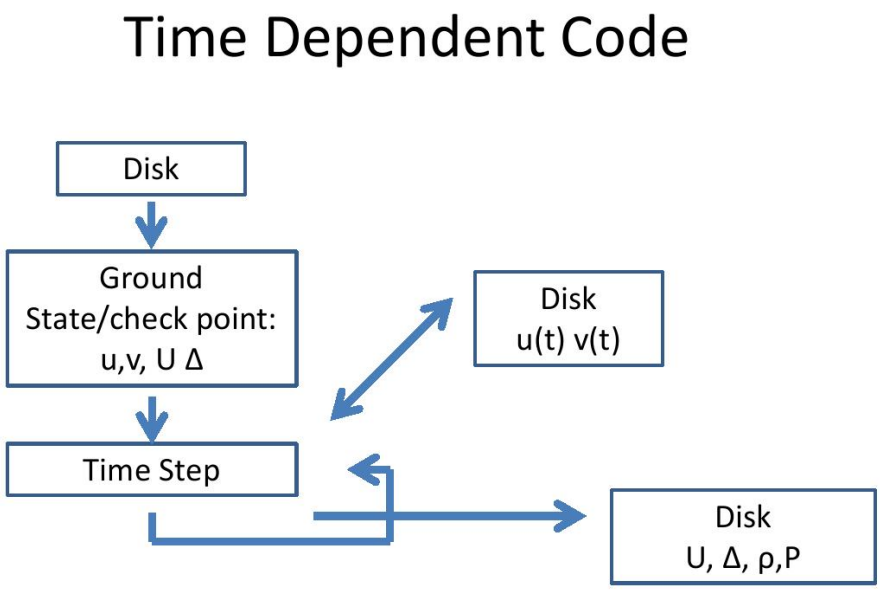

Figure 2.6: Flow chart of the time-stepping process.

density region as shown in the upper right subplot. As the stirring potential is pulled out of the system, they repel each other into individual vortices, each with a single quantized angular momentum. such process is shown in the down left subplot. Finally the vortices adjust their relative distances and form a rotating triangular vortex lattice, which is shown in the down right figure.

Fig.(2.9) shows the final stage of Fig. (2.8) from 4 simulations with the same geometric setup but with different stirring angular velocities ω, which ranges from 0.1667 to 0.675 and has unit as k_f/L. One observes that by varying different angular velocities, our SLDA formulation can simulate a series of states with different quantization conditions. From very weak velocity it generates a system no vortices at all. Then increasing the velocity over a threshold it generates systems with more and more vortex numbers up to 13. Finally it can overstir the system and destroys superfluidity, creating a giant normal fluid vortex in the middle of the trap. All these are simulated with the same underlying theory and only with different external potentials.

The strong compressibility of the unitary gas system shown in Fig.(2.8) can explain one

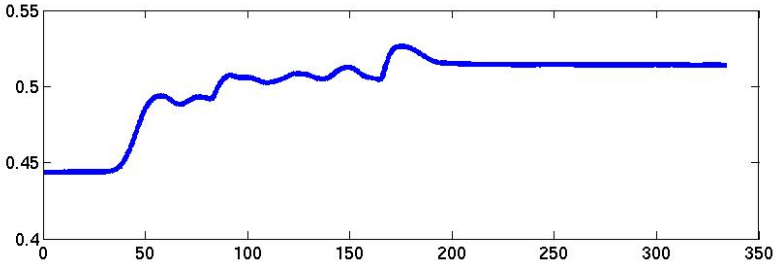

Figure 2.7: A typical energy profile versus time during the entire stirring process. The x-axes (time) is normalized by the Fermi Energy. The y-axes is normalized to the energy of a non-interacting uniform system that contains the same amount of particles to the unitary system.

observation that, at first sight, is controversial to the result in Fig.(2.9) . The critical Landau critical velocity v_s (the velocity in which the system loses superfluidity) in the unitary fermi gas system is, according to [57], the lower value of either the sound velocity or the minimal fluid velocity that broke Cooper pairs. Mathematically this is represented as:

$$V_s = \min\{c_s, (\sqrt{\Delta^2 + \mu^2} - \mu)^{1/2}\} \tag{2.15}$$

c_s is the speed of sound in the unitary system and Δ, μ are the local magnitude of the pairing potential and the chemical potential. Using Eqn.(1.50) and the values in [12] we derive the critical velocity as:

$$v_s \approx 0.365 v_f \tag{2.16}$$

where $v_f = k_f/m$ is the Fermi velocity, which in our simulation k_f/m for the initial state is almost 1. If we just look at the final state as in Fig.(2.9) we observe a controversy: with a stirring velocity at the stirrer of $\omega R = 0.45$ the system will lost superfluidity. However we observe that in the final state it still contains quantized vortices. This controversy can be remedied by studying the superfluid dynamics during the stirring process in Fig.(2.8). During the simulation we observe that due to the large compressibility of the unitary gas, the particle density $\rho(\vec{R})$ in front of the stirrer is more than twice as dense as the density in

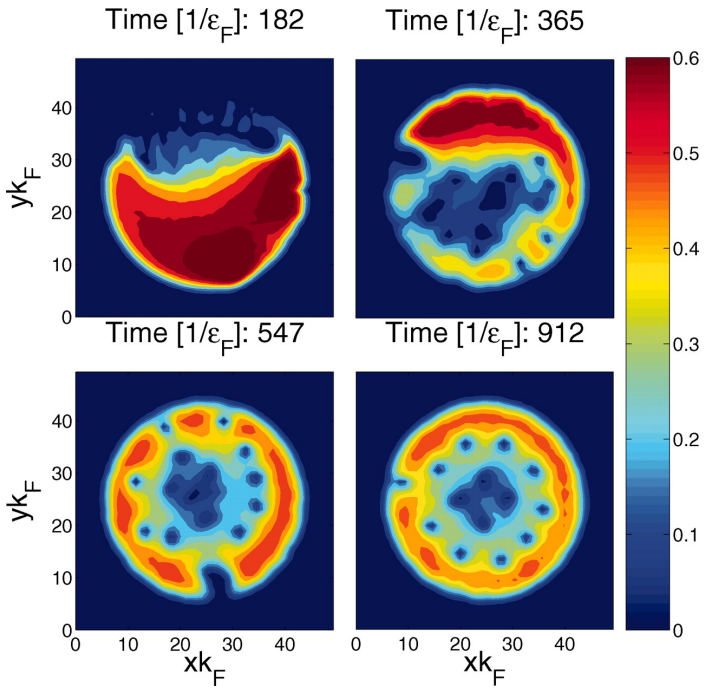

Figure 2.8: The pairing potential magnitude of the several stages of the vortex generating process in a 48 by 48 lattice, with rotating speed of $0.45k_f$ and the rotating length $r = 10$. The superfluid system is stirred by a repulsive, cylindrical shape stirring potential clockwise, and it is indicated as the round dark blue region about 2 o-clock location in the upper left subplot. The gas is largely compressed as shown in the plot as the red regions in front of the stirring potential. It is also depleted at the back of the stirring potential, which is shown in the plot as the dark blue region. The dark blue region later separates into 13 quantized vortices and forms a triangular vortex lattice.

the initial state. Since the local Fermi vector $v_f(\vec{R})$, under Thomas-Fermi approximation, is proportional to $\rho(\vec{R})^{1/3}$, the effective critical velocity $v_f(\vec{R})$ near the front of the stirrer at location $\vec{R}$ will than be large than $v_s * 2^{1/3} \approx 0.46$. This value is above the stirring velocity at the stirrer, and as a result the superfluidity is preserved.

In summary, these simulations show several significant advantages of our theoretical model. First they proved our SLDA theoretical formulation, which was derived from ab-initio properties of the static unitary gas, can accurately describe the unitary gas experiment in [90]. Second they enable us to examine the dynamics of the generation process, which are not shown in the experiment due to the destruction after imaging the cloud. Examples of

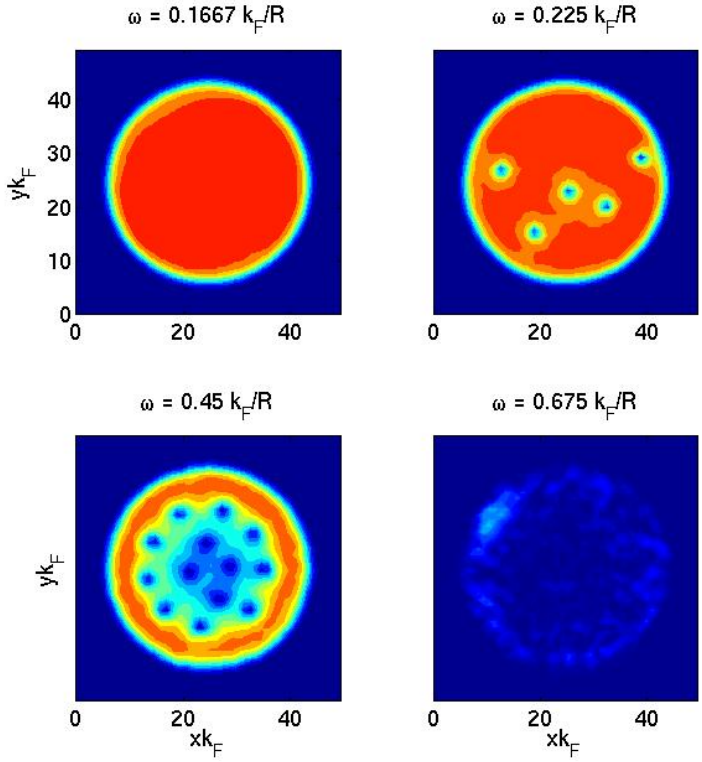

Figure 2.9: The pairing density of the final state of various unitary gas simulations with different stirring angular velocities. With small enough velocity the system does not generates any quantized vortices. With increasing velocity the number of vortices generated increases. Finally with sufficiently large velocity the superfluidity is destroyed, and the system became normal, leaving no quantized velocity in the system.

this are the strong compression of the unitary gas and the organization of the vortices into a lattice. Finally the capability to transit from a superfluid system with no vortices, to a superfluid system with vortices, and to a normal system with no superfluidity demonstrate that our SLDA formulation could describe accurately various adiabatic, dynamical processes in a unitary gas system. The process can be either in a superfluid state, in a normal state, or a state mixed with super and normal fluid.

2.5.3 Effect of Non-symmetric Geometry

In the vortex generation experiment [90] the authors observed that *"The roundness of the optical trap and its alignment with both the optical stirrer and the axes of the magnetic potential were critical [to quantized vortex production]"*. We will like to study these effects in our 2-D simulation.

Fig.(2.10) shows the pairing density of a set of simulations in a 48 by 48 lattice with ellipsoidal traps. The ratio of axes in these simulations is $3:2$, the stirring radius $R = 10$, and the stirring velocity varies. Compare with Fig.(2.9) we observed that the effect of changing the roundness of the trap significantly reduces the number of generated vortices. Moreover, with an ellipsoidal trap, the amount of superfluid (represented as the pairing density magnitude) in the system is significantly reduced even in the presence of quantized vortices.Finally, we observe that the superfluidity is completely lost with a lower value of stirring angular velocity compared to the round trap simulations.

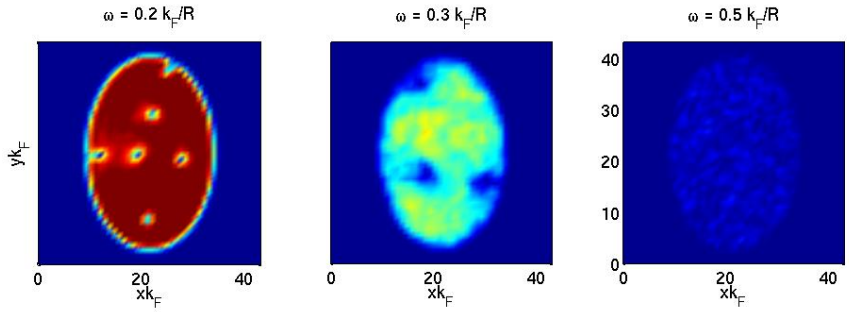

Figure 2.10: The pairing density of a set of simulations in a 48 by 48 lattice with ellipsoidal traps, with the ratio of axes be $3:2$, stirring radius $R = 10$, and stirring velocities be 0.2, 0.3, and 0.5. One observes that even when the angular velocity is only $\omega = 0.3$ the pairing density already turns blue and shows significantly lost of superfluidity in the system. For $\omega = 0.5$ the superfluidity is already destroyed.

Fig.(2.11) shows the pairing density of a set of simulations in a 48 by 48 lattice with perfectly round traps and with the stirring radius $R = 10$. However, the center of the stirrer is offset by 3 unit length to the right of the trap center, and the stirring velocity in each simulation differs. Compare with Fig.(2.9) we observe that surprisingly the number of

quantized vortices does not continue increasing until the system loses superfluidity: instead it peaks with a certain stirring velocity around $\omega = 0.3$.

The reduction of quantized vortices and superfluidity observed in these simulations can be explained as follows: with non-perfect roundness and centrality, the stirrer is less effective at introducing circular flows (angular momentums) into the system and maintained largely compressed gas at the front of the stirrer. As a result, more phonons are created that could interact and reduce the number of quantized vortices, and the lower density near the stirrer results into lower critical velocity. Together this makes the system lose superfluidity with a lower stirring velocity and limit vortex generation up to a certain stirring velocity.

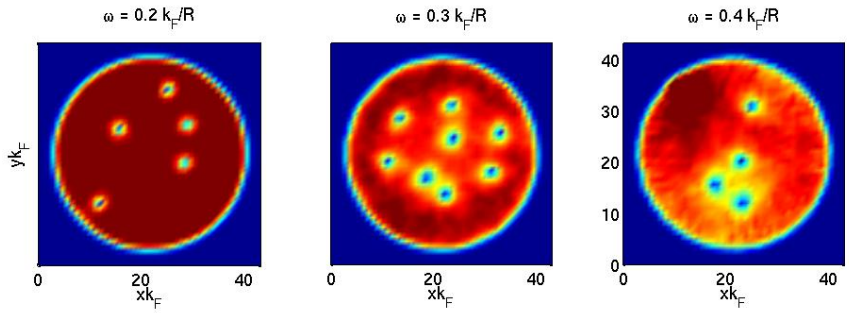

Figure 2.11: The pairing density of simulations in a 48 by 48 lattice with perfectly round traps and the stirring radius $R = 10$. The stirring center offsets of length of 3 units to the trap center and the stirring angular velocities vary from 0.2, 0.3, and 0.4. One observed that the number of quantized vortices increased from 5 to 8 when the angular velocity increased from 0.2 to 0.3, but dropped to 4 from 0.3 to 0.4. The color also shows that the superfluidity decreases when the angular velocity increases.

2.5.4 Excited Energy versus vortex number for different system sizes

We will like to understand further the relationship of the excited energies of simulations with different number of quantized vortices and different system sizes. Fig.(2.12) we plot the excited energies (the energy at the end of the simulation subtracted initial energy) normalized by $0.6\epsilon_F N^{1/3}$ (to get rid of the particle dependence) with respect to the number of quantized vortices. Also for comparison we calculate the normalized energy of the system treated as a rigid body; its angular momentum corresponds to different number of quantized

vortices. We observe several interesting phenomena:

1. When the particle-dependent term is subtracted out of the excited energy, the energies of different system sizes fall on to the same curve in Fig.(2.12) with only slight discrepancies. This is consistent with the universal property of the unitary fermi gas, as the particle-independent physical properties should be the same for all unitary systems. The slight discrepancies are possibly caused by some variations in different simulations. Examples of this are the number of phonons generated during the stirring process and the positions of the quantized vortices.

2. The excited energy versus quantized vortex curve appears to be quadratic. We know the energy of a system with many vortices is the sum of energy to generate each vortex plus the interacting energy between each pair of vortices. As the first energy scales linearly while the second scales quadratically with respect to the vortex number, the dominant energy factor in our simulations seemed to be the mutual interaction between the quantized vortices.

3. The excited energy versus quantized vortex curve approximately follows the rigid body energy curve, while at large number of vortices it started to deviate from it. The similarity of the excited energy curve to the rigid body energy curve indicates that the classical rigid body model is a good approximation to the energy of the quantized vortex system with a few vortices. The deviation when the vortex number is large can be explained by the larger density deviations to the initial state and the larger number of phonons in a highly-stirred state.

Since the excited energy curve closely follows the rigid body energy curve, one expects that the collective kinetic energy $E_{\text{coll.kin.}}$, which is defined mathematically by:

$$\begin{aligned} E_{\text{coll.kin.}} &= \int d^3r \frac{\vec{j}^2}{2\rho(\vec{r})} \\ \vec{j}(\vec{r},t) &= \text{Im}[2i\sum_n v_n^*(\vec{r},t)\vec{\nabla}v_n(\vec{r},t)] \end{aligned} \tag{2.17}$$

and physically represents the macroscopic flow energy in the superfluid unitary system, is the dominant component of the excited energy. However, our calculations shows that such term is small compared to the excited energies and the rigid body kinetic energies.

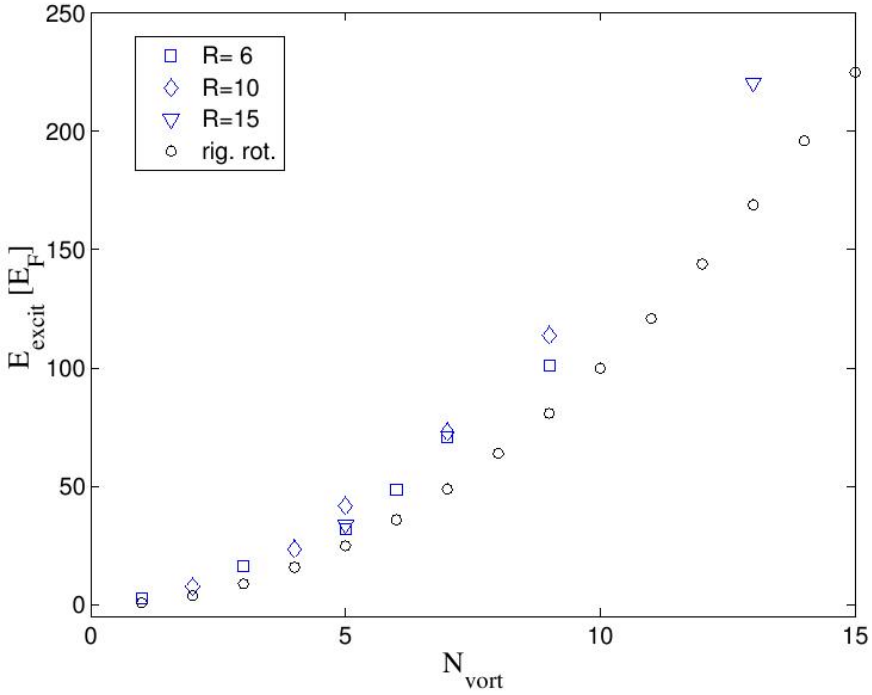

Figure 2.12: The normalized excitation energy versus number of quantized vortices of different simulation sizes and with stirring radius $R = 6$, 10, and 15. The circle dots are the normalized energy of the a rigid body system, with the rigid body approximated by the initial state of the system. The plot shows the universality of the unitary fermi gas, its quadratic relation between the excited energy and the quantized vortex number, and the similarity of the excitation curve to the rigid body curve.

Combined with the fact that we observe a quadratic excited energy curve, we conclude that despite the similarity of the excited energies curve to the rigid body curve, the energy is mostly represented in the density distortion caused by the interaction between quantized vortices.

2.5.5 Summary and Final Remarks

In this chapter we discuss the experiment [90] that demonstrates superfluidity in ultracold fermi gases and review the various classical superfluid dynamical theories. We also show how our SLDA formation can be used to describe the experiment and "bridged the gap"

by showing the dynamics during the vortex formation process. We observe strong compressibility of the unitary gas during the stirring process, which explains the controversy of having superfluidity when the stirring velocity is above the critical velocity. We also create simulations that demonstrate the transition from no vortices to several vortices, and to the lost of superfluid state. We examine the effect of geometry to vortex creation and destruction. Finally we discuss the relationship of excited states to the number of quantized vortices, and compare them to the energy of rigid body rotation.

The simulations discussed in this chapter are confined within two dimension; that is, we impose uniformity restriction in the z-direction. In the next chapter we will drop such restriction and simulate the unitary fermi gas dynamics in a full 3D dimension. We will see that many more exciting phenomena appeared.

Chapter 3

SUPERFLUID DYNAMICS OF THE UNITARY FERMI GAS IN THREE DIMENSION

This chapter presents the unitary fermi gas dynamics in zero temperature and in the full 3-dimensional space. Phenomena unseen in the 2-dimension simulations, for example the twisting (Kelvin waves) of vortices, the separation of one vortex of two-unit angular momentum into two vortices with single unit angular momentum, the creation of vortex rings, and the vortex segmentation and reconnection, are discussed. These results are published in [16].

3.1 Introduction

In previous chapter we investigate the dynamics of quantized vortex generation in $2D + 1$ dimension: we impose uniformity in the z direction and allow density variations in the x and y directions. Consequently the generated vortices are all "straight" without any bending and twisting. The quantized circulation is also only binary, being either counterclockwise or clockwise when seen from the z direction. As a result, in $2D+1$ dimension the motion of quantized vortices are relatively very limited: once they are generated they can only repel other vortices with the same circulation and form a vortex lattice, or annihilate with others with an opposite circulation.

When the restriction in the z-direction is dropped the degrees of freedom of quantized vortices largely increase, and as a result many interesting phenomena occurred. For example, a single quantized vortex can start bending and twisting, forming helical waves called "Kelvin Waves". It can also form solitary kink waves as the "Hasimoto Waves" [25] that propagate on the quantized vortex. In the case of extreme bending, a quantized vortex connects itself at the ends and forms a "vortex ring". The ring has a specific traveling velocity determined by the size and the radius of the vortex ring similar to the vortex ring in a bose condensate [61] or merely a classical smoke ring. An example of a classical smoke

ring is showed in Fig.(3.1).

Figure 3.1: Generation of a classical smoke ring[77].

For a system with many quantized vortices the bending and twisting of these vortices create a much interesting interaction than the simple repulsion and attraction seen in the 2D+1 simulations. For example, when two quantized vortices collide they can temporarily form an "X" shape structure and breakaway. The collided vortices can retain their original components with distorted bodies due to collision, or they can exchange new "parts" acquired from the colliding counterpart. The latter situation is similar to the case seen in liquid helium in Fig.(3.2). Such "vortex entanglement" allows the system to break large vortices into smaller vortices and create Kelvin waves, the waves onto each quatized vortex. These two mechanisms therefore transfer energies from large spacial structures (small wave-vectors) to small spacial structures (larger wave-vectors). With a large enough system with many tangled vortices randomly distorted and distributed in all directions, the system creates the "quantum turbulence" state described in the Introduction chapter.

To save computational time the ground state of the $3D$ simulations are the same as the $2D + 1$ simulations and have homogeneous density in the z direction. In the time-dependent code, however, the full $3D$ DVR representation is used for the operators, single-

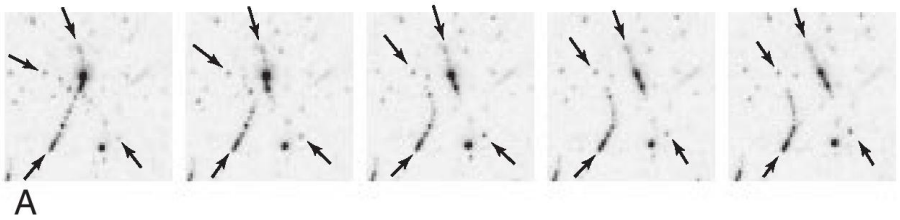

Figure 3.2: Reconnection of a pair of quantized vortices in superfluid liquid helium 4. The lines formed by black dots are vortices. One can clearly see that after reconnection the vortices swap their parts. [28]. Since the two resulting vortices have almost the same circulation they repel each other after reconnection.

particle wave-functions, potentials, and densities. For $3D$ simulations the checkpoint-restart functionality becomes critical, as many of our simulations required hours of computation that exceeds the maximal allowed computational time in the supercomputer facilities. To visualize the simulations we use VisIt and SILO file format (see Appendix C) to do graphic rendering and movie production.

3.2 Results

3.2.1 Generation of Twisted Vortices

To generate twisted vortices we use a "rod and a ball" stirrers, in which the rod generates the straight quantized vortices and the ball distortes the vortices. Fig.(3.3) shows the various stages of the 32 by 32 by 32 system during the stirring process. To visualize the vortices, only the pairing density within a value window is shown, and upper front quadrant is cut so that one can see through the trap. The upper left subplot shows that rather than pushing the quantized vortex away, the ball stirrer instead traps one quantized vortex and drags it along. Since the velocity of the ball is slightly faster than the generated vortex, the drag distorts the vortex and creates a twisted vortex, which is shown in the upper right subplot. The dragging effect can be explained by the reduction of energies when the ball and the vortex share part of their body, therefore reducing the compression to the surrounding unitary gas. When the rod stirrer is taken away from the system, due to its large size and rotating speed it generates a two-unit quantized vortex at the central position of the rod.

This vortex then later gradually splits into two partially connected single-unit quantized vortices, which is shown in the lower left subplot. Finally the repulsive forces between these vortices eventually separate each other and result into 5 twisted vortieces in the system, which is shown in the lower right subplot. One can clearly see the helical Kelvin wave formed at one of the vortex.

3.2.2 Generation and Interaction of Vortex Rings

In classical hydrodynamics a sphere projectile moving with sufficient high speed can create turbulence at the region opposite to the incoming fluid (Fig.(3.4)), and feel drag force to the projectile. In a similar fashion experimentalists use ions to move through the superfluid quantum liquid Helium above a certain critical speed, and generate quantized vortex rings [25] [9]. To simulate vortex rings in a unitary fermi gas system, we simulate a spherical projectile shooting through the z axes of a long, spherical trap (a 32 by 32 by 96 grid) with various velocities and ball sizes. Due to the finite volume and periodicity of our simulations we pass the ball several times through the trap. Fig.(3.5) shows the projectile shooting through the system with a speed $v_p = 0.3k_F$ and generated two vortex rings behind. Again to visualize the vortex ring only the pairing density in a certain value window is shown, and the two half-sides of the trap are cut to illustrate the process within. Besides the two vortex rings one can see the wiggles at the surface of the trap. These wiggles are generated at the onset of the shooting in front of the ball. They had traveled once through the trap and, due to periodicity, approach the projectile from back. When one estimates the velocity of the wiggles we find that it is close to the speed of sound in the unitary fermi gas. Thus those wiggles are actually phonons generated by the compression of the gas in front of the projectile.

As discussed in the introduction, we observe that the velocity of the vortex ring is larger when its radius is smaller. This creates an interesting dynamics that the vortex rings of different sizes can pass each other and change sizes. In Fig.(3.6), when a smaller vortex ring is generated behind a larger vortex ring it first moves closer to the larger ring. When they almost collide into each other the smaller ring shrinks and accelerates through the larger

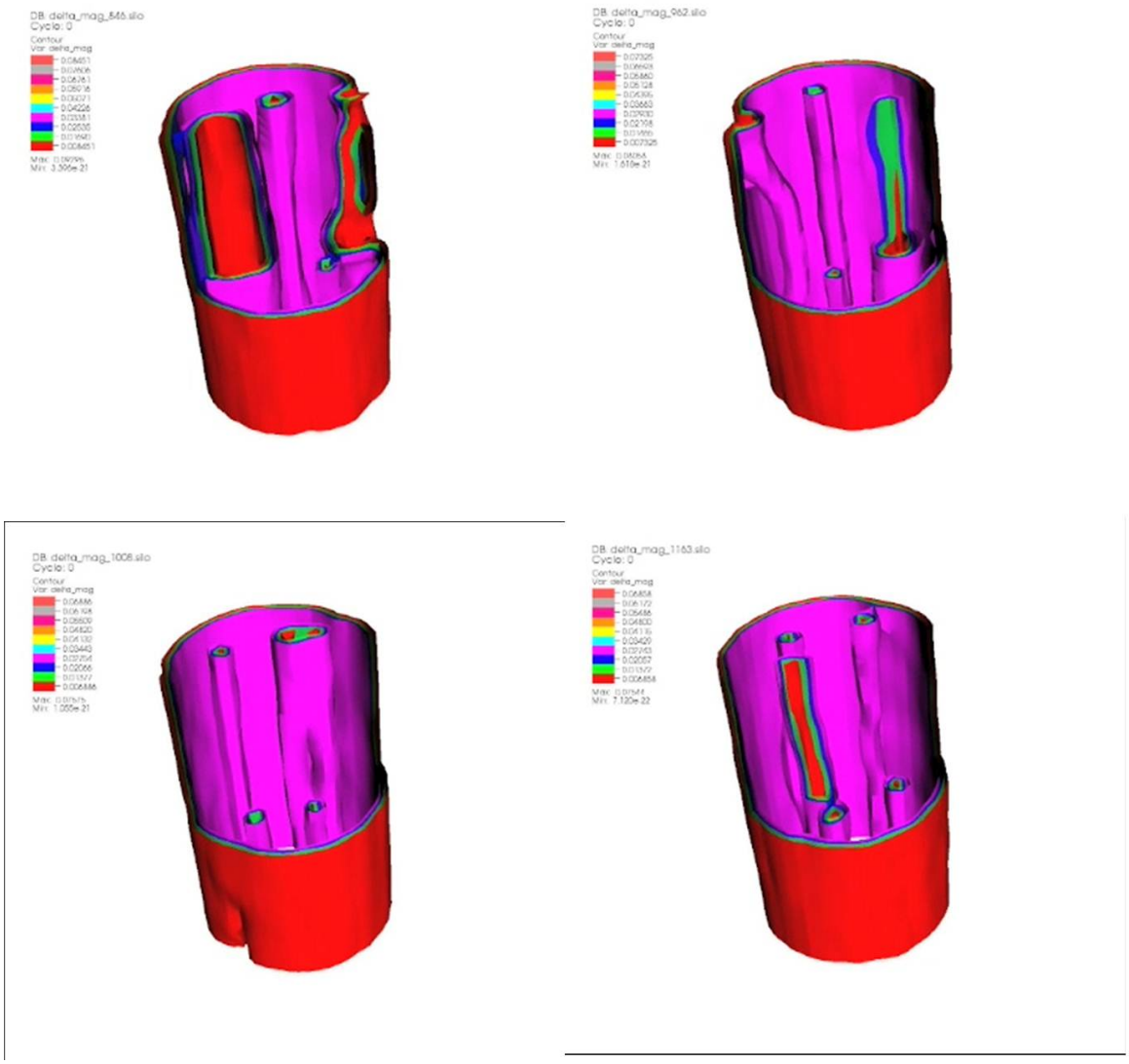

Figure 3.3: The various stages of a 32 by 32 by 32 unitary gas system during the stirring process. To visualize the vortices only the pairing density within a value window is shown, and the upper front quadrant is cut so that one can see through the trap. The upper left subplot shows one quantized vortex attaching to a ball. The upper right subplot shows the twisted vortex resulting from the ball attachment. The lower left subplot shows the two partially connected quantized vortices split from a two-unit vortex generated from the rotating rod. The lower right subplot shows the 5 twisted quantized vortices separating from each other due to the repulsive forces between them.

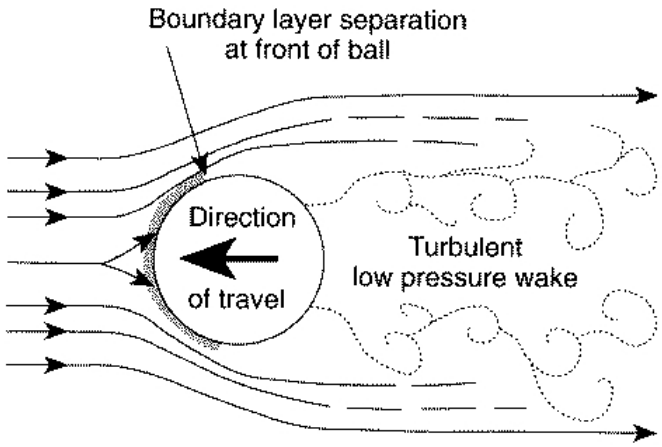

Figure 3.4: Air flow pattern through a spherical object such as a baseball. Turbulence was created at the back region of the ball, creating a drag force[79].

ring. The larger ring, on the other hand, expands and enables the smaller ring to pass through.

3.2.3 Vortex Crossing and Reconnection

To simulate vortex crossing, the generated quantum vortices must be bent and twisted to a sufficient degree to allow two vortices colliding into each other. Otherwise if they have almost the same circulation the repulsive forces will tend to straighten them and avoid each other. On the other hand, if they have almost the opposite circulation the vortices tend to annihilate with each other and result into normal fluid and phonon excitations. We find that using helical stirrers and off-centered projectiles can create the tangled vortex state we desire.

Fig.(3.7) demonstrates the different stirring stages of a stirring process using a helix rod (in a 32 by 32 by 96 grid). The helix rod is defined by a twisted rod with helix radius $R = 10$ and the center position $\vec{X}(x, y, z)$ as:

$$\vec{X}(x, y, z) = \left[R\cos\left(2\pi\frac{z}{L} + \theta(t)\right), R\sin\left(2\pi\frac{z}{L} + \theta(t)\right), z\right] \tag{3.1}$$

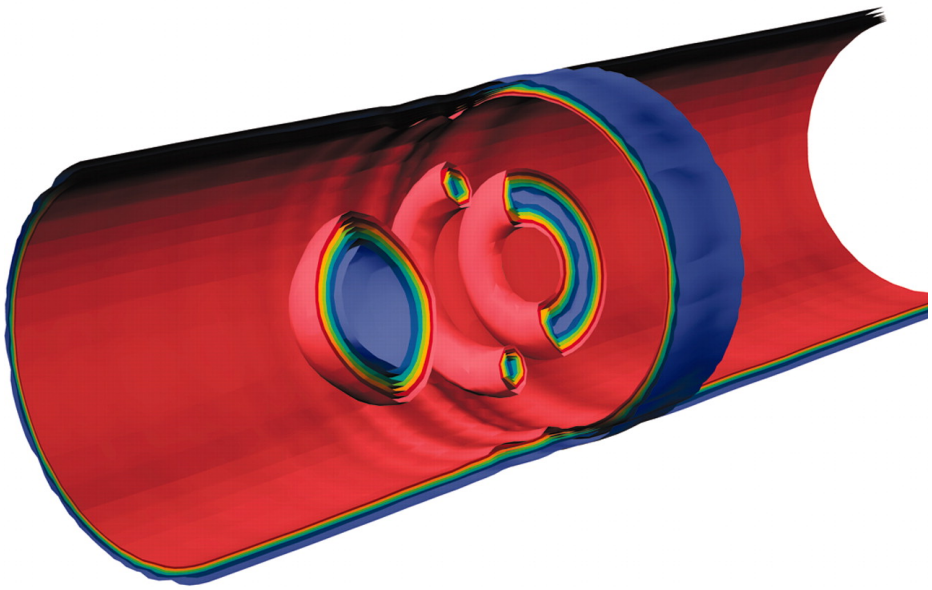

Figure 3.5: A spherical projectile shots through a 32 by 32 by 96 cylindrical trap and generates two vortex rings. Besides the trap sound, as seen as the wiggles at the surface of the trap, is also generated.

The helix stirrer is shown at the upper left subplot. This stirrer generates several highly twisted quantized vortices as shown in the upper right subplot. As the helix stirrer is taken away from the trap, the quantized vortices start to tangle and interact with each other. The original long twisted vortices create segments of smaller quantized "loops" attached onto the trap wall, which is shown in the lower left subplot. As more and more vortices interact and tangle, the vortices become shorter, segmented, and many "kinks", are generated on the vortex segments, which are shown in the lower right subplot.

When we look further into the stirring process shown in the lower left figure, we observe an interesting reconnection phenomenon. Fig.(3.8) shows the stages of how one of the vortex "loop" is formed and segregated. We observe that at first a small vortex segment approaches the longer quantized vortex and collides. They form a loop and evolve into a symmetric loop structure. Then surprisingly the left part of the loop, which is originally a part of the longer quantized vortex, separates and becomes a new quantum vortex segment. Such phenomenon is called reconnection. According to the quantum turbulence theory it

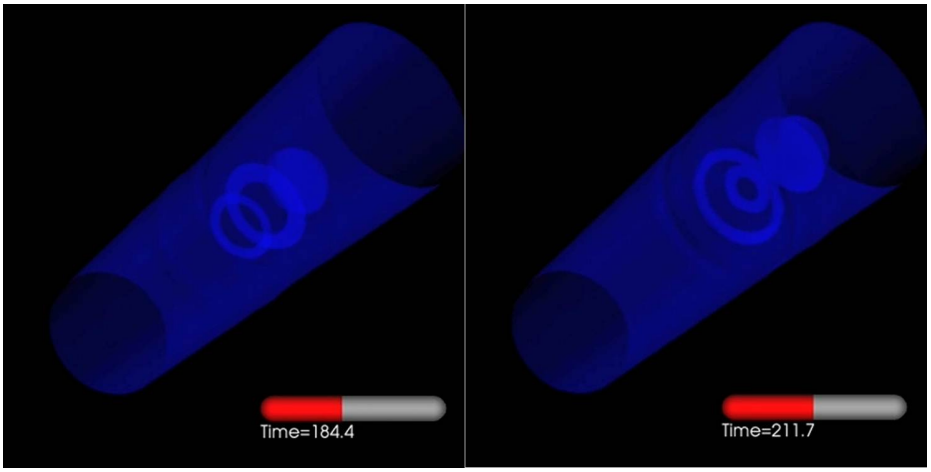

Figure 3.6: Vortex ring dynamics in a 32x32x96 simulation. Two vortex rings are created by the projectile with the former radius smaller than the latter. The smaller ring has a higher velocity and approaches the larger ring. When they almost collide the smaller ring shrinks and accelerates through the large ring, The large ring, on the other hand, expands in order to let the smaller ring pass.

plays the role of transferring energy from small wave-vectors to larger ones. This energy transfer mechanism is qualitatively demonstrated in our experiment by observing that after the reconnection, the longer vortex became more twisted and kinked. With the total energy fixed in the reconnection process it then means that part of the energies is transferred from orginal smooth vortex to these smaller structures.

To summarize, the helix simulation qualitatively demonstrates the onset of "quantum turbulence" in a superfluid unitary fermi gas system. From Fig.(3.7) we see how in a tangled system the different quantized vortices collide with each other, reconnect, produce kinks, and segment into smaller pieces. Although this simulation is too small to show the characteristic power spectrum of quantum turbulence discussed in the Introduction, we expected that in a larger system and with better ways of generating randomly distributed, tangled quantized vortices, we should be able to produce the characteristic quantum turbulence power spectrum.

Fig.(3.9) shows another example of vortex reconnection by shooting a spherical projectile similar to the vortex ring generation Fig.(3.5). However now the projectile trajectory is

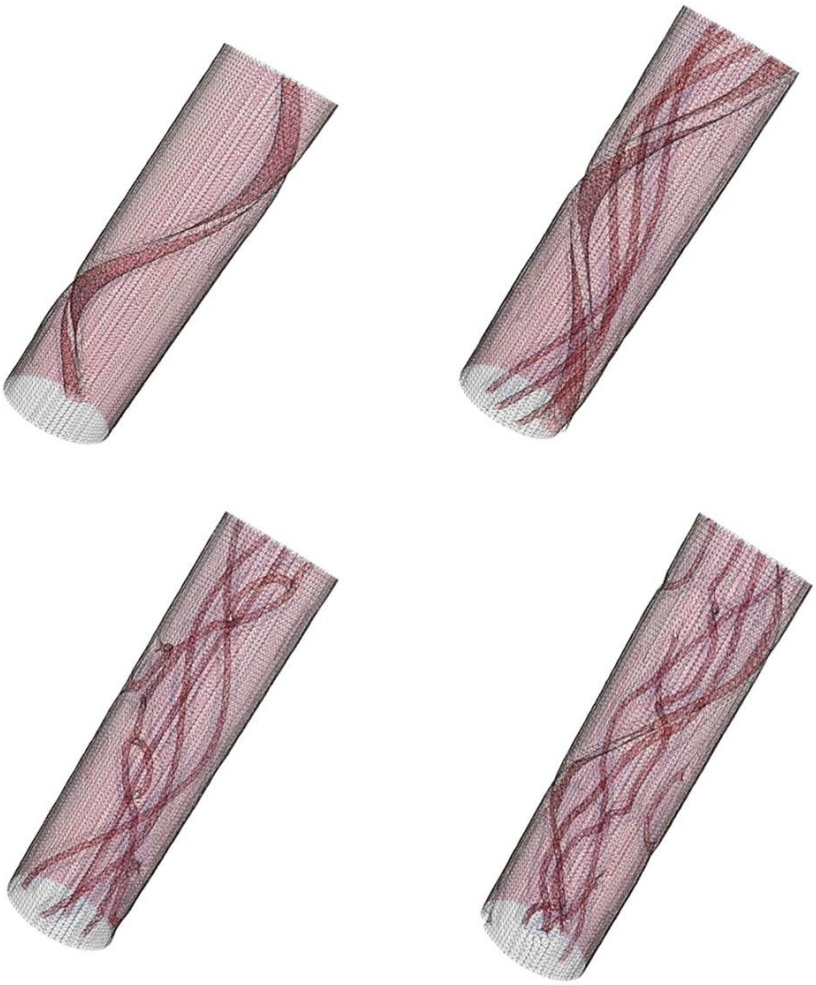

Figure 3.7: Different stages of a helix stirrer simulation in a 32x32x96 system. The upper left subplot shows the helix stirrer. The upper right shows the twisted quantized vortices generated by the helix rod. The lower left subplot shows that as the stirrer is removed, the vortices start to interact and create small "loops" attached onto the trap wall. The lower right subplot shows the end of the simulation, where the vortices are broken into smaller segments and have "kinks" all around their ends.

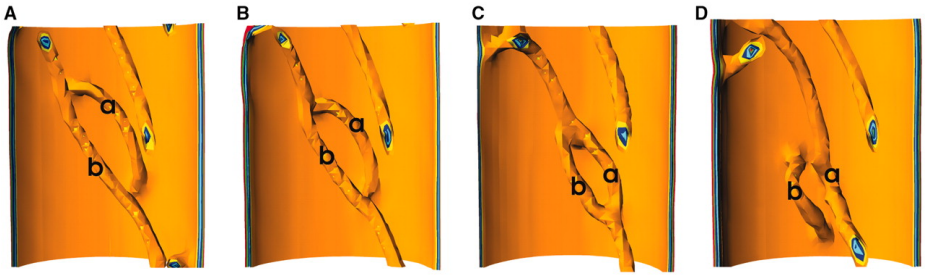

Figure 3.8: The loop forming process in the helix simulation. At first a small vortex segment approaches the long quantized vortex and collides. They form a loop and evolve into a more symmetric shape. Surprisingly the left part of the loop, which is originally part of the long quantized vortex, separates and becomes a quantum vortex segment.

slightly off-centered: the trajectory is now closer to one side of the trap. As shown in the upper left subplot, initially the projectile creates a parallel quantized vortex and a vortex ring. It then starts to generate another ring attached to the bottom of the trap. Then as shown in the upper right subplot, the ring pulls out a complicated structure that connects two rings and one quantized vortex in the middle. The structure then, as shown in the lower left subplot, becomes an X-shaped structure and separates into two quantized vortices . Finally, due to the interaction of the approaching parallel quantized vortex, the two vertical quantized vortices reconnect into an X-shape structure again and separate into two quantized vortices *parallel* to the long axes of the trap, which is shown in the lower right subplot. This vortex reconnection is similar to the superfluid liquid helium experiment shown in Fig.(3.2).

3.2.4 Summary

In this chapter we demonstrate the various dynamics of quantized vortices in the $3D$ environment. We first show the creation of twisted vortices with a "ball and rod" stirrer. Then we show the creation and interaction of vortex rings by shooting spherical projectiles through the long axes of the trap. Later we demonstrate the quantum vortex entanglement phenomena, which include vortex collision, reconnection, parts swapping, twists and kinks creation, and vortex/vortex rings segmentation. These simulations enable us to qualitatively

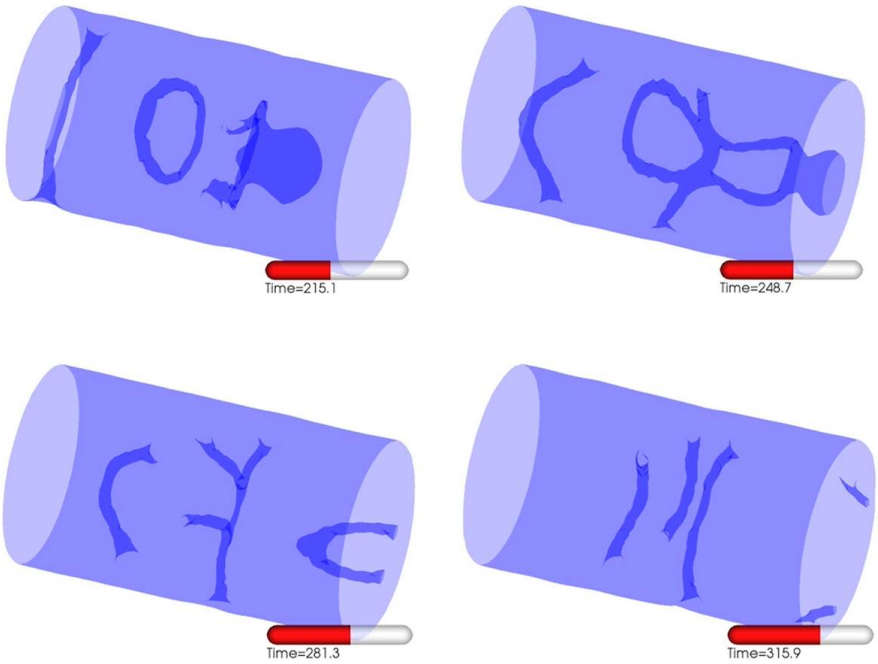

Figure 3.9: Vortex reconnection simulation by shooting a spherical projectile with an off-centered trajectory. In the upper left subplot initially the projectile creates a parallel quantized vortex and a vortex ring. It then starts to generate another ring attached to the bottom of the trap. In the upper right subplot the ring pulls out a complicated structure that connects two rings and one quantized vortex in the middle. In the lower left subplot the complex structure evolves into an X-shaped structure and later separates into two quantized vortices *vertical* to the long axes of the trap. Finally in the lower right subplot, due to the interaction of the approaching parallel quantized vortex, the two vertical quantized vortices reconnect into an X-shape structure and separate into two quantized vortices *parallel* to the long axes of the trap.

understand and visualize the dynamics resulting into quantum turbulence in a superfluid unitary fermi gas system.

In the next chapter, other nonlinear hydrodynamics and topological excitation of the unitary fermi gas are created through a dramatic dynamics: the collision of two large unitary fermi gas clouds.

Chapter 4

SHOCK WAVES AND DOMAIN WALLS IN UNITARY FERMI GAS

In this chapter we will discuss several non-linear superfluid hydrodynamics. These include shock waves, soliton trains, and domain walls. We are able to simulate the experiment of colliding two superfluid unitary fermi gas clouds [37] and observe the shock waves formation. Moreover we discover the generation of soliton trains and domain walls, and we provide a different explanation of the nature of the shock wave. The results are published in [7].

4.1 Introduction

For superfluid bose gas such as the Bose-Einstein condensate and superfluid liquid helium 4 in low temperature, a popular theoretical tool to describe their behavior is the Gross-Pitaevskii (GP) equation [30] [55]. Here we reprint the equation from Eqn.(2.4):

$$i\frac{\partial\Phi(\vec{r},t)}{\partial t} = \left(-\frac{1}{2}\nabla^2 + g|\Phi(\vec{r},t)|^2 - \mu\right)\Phi(\vec{r},t) \tag{4.1}$$

where Φ is the macroscopic superfluid wave function. Its square absolute value is the superfluid density, and its phase gradient is proportional to the superfluid velocity. We observe that Eqn.(4.1) is a non-linear wave function due to the quadratic density $g|\Phi(\vec{r},t)|^2$ term. As a result, the superfluid bose gas system displays some nonlinear hydrodynamics phenomena such as shock waves and solitons. These nonlinear phenomena indeed were observed in experiments [89] [68] [48] [21]. In a similar fashion, we expected the strongly interacting fermi gas superfluid, for example the superfluid unitary fermi gas, also demonstrates these nonlinear phenomena. In the Duke experiment [37] the authors demonstrate the creation of shock waves in a unitary fermi gas system. Initially they trap and cool a group of Li^6 atoms, and they separate them into two clouds through a narrow, repulsive

blue-detuned laser. To start the collision process they suddenly remove the laser to let the two clouds collide. Fig.(4.1) shows the absorption images of the cloud densities that are averaged over several experiments with approximately the same initial condition, and are taken in different collision time. The authors observe the collision generates a "box-like" structure in the center of the trap. It has a high, uniform density region in the middle and sharp density gradients at the two sides of the box.

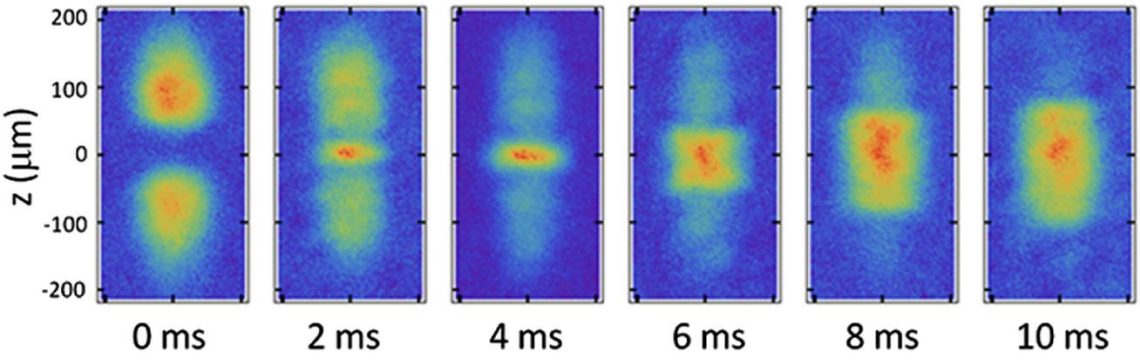

Figure 4.1: The Duke unitary fermi gas collision experiment [37]. Initially the two clouds of gas are separated by a repulsive blue-detuned laser and trapped within a red-detuned optical laser trap. At 0 ms the repulsive laser is suddenly turned off, and the two clouds approach each other by the harmonic trapping potential. At 2 to 4 ms the collision results into a "peak-like" shape with a high density peak in the middle of the trap. Later the shape evolved into a "box-like" shape with almost uniform density near the center of the trap, and a sharp boundary at the edges of the box.

To explain and simulate the observed shock waves the authors introduce a dissipative, viscous term $\nu\frac{\partial_z(n\partial_z v)}{n}$ into the normalized $1D$ hydrodynamic equations. The viscous term prevents the creation of so-called "gradient catastrophe" which described the infinite slope formation of the liquid medium if no dissipative or dispersive terms are included in the ordinary hydrodynamics equations.

4.2 Classical theory on nonlinear hydrodynamics

In this section a brief introduction on classical nonlinear hydrodynamics will be given. These theories will help us understand the nonlinear phenomena observed in a quantum system

such as the unitary fermi gas. The results are largely based on [88] and [48].

In one-dimensional linear wave theory such as an acoustic waves through a long pipe and or a light wave propagating in the vacuum, the wave satisfies the linear first-order equation:

$$\phi_t + c_0\phi_x = 0 \tag{4.2}$$

The solutions are simple sinuous waves traveling with a constant speed. Starting from Eqn.(4.2) one can add non-linearity into the system in order to describe nonlinear waves in nature. Some of the examples are water waves, flow of traffic, and nonlinear optics. One of the simplest ways is to make the speed c_0 dependent to the amplitude ϕ:

$$\phi_t + c_0(\phi)\phi_x = 0 \tag{4.3}$$

When $c(\phi) = \phi$ this gives the basic form of the superfluid velocity time derivative equation Eqn.(2.2). However, as shown in [88] a simple form of $c(\phi)$ with $\frac{\partial c(\phi}{\partial \phi}) > 0$ will make higher-amplitude waves travel faster and lower- amplitude waves slower. As a result a traveling wave with an initial finite slope wave front will develop an infinite slope at later time. Such phenomenon is the "gradient catastrophe" and is not physical. To remedy this problem a few additional small adjustment terms can be added into Eqn.(4.3). One example is to add a small dissipative term $\nu\phi_{xx}$ at the right hand side of Eqn.(4.3) and make it similar to a diffuse equation. With $c_0(\phi) = \phi$ this is called the Burger's equation:

$$\phi_t + \phi\phi_x = \nu\phi_{xx} \tag{4.4}$$

The other option to remedy the gradient catastrophe is to add a small dispersive term $\nu\phi_{xxx}$ at the right hand side. The resulting equation is called the Korteweg-deVries (KdV) equation:

$$\phi_t + \phi\phi_x = \nu\phi_{xxx} \tag{4.5}$$

Both of these equations are able to describe the shock wave nonlinear hydrodynamics. A shock wave is defined by a traveling structure in a liquid medium with abrupt difference of physical quantities (for example densities) at the two sides of the structure. In the vicinity of the abrupt change the structure depends on the detail formation of the equations as in Eqn.(4.4) and Eqn.(4.5). However to describe the general properties of the shock wave, one could use the flow continuity equation. If 1 and 2 represent the sub-indices of position x_1 and x_2 just in front and behind the shock front $s(t)$, with t as the time variable, and $Q(\phi)$ represents the flux, the continuity equation gives:

$$\begin{aligned} Q\left[\rho(s^-,t)\right] - Q\left[\rho(s^+,t)\right] &= \left(\phi(s^-,t) - \phi(s^+,t)\right)\frac{ds(t)}{dt} \\ \frac{ds(t)}{dt} \equiv U &= \frac{Q(\rho_2) - Q(\rho_1)}{\rho_2 - \rho_1} \end{aligned} \tag{4.6}$$

where U represents the shock front velocity. The characteristic velocity in the two sides of the shock is $c_i = c(\phi_i) = \frac{dQ}{d\phi}_i$, $i = 1, 2$, and the condition for the wave to maintain a shock structure is:

$$c_2 > U > c_1 \tag{4.7}$$

For a weak shock with $\rho_2 \approx \rho_1$ one can expand the right hand side of Eqn.(4.6) and get the shock propagation velocity:

$$U = \frac{1}{2}(c_1 + c_2) + O(\rho_2 - \rho_1)^2 \tag{4.8}$$

Although the shock wave speed has a universal expression described by Eqn.(4.6) and the Burger's and the KdV equation differ with very small coefficients ν, [48] shows that the two equations demonstrate distinct shock wave structures with very different speed. The solution of the Burger's equation with shock boundary condition $\phi_(- \infty) = 0$ and $\phi_(- \infty) = 1$ gives:

$$\phi(x,t) = \frac{1}{2} + \frac{1}{2}\tanh\left[-\frac{1}{4\nu}\left(\mathrm{x} - \frac{1}{2}\mathrm{t}\right)\right] \tag{4.9}$$

The solutions with various coefficients ν values are shown in Fig.(4.2). We observe that the shock velocity is 0.5. For the KdV equation, on the other hand, numerical solution gives a shock wave with rapid oscillation at front, which is shown in Fig.(4.3). The solution averaged over many oscillations gives a shock structure very similar to the Burger shock wave. However the velocity is 2/3 instead of 1/2, and this value 2/3 is also the velocity of the solitary wave solution for the KdV equation:

$$\phi(x,t) = 2\text{sech}\left[\frac{1}{\sqrt{(6\nu)}}\left(\text{x} - \frac{2}{3}\text{t}\right)\right] \tag{4.10}$$

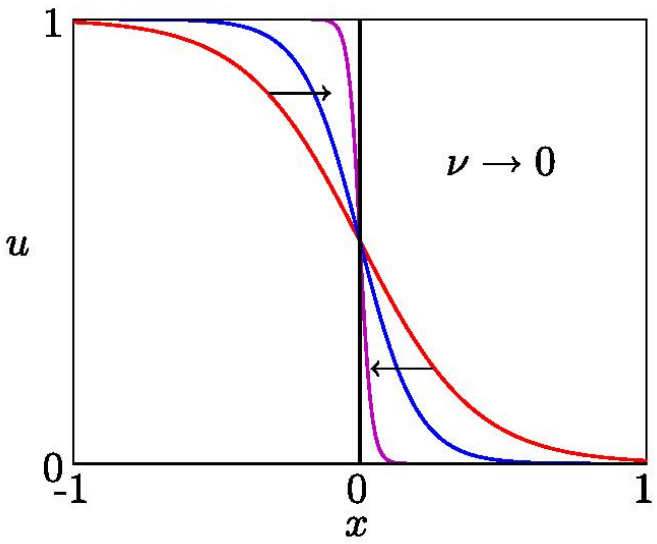

Figure 4.2: Solution of the Burger equation for various νs. The asymptotic solution approaches the discontinuous step function [48].

The velocity value and the oscillations can be explained by that for the dispersive KdV equation, a sharp gradient front produces a "train" of solitary waves at the shock front. This characteristic is also present in the Gross-Pitaevskii equation [48], which the equation Eqn.(4.1) can be rewritten to a hydrodynamic equation of density ρ and velocity u.

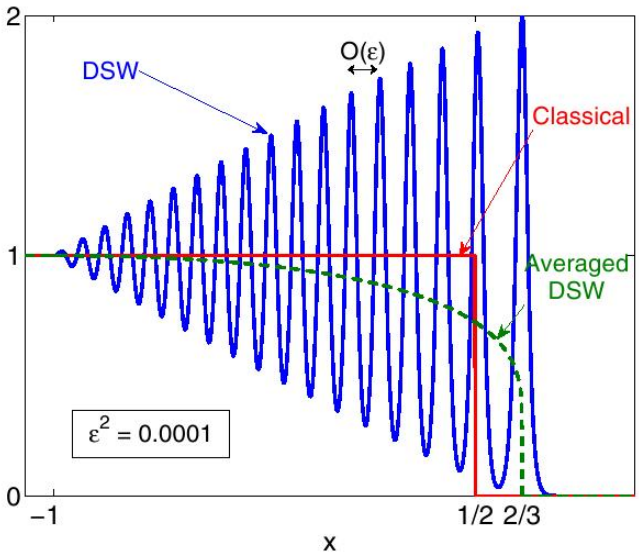

Figure 4.3: Numerical evolution of the KdV equation from a step function [48] with $\epsilon^2 = \nu$. Compared with the classical shock wave it has an oscillating structure. The solution averaged over oscillation has the shape similar to the classical shock but with a higher traveling speed $v = 2/3$.

4.3 Simulation setup

In our simulation we simulated the superfluid unitary gas collision in quasi-1D and 2D system and assume that the rest of dimensions be uniform. To mimic the experiment we use a harmonic trap to confine the unitary fermi gas, and "rounded" the trap near the boundary so that the periodic boundary condition is satisfied and no sharp edges were created. The reason to do so is that the sharp edges generate large errors when we perform Fourier transformation of the system. In the center we use a Gaussian-profile repulsive potential to separate the gas into two clouds. Due to the limitation of simulation hardware resources the width and the height of the repulsive potential do not exactly match the real experiment condition. We simulate different collision scenarios by changing the length-to-width trap aspect ratio, the initial phases of the two clouds, and the size of the grid.

4.4 Results

4.4.1 Generation of shock waves and soliton trains

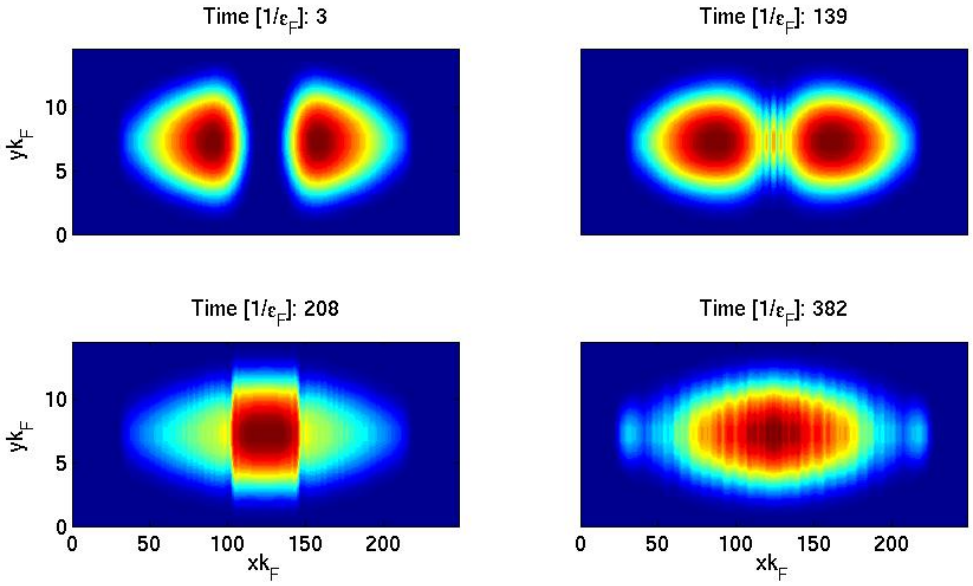

Figure 4.4: $2D+1$ Collision simulation of unitary fermi gas in a 256 by 16 2D+1 system. The plots does not show the actual aspect ratio. The two clouds are initially separated with the repulsive potential, and then they collide together and generate some interference at the collision center. The merging cloud then evolves into a box-like shape similar to the experiment in Fig.(4.1) [37]. Finally the system relaxes to a density distribution corresponding to the Thomas-Fermi distribution in a harmonic trap potential. During the collision process one can see some mysterious "strips" within the trap.

Fig.(4.4) shows the various time slice plots of a $2D+1$ collision simulation in a 256 by 16 grid (with uniform density in the 32 z axes). One can readily recognize the box-like structure within the simulation that indicates the formation of shock waves at the two edges of the box. The length-to-width ratio ($256/16 = 16$) of the simulation is similar to the experiment [37] ($437/27.7 = 15.8$). We notice that besides the shock waves, the simulation also generates some mysterious long "strips". These stripes can be seen at the beginning of the collision from the upper right subplot and the final relaxed state from the down right subplot, and they are not shown in the Duke experiment Fig.(4.1). To better visualize the

relation of shock waves and these trips to the collision time, we plot the density across the middle line of the trap with length equals to 256 versus time in Fig.(4.5).

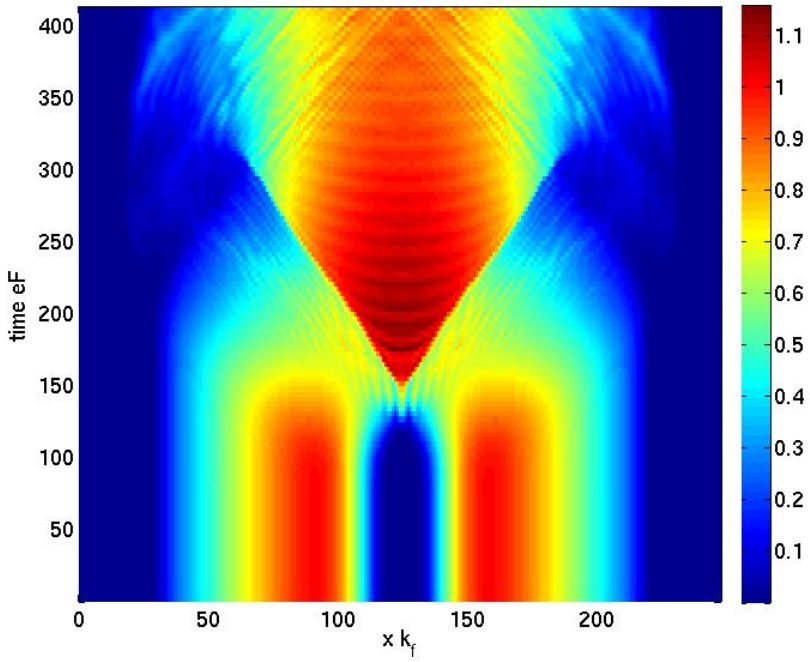

Figure 4.5: Density versus time plot of a line across the center of the trap in Fig.(4.4). The plot shows the shock front as the two density discontinuous lines forming an "V" shape. The ripples can be seen at the side of the shock front and at the upper part of the plot.

We observe that the shock wave is represented as a sharp discontinuity of two density lines forming a "V" shape. By calculating the slope of the two line and dividing by two for the $\frac{1}{2}$ appeared from $\epsilon_F = k_F^2/2$, we get the shock wave speed of about $0.2k_F$. Such value is smaller than the value estimated from the Duke experiment [37]. This discrepancy can be addressed to the different geometries of the simulation (full $3D$ versus $2D + 1$), the particle number estimation error in the experiment, the different repulsive potentials that resulted into different cloud profiles, the approximation model to describe the cloud expansion process, and the potential none-zero initial collision kinetic energy injected into the experiment.

Fig.(4.5) also display the mysterious density "strips" or ripples as seen in Fig.(4.4). The ripples seemed to be created from the initial interference of two colliding clouds. Once created they travel in front of the clouds into the edge of the trap, and are reflected and traveled back into the cloud. Furthermore, we observe that the velocity, or equivalent the trajectory slope , of these ripples do not change when they travel through the different density regions in the trap, or collide with each other. Compared these properties with the fact that solitary waves in the KdV equations had constant velocity and collided with each other elastically [88], we conclude that these ripples are solitary wave trains. Similar to the description in [48] that describes the soliton trains appearing either in front or at back of a dispersive shock wave (DSW) in a Bose superfluid system described by the GP equation, our solitary waves observation suggests that the shock wave in a superfluid unitary fermi gas system is a dispersive shock wave rather than a dissipative one claimed in the experiment [37]. The absence of ripples in the experiment can be explained by the image averaging process, which eliminates the small density variations while at the same time preserves the classical shock wave structure. The dissipative coefficient might be, as mentioned in [37], a pure phenomenological coefficient without any physical significance. Such argument is also supported by other studies [19], [71] that show the shear viscosity of the unitary fermi gas is small at the unitary regime.

4.4.2 Generation of domain walls and their dynamics

When we further simulate the collision with the trap length-to-width ratio twice as large as the experimental value (32), we observe a new excitation emerge from our simulation. Fig.(4.6) shows the density plot of a $2D + 1$ collision simulation in a 512 by 16 system. Compared with Fig.(4.4) we see that besides the typical box-shape shock wave front and trains of solitons some "domain walls" appear. Their structures are wider than soliton trains, and they are always presented as density depleted regions in the system. From the lower right subplot we also observe that these "domains", unlike the ripples which persist throughout the simulation, disappear later in the simulation as showed. To better understand these "domain walls" we again plot the position versus time plots for both the

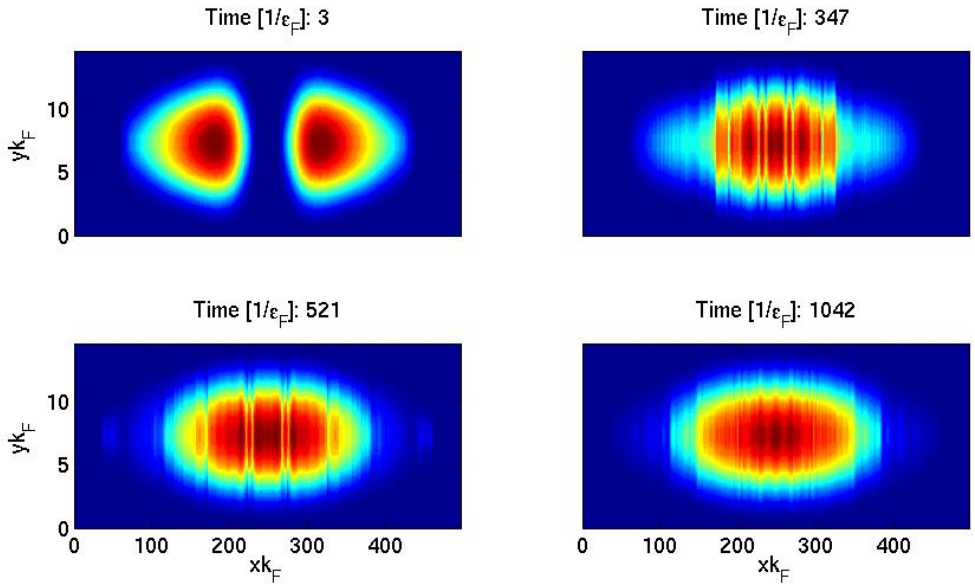

Figure 4.6: $2D + 1$ Collision simulation of unitary fermi gas in a 512 by 16 system (with uniform density along the 16-unit z axis). The plots does not show the actual aspect ratio. The length-to-width ratio is about twice as large as in the experiment [37]. We observe that besides the box-shape shock waves and the ripples seen in Fig.(4.4), we also observe some "domains". They are shown as density depletion strips with width much larger than the width of a single soliton in a soliton train.

density and the phase, which are shown in Fig.(4.7) and Fig.(4.8). We observe several features:

1. A closer look into Fig. (4.7) shows that the width of these domain walls are about $3k_F$. Compared with Fig(1.3) we observe that the width is similar to the width of a quantized vortex. This implies that the domain walls are also some quantized excitations in the system.

2. From Fig. (4.7) we observe that the density depletion at the center of the domain walls are the strongest at the turning points. They decrease when the domain walls had higher speed as measured by the slope of the trajectories.

3. From Fig. (4.8) we see a clear discontinuity of the phase across the domain wall. A closer look into Fig. (4.8) reveals that the phase change is about 180° degree at the turning point of the domain walls, where they were almost at rest. It decreases when the domain walls have a high speed as measured by the slope of the trajectories. Combined with feature

2. we conclude that there is a relationship between the phase change and the speed of a domain wall.

4. The domain walls seem to collide with each other elastically. This is shown by their continuous trajectories before and after collisions. However a closer look shows that some soliton trains emitted from the center of the domain wall collisions. Furthermore, at the top of Fig. (4.8) the domain walls are destroyed either by the other approaching domain walls or by the soliton trains.

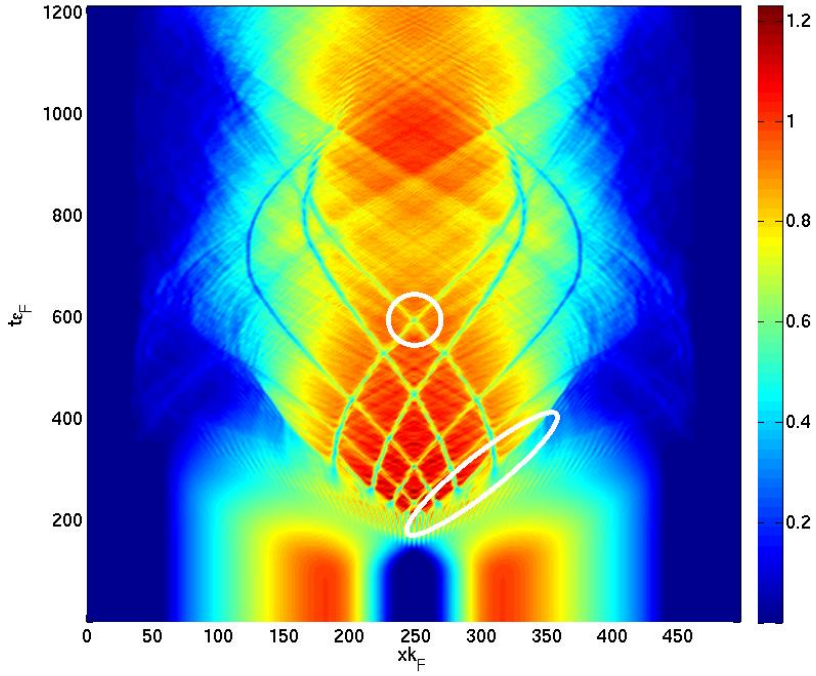

Figure 4.7: Position versus time plot of density of the $2D + 1$ collision simulation in a 512 by 16 by 16 lattice. The plot shows the trajectories of domain walls. One observe that the width of each domain wall is similar to the width of a quantized vortex. The density depletion is the strongest when the domain walls are stationary, and is the lowest when domain walls had the highest speed (the speed was measured by the slope of the trajectories). One also observes the generation of soliton trains during collisions between domain walls, or the collisions of domain walls with soliton trains.

These observation suggest that the domain walls are some sort of topological defects

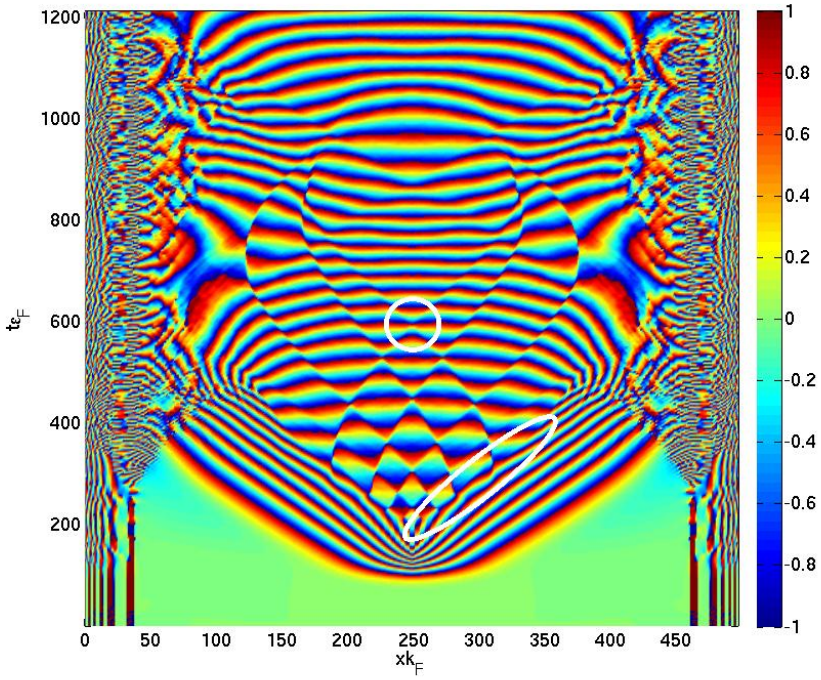

Figure 4.8: Position versus time plot of phase of the $2D+1$ collision simulation in a 512 by 16 lattice. The plot shows that unlike the soliton trains, which are observable in the density plot but not in the phase plot, the trajectories of domain walls are shown as discontinuous lines of the phase. One observes that the phase discontinuity is the strongest when the domain walls were stationary, and it has the value of about 180°. The discontinuity is the lowest when domain walls has the highest speed.

similar to quantized vortices. Indeed they are called "dark/grey solitons" in other publications, and the behaviors observed in Fig.(4.7) and Fig.(4.8) are also seen in [50], [58], and [59].

Fig.(4.9) shows the momentum of the unitary gas in x-direction. One sees that the domain walls emerge from the interference of the two colliding clouds shown as a "comb" like structure at the onset of the collision. Each "tooth" of this interfere does not itself generate one domain wall, but several of them together created one domain wall at later time. One also observes that the initial moving direction of these domain walls are opposite to the direction of the shock wave fronts. The underlying mechanisms of these two phenomena

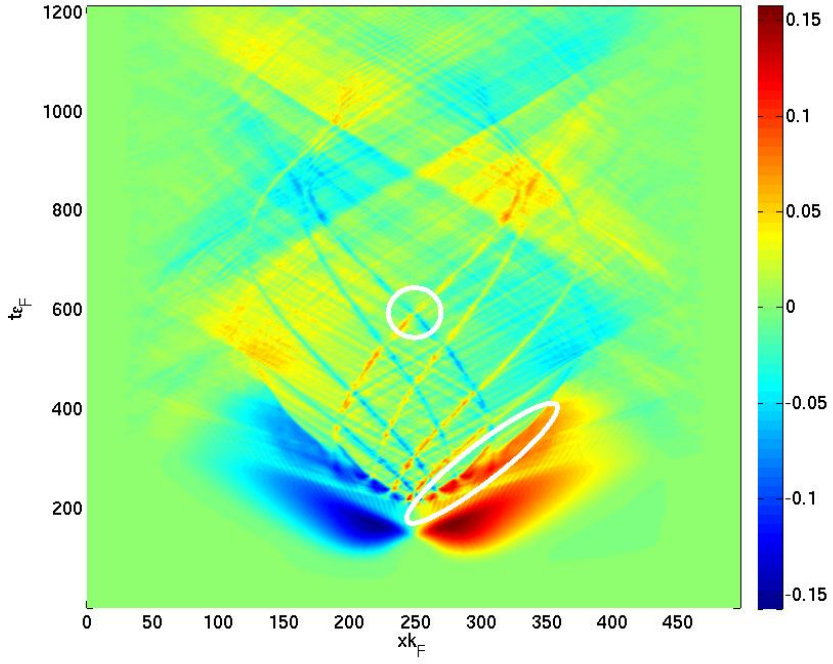

Figure 4.9: Position versus time plot of momentum in x-axis for the $2D + 1$ collision simulation in a 512 by 16 lattice. One sees that the domain walls emerge from a comb-like interference pattern during the initial state of collision, and initially they travel in opposite direction of the shock wave fronts.

can be for future investigation on superfluid unitary gas collision studies.

Finally, we investigate into more detail on the inelastic collisions of the domain walls. Fig.(4.10) shows various inelastic collisions of domain walls in $1D + 2$ dimension. The left-most subplot shows the collision of two domain walls; the middle subplot shows the collision of one domain wall to a small "bump" of repulsive potential in the middle of the trap; the right-most subplot shows the domain wall collision with a larger bump. Th domain walls in these simulation are initially prepared in a flat potential trap to converge to a stable solution. Then after a few unit of time a harmonic confining potential is gradually turned on to move the domain walls.

As seen in the simulations and also stated in [59], unlike the classical particles which decelerates under inelastic collision, the domain walls accelerates after inelastic collisions.

As a result, after several collisions the domain walls move to the edge of the trap and decay into soliton trains. As implied in Fig.(4.7), Fig.(4.10) explicitly demonstrates the inelastic collision process between the domain walls themselves, or between the domain walls and the bump potentials. It also explicitly shows the soliton trains emitted from both directions during a collision process. The collision of the domain wall to a repulsive bump potential in the middle and right-most subplots also showed that similar to a classical particle, domain walls can be scattered back by a sufficient large repulsive potential.

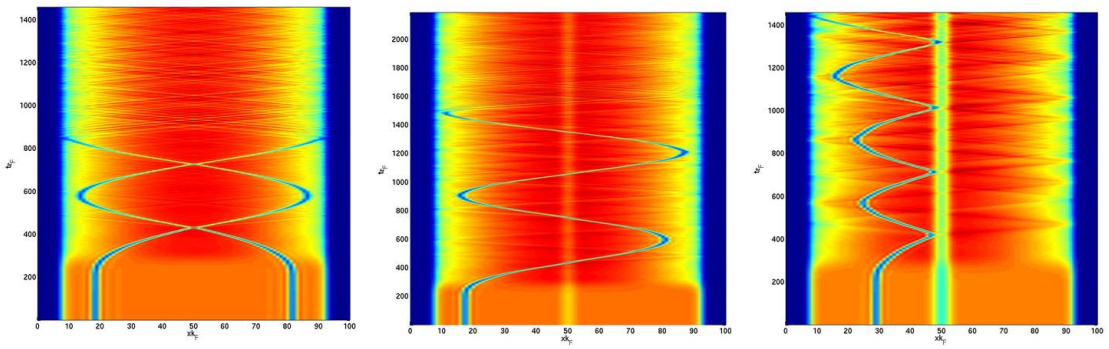

Figure 4.10: Various $1D + 2$ simulations of domain wall inelastic scattering processes. In each simulation the domain wall is initially located in a flat-bottom potential. After about 200 unit of time a harmonic potential is gradually turned on, and it forces the domain walls to collide. In the left-most subplot two domain walls collide with each other and emitted soliton trains in both side of directions. In the middle subplot the domain wall collides onto a small "bump" repulsive potential and emits soliton trains. In the right-most subplot the repulsive potential is so large that it scatters back the domain wall. In all three simulations the inelastic collision process accelerates the domain walls, and move them closer and closer to the edge of the trap. With sufficient acceleration the domain walls decay near the edge of the trap into several soliton trains.

Chapter 5

CONCLUSIONS AND FUTURE WORK

5.1 Conclusions

In this thesis we study the non-linear hydrodynamics and topological excitations of unitary fermi gases. The properties of these phenomena are explored in either full $3D$ dimension or with uniform density constraint in either 1 or 2 dimensions. They are also explored with various generating methods by stirring the systems with rods, shooting spherical bullets, or by colliding two unitary fermi clouds.

For $2D+1$ quantized vortex dynamics, we first show that our SLDA formation can accurately simulate from *ab-initio* the systems with no vortices, with some vortices, and systems in which the superfluidity is destroyed and there is again no vortex *from ab-initio*. This shows the superiority of our formation to other traditional methods for superfluid dynamics. Examples of this are the Landau's two-fluid model, the Gross-Pitaevskii (GP) equation, and the Bogoliubov-deGennes Equation. Our simulations supplement the experimental results by showing how the system is largely compressed during the stirring process and thus preserved superfluidity. We also verify the importance of the trap geometry and the alignment of the stirring center as observed in the MIT experiment. Lastly, by comparing vortex numbers to the normalized energy of different simulations, we reach the conclusion that the exciting energy is mostly due to the interactions between vortices. Such energies are represented as the strong density distortion created by these vortices.

For full $3D$ simulations we generate additional dynamics of quantized vortices. Examples of this are the Kelvin Waves on distorted vortices, the vortex rings and their dynamics of adjusting their sizes during collision, and finally the vortex separation and reconnection phenomena. The work on vortex segregation and reconnection give us insights on the mechanisms of quantum turbulence in a superfluid unitary fermi gase system. Furthermore, it suggests some potential ways to create quantum turbulence ab-initio from a uniform

system in unitary fermi gases.

Finally, our simulation on unitary fermi gas collision not only reproduces shock waves seen in the Duke experiment, but it also predicts the creation of domain walls in a system with sufficient large length-to-width ratio. Our simulation results suggest that the shock waves are dispersive shock waves rather than dissipative claimed in the experiment. We also verify the various properties of the domain walls, or so-called "dark solitons" in other theoretical simulations, with our more accurate SLDA formation.

5.2 Future Work

Much remains to be done in this field. One of the major questions to be addressed is what characteristics a quantum turbulent state has in a superfluid unitary fermi gas system. For example what is the kinetic power spectrum coefficients of a turbulent state in a unitary fermi gas as in Fig.(1.5), and what k value the transition from classical to quantum power spectrum appears on the figure. To get such quantum turbulent state a large enough system, along with sufficient quantized vortices closely packed with each other in a randomized fashion, is necessary. This requires sufficient computational power, enough CPU time for simulation, and most importantly an effective way to generate such a largely tangled vortex state as the initial condition. Initial exploration in a 32 by 32 by 32 lattice with complicated stirring potentials, for example a potential "net" or rods passing from different directions, generate complicated quantized system during the stirring process. However this complex structure quickly decays into several simple vortices before the stirring potential is turned off. Perhaps a way of initially imprinting phases into initial conditions, as it is used in the initial creation of domain walls in Fig.(4.10), can be more effective. However using such imprinting method might require a new, innovative iterative method in order to converge to a stable solution with reasonable steps, as the author observes that the number of steps to convergence largely increases for the domain wall, and sometimes the system becomes oscillatory and does not converged.

For the unitary gas collision experiment, a full $3D$ collision might reveal some other interesting features of domain walls. Examples of this are the "Snake Instability" [89] of the domain wall decaying into quantized vortices, and the interaction between these vortices

and domain walls [39]. As shown in Fig.(5.1), the collision of a large enough cloud can generate so many domain walls and, when they decay, possibly create a turbulent state.

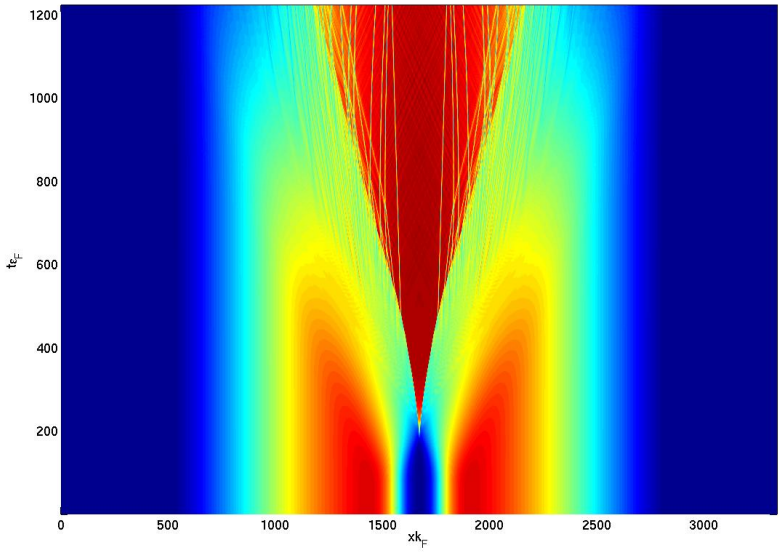

Figure 5.1: $2D+1$ Collision simulation in 4000 by 32 by 32 grid. Massive amount of domain walls are generated during the collision process.

Third, the SLDA formation in this thesis describes unitary fermi gases system with fully paired and equally amount of spin up and spin down particles in zero temperature. It is possible to extend our formation into so-called "Asymmetric" Superfluid Local Density Approximation (ASLDA) [14], and study the dynamics of asymmetric systems in finite temperature [49]. One of the challenges to simulate an asymmetric system is to deal with the non-adiabatic collision process when spin-up fermions collide with spin-down fermions [65] [53]. The inclusion of the additional spin freedom can result into more types of topological defects and the dynamics between them.

Finally, by rewriting the evolution operator of an on-site interacting fermion system by the Trotter decomposition and discrete Hubbard-Stratonovich transformation [33] [11], one rewrites the interaction potential term as:

$$\begin{aligned} \exp\left(-ig\Delta t n_{k\uparrow} n_{k\downarrow}\right) &= 1 + A^2 n_{k\uparrow} n_{k\downarrow} \\ &= \frac{1}{2} \sum_{\sigma_k = \pm 1} \left(1 + A n_{k\uparrow}\right)\left(1 + A n_{k\uparrow}\right) \end{aligned} \tag{5.1}$$

which $A = \sqrt{(exp(-ig\Delta t - 1)}$. The plus and minus term can therefore be generated stochastically by random number of $+1$ and -1 for vast number of ensembles. The approximated final results are calculated as the averaged physical values over all these ensembles. The author have performed some preliminary calculations of the wave function norm and the energies of a small system. We find that while the norm remains close to 1 after a few hundred simulation, the kinetic energy generates large errors. Future work to understand better the error sources of such formation and to reduce errors will be critical for applying such formation for time-dependent strongly interacting fermion gas calculation.

BIBLIOGRAPHY

[1] Gray solitons in a strongly interacting superfluid fermi gas. *New J. Phys*, 13:035010, 2011.

[2] A. A. Abrikosov, L. P. Gorkov, and I. E. Dzyaloshinski. *Methods of Quantum Field Theory in Statistical Physics*. Dover, Mineola, NY, 1975.

[3] Yean an Liao, Ann Sophie C. Ritter, Tobias Paprotta, Wenhui Li, Guthrie B. Partridge, Randall G. Hulet, Stefan K. Baur, and Erich J. Mueller. Spin-imbalance in a one-dimensional fermi gas. *Nature*, 467:567–571, 2010.

[4] M. H. Anderson, J. R. Ensher, M. R. Matthews, C. E. Wieman, and E. A. Cornell. Observation of bose-einstein condensation in a dilute atomic vapor. *Science*, 269:198–201, 1995.

[5] Mauro Antezza, Franco Dalfovo, Lev P. Pitaevskii, and Sandro Stringari. Dark solitons in a superfluid fermi gas. *Phys. Rev. A.*, 76:043610, 2007.

[6] Joaquin E. Drut Aurel Bulgac and Piotr Magierski. Quantum monte carlo simulations of the bcs-bec crossover at finite temperature. *Phys. Rev. A.*, 78:023625, 2008.

[7] Yuan-Lung Luo Aurel Bulgac and Kenneth J. Roche. Quantum shock waves and domain walls in the real-time dynamics of a superfluid unitary fermi gas. *Phys. Rev. Lett.*, 108:150401, 2012.

[8] J. Bardeen, L. N. Cooper, and J. R. Schrieffer. Theory of superconductivity. *Phys. Rev.*, 108:1175–1204, 1957.

[9] R. M. Bowley. Vortices in 2-d and 3-d superfluids. *J. Low. Temp.*, 87:137, 1992.

[10] G. Bruun, Y. Castin, R. Dum, and K. Burnett. Bcs theory for trapped ultracold fermions. *Eur. Phys. J. D*, 7:433–439, 1999.

[11] Aurel Bulgac. Private notes.

[12] Aurel Bulgac. Local-density-functional theory for superfluid fermionic systems: The unitary gas. *Phys. Rev. A.*, 76:040502, 2007.

[13] Aurel Bulgac. The unitary fermi gas: From quantum monte carlo to density functional theory, to real time dynamics. Presented at the INT program Fermions from Cold Atoms to Neutron Stars: Benchmarking the Many-Body Problem, 2011.

[14] Aurel Bulgac and Michael Forbes. Unitary fermi supersolid: The larkin-ovchinnikov phase. *Phys. Rev. Lett.*, 101:215301, 2008.

[15] Aurel Bulgac, Michael McNeil Forbes, and Piotr Magierski. The unitary fermi gas: From monte carlo to density functionals. *ArXiv*, 1008.3933, 2010.

[16] Aurel Bulgac, Yuan-Lung Luo, Piotr Magierski, Kenneth J. Roche, and Yongle Yu. Real-time dynamics of quantized vortices in a unitary fermi superfluid. *Science*, 332:1288–1291, 2011.

[17] Aurel Bulgac and Yongle Yu. Renormalization of the hartree-fock-bogoliubov equations in the case of a zero range pairing interaction. *Phys. Rev. Lett.*, 88:042504, 2002.

[18] Aurel Bulgac and Yongle Yu. Vortex state in a strongly coupled dilute atomic fermionic superfluid. *Phys. Rev. Lett.*, 91:190404, 2003.

[19] H. Wu C. Cao, E. Elliott and J. E. Thomas. Searching for perfect fluids: quantum viscosity in a universal fermi gas. *New. J. Phys.*, 13:1, 2011.

[20] J. Carlson and Sanjay Reddy. Asymmetric two-component fermion systems in strong coupling. *Phys. Rev. Lett.*, 95:060401, 2005.

[21] J. J. Chang and P. Engels. M. A. Hoefer. Formation of dispersive shock waves by merging and splitting bose-einstein condensates. *Phys. Rev. Lett.*, 101:170404, 2008.

[22] Leon N. Cooper. Bound electron pairs in a degenerate fermi gas. *Phys. Rev.*, 104:1189–1190, 1956.

[23] Franco Dalfovo and Sandro Stringari Stefano Giorgini, Lev P. Pitaevskii. Theory of bose-einstein condensation in trapped gases. *Rev. Mod. Phys.*, 71:463, 1999.

[24] B. DeMarco and D. S. Jin. Onset of fermi degeneracy in a trapped atomic gas. *Science*, 285:1703–1706, 1999.

[25] Russell J. Donnelly. *Quantized vortices in Helium II.* Cambridge University Press, NY, 1991.

[26] H. Feshbach. A unified theory of nuclear reactions. ii. *Ann. Phys.*, 19:287, 1962.

[27] Alexander L. Fetter and John Dirk Walecka. *Quantum Theory of Many-Particle Systems*. Dover, Mineola, NY, 2003.

[28] K. R. Sreenivasan G. P. Bewley, M. S. Paoletti and D. P. Lathrop. Characterization of reconnecting vortices in superfluid helium. *PNAS*, 105:13707, 2008.

[29] P. G. Gennes. *Superconductivity of Metals and Alloys*. Westview Press, Boulder CO, 1999.

[30] E. P. Gross. Structure of a quantized vortex in boson systems. *Nuovo Cim.*, 20:454–477, 1961.

[31] R. W. Hamming. *Numerical Methods for Scientists and Engineers*. McGraw-Hill, 1973.

[32] Shungo Ishino Hiromitsu Takeuchi and Makoto Tsubota. Binary quantum turbulence arising from countersuperflow instability in two-component bose-einstein condensates. *Phys. Rev. Lett.*, 105:205301, 2010.

[33] J. E. Hirsch. Discrete hubbard-stratonovich transformation for fermion lattice models. *Phys. Rev. B.*, 28:4059, 1983.

[34] Tin-Lun Ho. Universal thermodynamics of degenerate quantum gases in the unitarity limit. *Phys. Rev. Lett.*, 92:090402, 2004.

[35] P. Hohenberg and W. Kohn. Inhomogeneous electron gas. *Phys. Rev.*, 136:B864, 1964.

[36] D. D. Johnson. Modified broyden's method for accelerating convergence in self-consistent calculations. *Phys. Rev. B*, 38:12807–12813, 1988.

[37] J. A. Joseph, J. E. Thomas. M. Kulkarni, and A. G. Abanov. Observation of shock waves in a strongly interacting fermi gas. *Phys. Rev. Lett.*, 106:150401, 2011.

[38] R. J. Ballagh K. J. Challis and C. W. Gardiner. Bragg scattering of cooper pairs in an ultracold fermi gas. *Phys. Rev. Lett.*, 98:093002, 2007.

[39] Makoto Tsubota Kazuya Fujimoto. Synergy dynamics of vortices and solitons in atomic bose-einstein condensate excited by an oscillating potential. *Phys. Rev. A.*, 82:043611, 2010.

[40] Wolfgang Ketterle and Martin W. Zwierlein. Making, probing and understanding ultracold fermi gases. *ArXiv*, 0801.2500, 2008.

[41] T. Kinoshita, T. R. Wenger, and D. S. Weiss. A quantum newton's cradle. *Nature*, 440:900–903, 2006.

[42] Charles Kittel. *Introduction to Solid State Physics*. John Wiley & Sons, Hoboken, NJ, 2005.

[43] W. Kohn and L. J. Sham. Self-consistent equations including exchange and correlation effects. *Phys. Rev.*, 140:A1133, 1965.

[44] Manas Kulkarni and Alexander G. Abanov. Hydrodynamics of cold atomic gases in the limit of weak nonlinearity, dispersion, and dissipation. *Phys. Rev. A.*, 86:033614, 2012.

[45] L. D. Landau and E. M. Lifshitz. *Fluid Mechanics*. Pergamon Press, Oxford, 1987.

[46] L. Laudau. The theory of superfluidity of helium ii. *J. Phys. USSR*, 5:71, 1941.

[47] J. C. Light and T.Carrington. Discrete-variable representations and their utilization. *Adv. Chem. Phys.*, 114:263, 2000.

[48] I. Coddington E. A. Cornell P. Engels M. A. Hoefer, M. J. Ablowitz and V. Schweikhard. Dispersive and classical shock waves in bose-einstein condensates and gas dynamics. *Phys. Rev. A.*, 74:023623, 2006.

[49] Christian H. Schunck Martin W. Zwierlein, Andre Schirotzek and Wolfgang Ketterle. Fermionic superfluidity with imbalanced spin populations. *Science*, 311:492, 2005.

[50] Lev P. Pitaevskii Mauro Antezza, Franco Dalfovo and Sandro Stringari. Dark solitons in a superfluid fermi gas. *Phys. Rev. A.*, 76:043610, 2007.

[51] N. D. Mermin. The topological theory of defects in ordered media. *Rev. Mod. Phys.*, 51:591–648, 1979.

[52] Marshall N. Rosenbluth Augusta H. Teller Nicholas Metropolis, Arianna W. Rosenbluth and Edward Teller.

[53] F. Chevy O. Goulko and C. Lobo. Collision of two spin-polarized fermionic clouds. *Phys. Rev. A.*, 84:051605, 2011.

[54] L. N. Oliveira, E. K. U. Gross, and W. Kohn. Density-functional theory for superconductors. *Phys. Rev. Lett.*, 60:2430, 1984.

[55] L. P. Pitaevskii. Vortex lines in an imperfect bose gas. *Sov. Phys. JETP*, 13:451, 1961.

[56] L. P. Pitaevskii. Vortex lines in an imperfect bose gas. *ZEPT*, 40:646, 1961.

[57] M. Yu. Kagan R. Combescot and S. Stringari. Collective mode of homogeneous superfluid fermi gases in the bec-bcs crossover. *Phys. Rev. A*, 74:042717, 2006.

[58] L. P. Pitaevskii R. G. Scott, F. Dalfovo and S. Stringar. Dynamics of dark solitons in a trapped superfluid fermi gas. *Phys. Rev. Lett.*, 106:185301, 2011.

[59] L. P. Pitaevskii S. Stringar O Fialko R Liao R. G. Scott, F. Dalfovo and J Brand. The decay and collisions of dark solitons in superfluid fermi gases. *New. J. Phys.*, 14:023044, 2012.

[60] Peter Ring and Peter Schuck. *The Nuclear Many-Body Problem*. Springer-Verlag, NY, 1980.

[61] P. H. Roberts and J. Grant. Motions in a bose condensate. i. the structure of the large circular vortex. *J. Phys. A.*, 4:55, 1971.

[62] Erich Runge and E. K. U. Gross. Density-functional theory for time-dependent systems. *Phys. Rev. Lett.*, 52:997, 1984.

[63] J. J. Sakurai. *Modern Quantum Mechanics*. Addison-Wesley, Reading, MA, 1994.

[64] R. G. Scott, F. Dalfovo, L. P. Pitaevskii, and S. Stringari. Dynamics of dark solitons in a trapped superfluid fermi gas. *Phys. Rev. Lett.*, 106:185301, 2011.

[65] Ariel Sommer, Mark Ku, Giacomo Roati, and Martin W. Zwierlein. Universal spin transport in a strongly interacting fermi gas. *Nature*, 472:201–204, 2011.

[66] Sandro Stringari Stefano Giorgini, Lev P. Pitaevskii. Theory of ultracold atomic fermi gases. *Rev. Mod. Phys.*, 80:1215, 2008.

[67] Kevin E. Strecker, Guthrie B. Partridge, Andrew G. Truscott, and Randall G. Hulet. Formation and propagation of matter-wave soliton trains. *Nature*, 417:150–153, 2002.

[68] I. Coddington V. Schweikhard E. A. Cornell T. P. Simula, P. Engels and R. J. Ballagh. Observations on sound propagation in rapidly rotating bose-einstein condensates. *Phys. Rev. Lett.*, 94:080404, 2005.

[69] Mark J.H. Ku Lawrence W. Cheuk Wenjie Ji Waseem S. Bakr Martin W. Zwierlein Tarik Yefsah, Ariel T. Sommer.

[70] D. J. Thouless, Ping Ao, and Qian Niu. Transverse force on a quantized vortex in a superfluid. *Phys. Rev. Lett.*, 76:3758–3761, 1996.

[71] Rudolf Haussmann Tilman Enss and Wilhelm Zwerger. Viscosity and scale invariance in the unitary fermi gas. *Ann. Phys.*, 326:770, 2011.

[72] F. Tisseur and J. Dongarra.

[73] L. Tisza. Transport phenomena in helium ii. *Nature*, 141:913, 1938.

[74] A. Trenkwalder, C. Kohstall, M. Zaccanti, D. Naik, A. I. Sidorov, F. Schreck, and R. Grimm. Hydrodynamic expansion of a strongly interacting fermi-fermi mixture. *Phys. Rev. Lett.*, 106:115304, 2011.

[75] Makoto Tsubota and Kenichi Kasamatsu. Quantized vortices and quantum turbulence. *arXiv:1202.1863*.

[76] Makoto Tsubota, Kenichi Kasamatsu, and Michikazu Kobayashi. Quantized vortices in superfluid helium and atomic bose-einstein condensates. *ArXiv*, 1004.5458, 2010.

[77] `http://en.wikipedia.org/wiki/Vortex_ring_toy`.

[78] `http://escience.washington.edu/content/hyak-0`.

[79] `http://oregonstate.edu/instruct/exss323/Fluid_Motion/form_drag2.htm`.

[80] `https://wci.llnl.gov/codes/silo/release_notes.html`.

[81] `https://wci.llnl.gov/codes/visit/`.

[82] `https://www.olcf.ornl.gov/computing-resources/titan-cray-xk7/`.

[83] `http://wiki.lustre.org/index.php/Main_Page`.

[84] `http://www.fftw.org/`.

[85] `http://www.nersc.gov/systems/`.

[86] William F. Vinen and Russell J. Donnelly. Quantum turbulence. *Physics Today*, 60:43, 2007.

[87] S. A. Teukolsky W. H. Press, B. P. Flannery and W. T. Vetterling. *Numerical Recipes in C*. Cambridge University Press, 1988.

[88] G. B. Whitham. *Linear and Nonlinear Waves*. John Wiley and Sons, 1974.

[89] C. Slowe Z. Dutton, M. Budde and L. V. Hau. Observation of quantum shock waves created with ultra- compressed slow light pulses in a bose-einstein condensate. *Science*, 293:663, 2001.

[90] M.W. Zwierlein, J. R. Abo-Shaeer, A. Schirotzek, C. H. Schunk, and W. Ketterle. Vortices and superfluidity in a strongly interacting fermi gas. *Nature*, 435:1047–1051, 2005.

Appendix A

THE FESHBACH RESONANCE

A.1 Introduction

Feshbach resonance is a term that describes resonant scattering: when the scattering length a diverges between particles in a systems. Examples of this are nuclear systems with neutrons or trapped fermi gases. The resonance occurs between two fermion particles when the following situations are satisfied:

- There is a weak component in the interaction potential U_{cp} that couples two channels with different quantum number (ex: spin).

- Neglecting U_{cp}, there is a localized bound state in one channel with energy E_m being very close to zero. As a result the energy is very close to the continuous scattering state $E_s > 0$ in another channel

Because the energy values of the bare scattering states and the bound state are so close, the true scattering state (the state that diagonalizes the Hamiltonian) behaves like a free particle when the two particles are far apart, while it behaves like a bound state when the two particles get close to each other. The strong confinement of particles when they are close means that the particles are strongly scattered by each other. Therefore they have a diverging scattering length. The strong scattering length also means that the particles experience strong interaction when they are close together.

For the trapped fermi gases the two-particle bare scattering state and bare molecule state are characterized by the total electronic spin. With the restriction of Pauli principle the scattering state is a triplet and the molecule state is a singlet. The potential that couples the two state is the hyperfine potential:

$$\begin{aligned} U_{hf} &= a_{hf}\,(s_1 \cdot i_1 + s_2 \cdot i_2) \\ &= \frac{a_h f}{2}\,[S \cdot (i_1 + i_2) + (s_1 - s_2)(i_1 - i_2)] \end{aligned} \tag{A.1}$$

which can be diagonalized by the total spin (nuclear + electronic spin). One observes that the second part of U_{hf} couples the singlet state to the triplet state.

Because a singlet and a triplet state have different electronic structures, they have different magnetic moments. Thus by tuning the external magnetic field one can change the energy difference $\Delta E = E_s - E_m$ and change the degree of resonance, the magnitude of the scattering length, and the effective interaction between the two particles. It is this ability to tune the interaction that makes the trapped fermi gas system a versatile tool to study systems of different interaction strengths. With Feshbach resonace one can study the system from a weakly attractive BCS gas to strongly interacting unitary gases, and then to a weakly repulsive molecular BEC gases. This transition is called the "BCS-BEC crossover".

In below we use a simple one-bound state with continuum model to illustrate Feshbach resonance, and we follow the treatment in [40].

A.2 one-bound state with continuum model

Consider a two particle system with Hamiltonian $H = H_0 + V$. H_0 is the bare Hamiltonian that has free two particle states when they are far apart, and it has a bound state when the particles are close together. V is the coupling potential. One has the continuous states $|k\rangle$ and one bound state $|m\rangle$ that satisfy:

$$\begin{aligned} H_0|k\rangle &= 2\epsilon_k|k\rangle \\ \epsilon_k &= \frac{k^2}{2} \\ H_0|m\rangle &= \delta|m\rangle \\ \langle m|k\rangle &= 0 \\ \langle k|k'\rangle &= c\delta_{k,k'} \end{aligned} \tag{A.2}$$

where we set $\hbar$ and m to one and c is a normalized coefficient. We now consider the true

eigen-states $|\phi\rangle$ of the system's Hamiltonian H. Let the overlap matrix element $\langle m|V|k\rangle = g_k/\sqrt{\Omega}$. Representing $|\phi\rangle$ with the bare states, we get:

$$\begin{aligned} H|\phi\rangle &= E|\phi\rangle \\ |\phi\rangle &= \alpha|m\rangle + \sum_k c_k|k\rangle \end{aligned} \tag{A.3}$$

Applying the bras to the LHS of Eqn.(A.3), one gets the equation of the bare scattering state coefficients c_k as:

$$Ec_k = 2\epsilon_k c_k + \sum_q \frac{g_k}{\Omega}\frac{1}{E-\delta+i\eta}\frac{g_q}{\Omega}c_q \equiv \sum_q \left(2\epsilon_q\delta_{kq} + V_{eff}(k,q)\right)c_q \tag{A.4}$$

where $i\eta$ indicates that the scattering state is an incoming state. This equation can be regarded as the eigen-equation for the scattering state, with the effect of the bound state hidden in the "effective potential" $V_{eff}(k,q) \equiv \sum_q \frac{g_k}{\Omega}\frac{1}{E-\delta+i\eta}\frac{g_q}{\Omega}$. Substitute this potential into equation for the scattering amplitude [63]:

$$f(k',k) = -\frac{V_{eff}(k'-k)}{4\pi} + \int \frac{d^3q}{(2\pi)^3}\frac{V_{eff}(k'-q)f(q,k)}{k^2-q^2+i\eta} \tag{A.5}$$

To get the scattering length we look at the low energy expression of Eqn.(A.5). This means that $k' \approx 0$, $f(k',k) = f(k)$, so that $V_{eff}(k'-k) = V_{eff}(k)$, $V_{eff}(k'-q)f(q,k) = V_{eff}(-q)f(k)V_{eff}(q)f(k) =$. Also assuming the size of the bound state is R, the value g_k then should be roughly constant up to $k_R = 1/R$, and then it quickly goes to zero. This is because higher k values generate oscillations in the overlap and thus average into zero. Thus we can approximate g_k as constant g_0 up to $k = k_R$ and zero elsewhere. With this approximation and notice that $\int \frac{d^3q}{(2\pi)^3} = \Omega$, $V_{eff}(q)$ becomes uniform (up to k_R):

$$V_{eff}(q) \equiv V_0 = \frac{g_0^2}{(E-\delta)\Omega} \tag{A.6}$$

After some rearrangement Eqn.(A.5) becomes:

$$\frac{1}{f(k)} = -\frac{4\pi}{V_0} + 4\pi \int \frac{d^3q}{(2\pi)^3} \frac{1}{k^2 - q^2 + i\eta} \tag{A.7}$$

The integral term in Eqn.(A.7) deserves special attention: it is a diverging quantity, so one must introduce a cutoff, which to be consistent we choose to be k_R. Using the fact that

$$\frac{1}{g(r) + i\eta} = \frac{P}{g(r)} - i\pi\delta(g(r)) \tag{A.8}$$

where "P" stands for principle value. One has:

$$\begin{aligned}
4\pi \int \frac{d^3q}{(2\pi)^3} \frac{1}{k^2 - q^2 + i\eta} &= \frac{2}{\pi} \int_0^{k_R} \frac{q^2 dq}{k^2 - q^2 + i\eta} \\
&= \frac{2}{\pi} P \int_0^{k_R} \frac{q^2 dq}{k^2 - q^2} - ik \\
&= \frac{2k}{\pi} \left[\int_0^{\pi/2} \frac{\sin^2\theta}{\cos\theta} d\theta - \int_0^{\theta_R} \sec^2\theta \csc\theta \right] - ik \\
&= \frac{2k}{\pi} \left[-\frac{1}{kR} + k \int_{\theta_R}^{\pi/2} \csc\theta d\theta \right] - ik \approx \frac{2k}{\pi} \left[-\frac{1}{kR} + k^2 \right] - ik \\
&= -\frac{2}{\pi R} + \frac{2R}{\pi} k^2 - ik
\end{aligned} \tag{A.9}$$

where the term $\frac{2R}{\pi}k^2$ corresponds to the effective range term of the bare interaction, which we neglect due to the smallness of R. Let $g_0^2/4\pi \equiv \sqrt{2E_0}$ measure the strength of the coupling, and $E \equiv k^2 + \delta_0$, where δ_0 indicates the energy shift from the coupling to the bound state The inverse low energy scattering amplitude Eqn.(A.7) becomes:

$$\frac{1}{f_0(k)} \approx -\frac{1}{\sqrt{2E_0}}(\delta_0 - \delta) - \frac{1}{\sqrt{2E_0}} k^2 - ik \tag{A.10}$$

with $1/f_0(k) = kcot\delta - ik \approx -\frac{1}{a} + \frac{1}{2} r_{eff} k^2$ [63],we get the scattering length and effective range be

$$\begin{aligned}
a &= \sqrt{2E_0} \frac{1}{\delta_0 - \delta} \\
r_{eff} &= -\sqrt{\frac{2}{E_0}}
\end{aligned} \tag{A.11}$$

To see one can indeed change the sign of $\delta_0 - \delta$, and thus the scattering length a from positive to negative, one starts from Eqn.(A.3), apply bras to the LHS of A.3, and eliminate eigenfunction coefficients:

$$E - \delta \equiv k^2 + \delta_0 - \delta = \frac{1}{\Omega} \sum_q \frac{g_q^2}{k^2 + \delta_0 - q^2}$$
$$\delta \approx \delta_0 + \frac{g_0^2}{\Omega} \sum_q \frac{1}{\delta_0 - q^2} \tag{A.12}$$

We see that the terms with $q < \delta_0$ contribute positive to the summation, while $q < \delta_0$ contribute negative. Thus there is be a value δ_0 that makes the total summation be zero, so that $\delta = \delta_0$ and scattering length diverges. Below this value we get a positive scattering length, while above we get a negative scattering length. In experiment both the energy of the scattering triplet state and singlet state are shifted linearly by the external magnetic field. Therefore we expect the shift $\delta_0 - \delta$ has a term $\Delta\mu(B - B_0)$, where $\Delta\mu$ is the magnetic moment difference and B_0 is the resonance magnetic field. Combine with that the bare scattering particles itself has an intrinsic scattering length a_{bg} when no external field is applied, one can write the final expression of the scattering length be:

$$a = a_{bg}(1 - \frac{\Delta B}{B - B_0}) \tag{A.13}$$

Fig.(A.1) shows the actual energy spectrum of the Hamiltonian $H = H_0 + V$. The dotted line is the uncoupled bound state. The red line is the true bound state that merges with the continuous scattering state at zero detuning. The blue line is the scattering length.

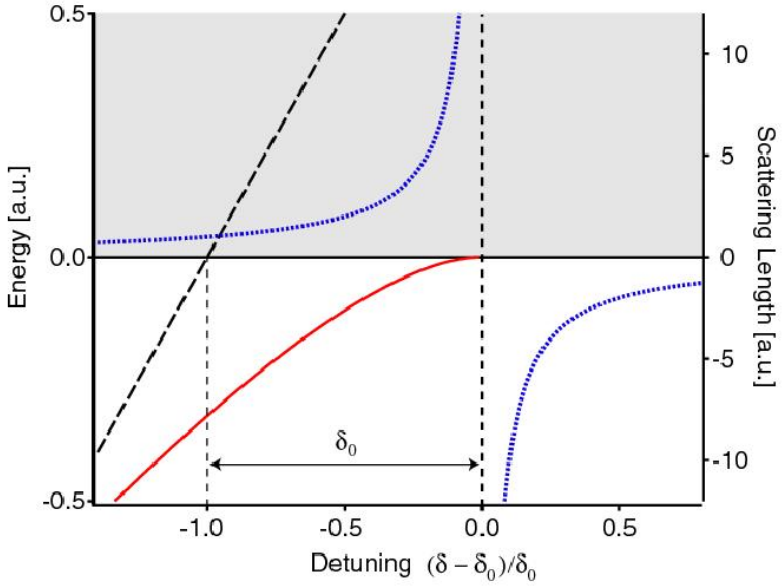

Figure A.1: The actual energy spectrum of the Hamiltonian and the scattering length [40]. The dotted line is the uncoupled bound state. The red line is the true bound state that merges with the continuous scattering state at zero detuning. The blue line is the scattering length.

Appendix B

FORMATION OF THE SYMMETRIC LOCAL DENSITY APPROXIMATION (SLDA) EQUATION

In this chapter we derive the Bdg-like equation Eqn.(1.56) from the non-normalized functional Eqn.(1.51). We first derive the expression for the normalized coefficient g_{eff} for the pairing potential, and then we perform variations on the functional to give the Bdg-like equation used in this dissertation.

B.1 Renomalization procedure on the energy functional

The local density approximation for the superfluid system with constant coefficient is equivalent to use a constant contact interaction to describe the system. Such constant contact interaction, however, is only valid in the low energy description and leads to divergence in the anomalous density [27]. Assuming that the system's behavior is dominated by the low energy description, one can simply "renormalize" the theory by throwing out the divergence. The simplest way to do so is to introduce an energy cutoff E_c, as in the BCS theory [8] that uses the Debye frequency as the cutoff energy. However, in the trapped fermi system there is no such physical energy to serve as the cutoff energy. Therefore simply using an arbitrary cutoff energy for calculating the physical quantities lacks the consistent treatment to the theory. On can also relax the contact interaction potential and use a finite range potential [20], but this makes the theory much more complicate to calculate.

Here we find a consistent way to directly subtract out the divergence in the anomalous density. We first identify the form of the divergent part and then subtract that part with another form *including an energy cutoff* E_c such that when taking E_c to infinity, this form identically cancels out the divergence in the anormalous density. By first assuming that the anormalous density $\nu = \nu(R, r)$ is non-local, Bruun et al. in [10] find that the divergent part is proportional to pairing field and $1/r$:

$$\nu(R,r)_{r\to 0} = \frac{1}{4\pi r}\delta(R) + F_{reg}(R) + O(r) \tag{B.1}$$

Therefore, we need a term that is easy to calculate and has the same $\frac{1}{4\pi r}\delta(R)$ term to subtract the divergence. In [10] the authors find out that the real-space Green's function exactly has this $1/r$ term. However the Green's function they choose is system-dependent, and thus need to solve the eigen-equation to get the function. This is unnecessarily complicate, and Bulgac and Yu [17] instead use simply the free-particle Green's function with Thomas-Fermi approximation:

$$\begin{aligned} G_0\left(r_1, r_2, k_F(r) \equiv \sqrt{2(\mu - U(r))}\right) &\equiv -\frac{\exp\left(ik_F(r)|r_1 - r_2|\right)}{2\pi|r_1 - r_2|} \\ &= -\frac{1}{2\pi|r_1 - r_2|} - \frac{ik_F(r)}{2\pi} + O(|r_1 - r_2|) \end{aligned} \tag{B.2}$$

One gets the regularized anomalous density by adding
$\frac{\Delta(r)}{2}G_0(|r_1 - r_2| \to 0, k_F(r)) + \frac{ik_F(r)}{2\pi}$ to the unregularized anormalous density:

$$\begin{aligned} \nu_{reg}(r) &= \nu_c(r) + \frac{ik_F(r)}{4\pi} + \frac{\Delta(r)}{4\pi}\frac{\exp\left(ik_F(r)r'\right)}{r'}_{r'\to 0} \\ &= \nu_c(r) + \frac{ik_F(r)}{4\pi} + \frac{\Delta(r)}{2}H_0^{-1}(r' \to 0) \\ &= \nu_c(r) + \frac{ik_F(r)}{4\pi} + \frac{\Delta(r)}{2}\frac{1}{2\pi^2}\int_0^{k_c(r)} \frac{e^{(ikr')}k^2 dk}{\epsilon_F(r) - k^2/2 + i\gamma} \\ &= \nu_c(r) + \frac{ik_F(r)}{4\pi} + \frac{\Delta(r)}{4\pi^2}\int_0^{k_c(r)} \frac{k^2 dk}{\epsilon_F(r) - k^2/2 + i\gamma} \\ &= \nu_c(r) - \frac{\Delta(r)k_c(r)}{2\pi^2}\left[1 - \frac{k_F(r)}{2k_c(r)} ln\frac{k_c(r) + k_F(r)}{k_c(r) - k_F(r)}\right] \end{aligned} \tag{B.3}$$

where

$$\begin{aligned} \nu_c(r) &= \sum_{E_i \le E_c} v_i^*(r)u_i(r) \\ \epsilon_F(r) &= k_F(r)^2/2 = \mu - U(r) \\ E_c &= k_c(r)^2/2 + U(r) - \mu \end{aligned} \tag{B.4}$$

The integral evaluation in Eqn.(B.3) is identical to the scattering amplitude in Appendix A. The cutoff energy E_c is introduced here because we cannot sum up to infinite states in numerical calculations. When pushing E_c to infinity the divergent terms cancel identically. With this expression of the regularized anomalous density and $\Delta(r) = -g\nu_{reg}(r)$, by moving the terms in Eqn.(B.3) proportional to Δ to the left hand side, we get the expression of the pairing field $\Delta(r)$ in terms of unnormalized anomalous density $\nu_c(r)$:

$$\begin{aligned} \Delta(r) &= -g\nu_{reg}(r) = -g_{eff}\nu_c(r) \\ g_{eff}^{-1}(r) &= g^{-1} - \frac{k_c(r)}{2\pi^2}\left[1 - \frac{k_F(r)}{2k_c(r)} ln \frac{k_c(r)+k_F(r)}{k_c(r)-k_F(r)}\right] \end{aligned} \tag{B.5}$$

This completes the derivation of the effective functional form in Eqn.(1.55).

B.2 Variation to the SLDA functional

We now derive the Bdg-like equation Eqn.(1.56) from the energy functional Eqn.(1.55). In terms of the quasi-particle wave-functions u_k and v_k, the various densities are represented in Eqn.(1.54). Furthermore, the u_k and v_k are not mutually independent, but they are subject to constraints from the unitary requirement in the Bogoliubov transformation. Here we reprint the constraint in Eqn.(1.26):

$$\begin{aligned} U^\dagger U + V^\dagger V &= 1 \\ U^T V + V^T U &= 0 \\ U U^\dagger + V^* V^T &= 1 \\ U V^\dagger + V^* U^T &= 0 \end{aligned} \tag{B.6}$$

The first two constraints in B.6 are automatically satisfied by the Bdg-like equation Eqn.(1.56). The first constraint is just the eigen-function normalization condition. The second constraint is satisfied by that we have a system with equal spin-up and spin-down atoms and spin-independent potentials. Thus the Bdg-like equation has a solution with energy ϵ_k, it will have another solution with $u'_k = u^*_k$, $v'_k = v^*_k$ exchanged, and energy

$\epsilon'_k = -\epsilon_k$ [60]. As a result, to derive the Bdg-like equation we will use the last two constraint in Eqn.(B.6) alone.

For convenience we reprint the energy functional Eqn.(1.55) here and ignore the underline 'c' symbol and vector symbol in $\vec{r}$"

$$\begin{aligned} E_{UFG} &= \int d\vec{r}\left[\alpha\frac{\tau(r)}{2} + \beta\frac{3(3\pi^2)^{2/3}n^{5/3}(r)}{10} + g_{eff}|\nu(r)|^2 + V_{ext}(r)n(r) + \mu n(r)\right] \\ \Delta(r) &= -g_e f f \nu(r) \end{aligned} \tag{B.7}$$

We then vary Eqn.(B.7) with respect to $u_k^*(r)$. One gets

$$\frac{\partial E_{UFG}}{\partial u_k^*(r)} = \frac{\partial E_{UFG}}{\partial n(r)}\frac{\partial n(r)}{\partial u_k^*(r)} + \frac{\partial E_{UFG}}{\partial \nu(r)}\frac{\partial \nu(r)}{\partial u_k^*(r)} + \frac{\partial E_{UFG}}{\partial \nu^*(r)}\frac{\partial \nu^*(r)}{\partial u_k^*(r)} \tag{B.8}$$

Notice that the variation with respect to τ is included in $\frac{\partial E_{UFG}}{\partial n(r)}$ as a standard practice in DFT. Similarly, doing the variations with respect to $v_k^*(r)$, we get

$$\frac{\partial E_{UFG}}{\partial v_k^*(r)} = \frac{\partial E_{UFG}}{\partial n(r)}\frac{\partial n(r)}{\partial v_k^*(r)} + \frac{\partial E_{UFG}}{\partial \nu(r)}\frac{\partial \nu(r)}{\partial v_k^*(r)} + \frac{\partial E_{UFG}}{\partial \nu^*(r)}\frac{\partial \nu^*(r)}{\partial v_k^*(r)} \tag{B.9}$$

We can easily work out the variation with respect to the densities:

$$\begin{aligned} \frac{\partial E_{UFG}}{\partial n(r)} &= -\alpha\frac{\nabla^2}{2} + \frac{\beta(3\pi^2 n(r))^{2/3}}{2} - g_{eff}^2(r)\frac{1}{3n^{2/3}(r)}|\nu(r)|^2 + \mu + V_{ext}(r) \\ &= -\alpha\frac{\nabla^2}{2} + \frac{\beta(3\pi^2 n(r))^{2/3}}{2} - \frac{|\Delta(r)|^2}{3\gamma n^{2/3}(r)} + \mu + V_{ext}(r) \equiv h(r) \\ \frac{\partial E_{UFG}}{\partial \nu(r)} &= g_{eff}(r)\nu^*(r) \\ \frac{\partial E_{UFG}}{\partial \nu^*(r)} &= g_{eff}(r)\nu(r) \end{aligned} \tag{B.10}$$

Now comes the constraints in Eqn.(B.6). Compare the fourth constraint with the expression of $\nu(r)$ we immediately get

$$\nu(r) = -\nu^*(r) \tag{B.11}$$

$$\frac{\partial \nu(r)}{\partial u_k^*(r)} = -\frac{\partial \nu^*(r)}{\partial u_k^*(r)} = -v_k(r) \tag{B.12}$$

$$\begin{aligned} \frac{\partial E_{UFG}}{\partial \nu(r)}\frac{\partial \nu(r)}{\partial u_k^*(r)} + \frac{\partial E_{UFG}}{\partial \nu^*(r)}\frac{\partial \nu^*(r)}{\partial u_k^*(r)} &= -g_{eff}(r)\nu^*(r)v_k(r) + g_{eff}(r)\nu(r)v_k(r) \\ &= 2g_{eff}(r)\nu(r)v_k(r) = -2\Delta(r)v_k(r) \end{aligned} \tag{B.13}$$

Also, from the third constraint, we get:

$$\begin{aligned} \delta\left[\frac{1}{2}n(r)+\sum_k u_k^* u_k(r)\right] &= \delta 1 = 0 \\ \frac{\partial n(r)}{\partial u_k^*(r)} &= -2u_k(r) \end{aligned} \tag{B.14}$$

Combine Eqn.(B.10), Eqn.(B.13), and Eqn.(B.14) we get:

$$\begin{aligned} -2h(r)u_k(r) - 2\Delta v_k(r) &= 2\epsilon_k' u_k(r) \\ h(r)u_k(r) + \Delta v_k(r) &= \epsilon_k u_k(r) \end{aligned} \tag{B.15}$$

In a similar fashion we get from $\frac{\partial E_{UFG}}{\partial v_k^*(r)}$:

$$\begin{aligned} 2h(r)v_k(r) - 2\Delta^* u_k(r) &= 2\epsilon_k' v_k(r) \\ \Delta^* u_k(r) - h(r)v_k(r) &= \epsilon_k v_k(r) \end{aligned} \tag{B.16}$$

Combine B.15 and B.16 give the Bdg-like equation as in Eqn.(1.56).

Appendix C

SIMULATION ENVIRONMENT, SLDA CODE STRUCTURES, AND PERFORMANCE

C.1 Running hardware

The $2D+1$ simulations are done on Hyak, a cluster own by the University of Washington [78]. We use about 1120 cores to run our programs. We also run a few big simulations on NERSC's Franklin (now retired) and Hopper [85] supercomputers at Lawrence Livermore National Lab with about 10000 cores. The $3D+1$ simulations are performed on NCSS's JaguarPF (now Titan) [82] supercomputer at Oak Ridge National Lab, using as much as 114000 cores.

C.2 Running environment, language and libraries

All the codes are written and run in Linux operating systems. The languages we use are C and Fortran90. For distributed computing we use the Message Passing Interface (MPI) library, with MPICH on Hyak, and CRAY's MPI library on JaguarPf . For solving linear algebra routine we use BLAS, Scalapack and Lapack, with version provided by Intel's Math Kernel Library (MKL) on Hyak and CRAY's Scientific Library on JaguarPF. For doing fast fourier transform we use the FFTW3 library [84]. On JaguarPF, to fully take the advantage of the parallel IO architecture, we use the LUSTRE library [83] for data input/output on JaguarPF. For $3D$ simulation data visualization we use the SILO [80] format and import them into VisIt visualization program [81] from Lawrence Livermore National Lab. For $2D+1$ simulations and other data analysis we use Matlab.

C.3 Numerical methods used in simulations

The SLDA codes consist of two parts, one is the ground state solver, the other is the time-evolving code. The flow charts of the two are shown in Fig.(2.5) and Fig.(2.5).

For the solver, the explicit BdG-like matrix Eqn.(1.56) is constructed by using the Discrete Variable Representation (DVR) with sinc function basis [47] in even-number grids. From the basis function we derive the expression of the Laplacian for the Kinetic energy term in the Hamiltonian:

$$F(x) = \frac{1}{N}\sum_{l=-N/2}^{N/2-1} \exp\left(\frac{i2\pi xl}{N}\right) = \frac{1}{N}\frac{\sin(\pi x)\exp(-i\pi x/N)}{\sin(\pi x/N)} \tag{C.1}$$

$$\nabla_{nm} = F''(x_n - x_m) = \frac{\pi^2}{2N^2}\frac{1-\delta_{nm}}{\sin^2\left(\frac{\pi(n-m)}{N}\right)} - \frac{\pi^2}{3}(1+\frac{2}{N^2})\delta_{nm} \tag{C.2}$$

To use ScaLapack's function the matrix elements are constructed with cyclic-decomposition order. The matrix is then solved by Scalapack's parallel, double precision symmetric matrix divide and conquer solver (pdsyevd) [72]. The solution u_k and v_k are used to calculate the new densities. To accelerate convergence and avoid oscillation in our solution, we implement the modified Broyden's method [36]. The principle of the Broyden method is that the new set of densities, $|n^{m+1}\rangle$ out of the Broyden method can be expressed as the previous iteration of densities $|n^m\rangle$ plus a Green function G^m times the estimated residue $|F^m\rangle = |n^m\rangle - |n^m_{out}\rangle$ we get from the previous iteration. n^m_{out} are the densities computed out of the BdG-like matrix:

$$|n^{m+1}\rangle = |n^m\rangle + G^m|F^m\rangle \tag{C.3}$$

The Green's function is estimated by starting with a simple matrix (ex: the identity matrix). In subsequent iterations it is then updated by minimizing an error function defined by the weighed sum of the distance of the Green's function to the previously calculated Green's function, as well as the distances densities difference $|\Delta n\rangle$ and $|\Delta F\rangle$ in the previous few iterations:

$$Error = w_0^2|G^m - G^{m-1}| + \sum_{k=1}^{s} w_k^2||\Delta n^{m-k}\rangle - G^m|\Delta F^{m-k}\rangle|^2 \tag{C.4}$$

where the weight w_k and s are pre-determined. Differentiating Eqn.(C.4) gives us the iterative equation of the Green's function with respect to the residues. By storing these

residues for a few previous iterations and updating the Green's function in each iteration, we can then calculate Eqn.(C.3).

For the $2D+1$ and $1D+2$ dimensional systems we simulate, the wave-functions are the products of two(one) wave-functions and one(two)-dimensional plane waves $\exp(i\vec{k}\cdot\vec{x})$. This makes the Bdg-like Hamiltonian block-diagonal with respect to the wave-vectors at the uniform density directions. With this one can further separate processors into groups G_s so that each group solves the subblocks of the Bdg-like Hamiltonian, and therefore speeds up the iteration speed dramatically.

For the time-dependent code, to achieve high accuracy, good stability, and fewer evaluations when evolving the time dependent BdG-like equation, we implement the fifth order predictor-corrector-modifier Adams-Bashforth-Milne method

[31]:

$$\begin{aligned} p_{n+1} &= \frac{y_n + y_{n-1}}{2} + \frac{dt}{48}(119y'_n - 99y'_{n-1} + 69y'_{n-1} - 17y'_{n-3}) \\ m_{n+1} &= p_{n+1} - \frac{161}{170}(p_n - c_n) \\ c_{n+1} &= \frac{y_n + y_{n-1}}{2} + \frac{dt}{48}(17m'_n + 55y'_n + 3y'_{n-1} + y'_{n-2}) \\ y_{n+1} &= c_{n+1} + \frac{9}{170}(p_{n+1} - c_{n+1}) \end{aligned} \tag{C.5}$$

where the ys are the wave-functions and the y's the derivatives. To handle the Laplacian we use the Fast Fourier Transfer routine (FFTW3) to transform the wave-functions into momentum space, applying k^2 operator, and then transform back. The dynamics are introduced through a time-dependent potential $U(x,t)$.

VITA

Yuan Lung (Alan) Luo was born in ChangHwa, Taiwan, on December 20th of the year 1986. He moved to the U.S. in 2003 for his last year of high school in Georgia State, then he moved to Seattle and earned his Bachelor degree in physics at the University of Washington. He continue attended the Physics graduate program from year 2008. In 2011 he decided to become an entrepreneur and enrolled in UW's Technology Entrepreneurship Certificate Program from Foster School of Business. His personal goal is to be the man standing in the intersection of Business, Technology, Design, and Social Welfare. When he is not intensively thinking about ideas, doing research, and working on start-up projects he reads books, blogs, and cycles in the great nature.